



THE UNIVERSITY OF QUEENSLAND
AUSTRALIA

On Integrated Photonic Quantum Simulations

Devon N. Biggerstaff
B.Sc., The University of Puget Sound
M.Sc., The University of Waterloo

*A thesis submitted for the degree of Doctor of Philosophy at
The University of Queensland in 2014
School of Mathematics and Physics*

Abstract

Quantum information science has the potential to greatly enhance our capabilities for secure communication through quantum encryption and communication technologies; for measurement sensitivity through quantum metrology; and for certain computational tasks through quantum computers. In particular, simulations of complex quantum systems—using either quantum computers or other, better-controllable quantum systems—have the potential to greatly improve our understanding of the states and dynamics of processes such as the folding of proteins, dynamics in chemistry, and energy transport on molecular and cellular scales. This thesis concerns experimental quantum information science, in particular quantum simulations, conducted using classical and quantum states of light in arrays of coupled laser-written waveguides. Integrated quantum photonics, wherein optical quantum states are manipulated in waveguide arrays, will be crucial for the miniaturization and ultimate practical scalability of optical quantum simulation and computing. Such waveguide arrays are also particularly well-suited for some quantum simulations due to the similarity between the scalar, paraxial optical wave equation and Schrodinger’s equation for a bound quantum particle.

Four experiments are described in this thesis where laser-written waveguide arrays are employed for optical quantum information science. Two of these concern waveguide optical simulations inspired by exciton transport dynamics in photosynthetic structures. For the first of these, we detail the design, modeling, and testing of a waveguide array for analog simulation of the Hamiltonian governing exciton dynamics in a particular bacterial photosynthetic subunit. We ultimately find that such a demanding simulation may exceed current capabilities in the rapidly-maturing field of laser-written waveguides, but the modeling and measurement techniques developed inform our further experiments. In the other such experiment we study an important quantum transport phenomenon, environmentally-assisted quantum transport (ENAQT), which is hypothesized to partially explain high energy transport in photosynthetic light-harvesting. We show that the transport efficiency of light in a specific disordered waveguide array can be enhanced through the addition of quantum decoherence which we implement by broadening the illumination bandwidth.

Another experiment concerns the behavior of two-photon states in a continuous-time quan-

tum walk with periodic boundary conditions implemented in an elliptic waveguide array. We use results from classical-light characterization to predict the outcomes of measurements of two-photon correlations in the array. The final experiment in this thesis details the design, modeling, fabrication, and testing of laser-written unitary circuits for heralded two-photon entangling quantum gates. We study the action of such devices in the presence of fabrication imperfections, characterize our circuits using classical and quantum interference techniques, and show such circuits to be good candidates for heralded photonic gate fabrication.

Declaration by author

This thesis is composed of my original work, and contains no material previously published or written by another person except where due reference has been made in the text. I have clearly stated the contribution by others to jointly-authored works that I have included in my thesis.

I have clearly stated the contribution of others to my thesis as a whole, including statistical assistance, survey design, data analysis, significant technical procedures, professional editorial advice, and any other original research work used or reported in my thesis. The content of my thesis is the result of work I have carried out since the commencement of my research higher degree candidature and does not include a substantial part of work that has been submitted to qualify for the award of any other degree or diploma in any university or other tertiary institution. I have clearly stated which parts of my thesis, if any, have been submitted to qualify for another award.

I acknowledge that an electronic copy of my thesis must be lodged with the University Library and, subject to the General Award Rules of The University of Queensland, immediately made available for research and study in accordance with the Copyright Act 1968.

I acknowledge that copyright of all material contained in my thesis resides with the copyright holder(s) of that material. Where appropriate I have obtained copyright permission from the copyright holder to reproduce material in this thesis.

Publications during candidature

1. James. O. Owens, Matthew. A. Broome, **Devon. N. Biggerstaff**, Michael. E. Goggin, Alessandro Fedrizzi, Trond Linjordet, Martin. Ams, Graham. D. Marshall, Jason. Twamley, Michael. J. Withford, and Andrew. G. White.
Two-photon quantum walks in an elliptical direct-write waveguide array.
New Journal of Physics **13**, 075003 (2011).
2. Martin Ringbauer, **Devon N. Biggerstaff**, Matthew A. Broome, Alessandro Fedrizzi, Cyril Branciard, and Andrew G. White.
Experimental joint quantum measurements with minimum uncertainty.
Physical Review Letters **112**, 020401 (2014).
3. Thomas. Meany[†], **Devon. N. Biggerstaff**[†], Matthew. A. Broome, Alessandro. Fedrizzi, Michael. Delanty, Michael. J. Steel, Alexei. Gilchrist, Graham. D. Marshall, Andrew. G. White, and Michael. J. Withford.
Engineering integrated photonics for heralded quantum gates.
Submitted to *Light: Science and Applications* (August 2014).
4. **Devon N. Biggerstaff**, René Heilmann, Aidan A. Zecevik, Markus Gräfe, Matthew. A. Broome, Alessandro. Fedrizzi, Stefan Nolte, Andrew. G. White, and Ivan Kassal.
Enhancing quantum transport in a photonic network using controllable decoherence.
Submitted to *Nature Photonics* (November 2014).

[†]Co-equal first authors.

Publications included in this thesis

J. O. Owens, M. A. Broome, **D. N. Biggerstaff**, M. E. Goggin, A. Fedrizzi, T. Linjordet, M. Ams, G. D. Marshall, J. Twamley, M. J. Withford, and A. G. White.

Two-photon quantum walks in an elliptical direct-write waveguide array.

New Journal of Physics **13**, 075003 (2011).

Incorporated as Ch. 6.

Contributor	Statement of contribution
D. N. Biggerstaff	Primarily responsible for circuit modeling (50%). Contributed significantly to the first (25%) and final (25%) manuscript drafts.
J. O. Owens	Shared primary responsibility for experiment design (40%) and construction (40%), data acquisition (50%), and data analysis (40%). Contributed significantly to circuit modeling (25%) and preparation of the first draft of the manuscript (20%). Contributed to final manuscript draft (10%).
M. A. Broome	Shared primary responsibility for experiment design (40%) and construction (40%), data acquisition (50%), and data analysis (40%). Contributed significantly to circuit modeling (25%), preparation of the first draft of the manuscript (30%), and the final manuscript draft (25%). Coordinated publication process and authored referee replies (100%).
M. E. Goggin	Contributed significantly to the experiment construction (20%). Contributed to the final manuscript draft (10%).
A. Fedrizzi	Contributed supervision to the experiment design (20%) and construction and data analysis. Contributed significantly to the first (25%) and final (25%) manuscript drafts.
T. Lindjordet	Primarily responsible for optical circuit design and fabrication (60%).
M. Ams	Supervised and contributed to optical circuit design and fabrication (10%).
G. D. Marshall	Supervised and contributed to optical circuit design and fabrication (10%).
J. Twamley	Supervised and contributed to optical circuit design and fabrication (10%).
M. J. Withford	Supervised and contributed to optical circuit design and fabrication (10%).
A. G. White	Contributed to supervision of experiment construction, data analysis, and the first manuscript draft. Contributed to the final manuscript draft (5%).

D. N. Biggerstaff, T. Meany, M. A. Broome, A. Fedrizzi, M. Delanty, M. J. Steel, A. Gilchrist, G. D. Marshall, A. G. White, and M. J. Withford.

Engineering integrated photonics for heralded quantum gates.

Submitted to *Light: Science and Applications* (August 2014).

Incorporated as Ch. 8.

Contributor	Statement of contribution
D. N. Biggerstaff	Primarily responsible for design and construction of circuit testing apparatus (70%) and data acquisition (90%). Fully responsible for data analysis (100%). Contributed significantly to new theory and circuit modeling (40%). Primarily responsible for first (60%) and final (75%) manuscript drafts. Coordinated manuscript submission process (100%).
T. Meany	Contributed to initial concepting (10%). Primarily responsible for optical circuit design (60%) and fabrication (80%). Contributed to design and construction of circuit testing apparatus (10%). Contributed significantly to the first manuscript draft (25%).
M. A. Broome	Contributed significantly to design and construction of circuit testing apparatus (20%). Contributed to data acquisition (10%).
A. Fedrizzi	Contributed to initial concepting (10%). Contributed supervision to the experiment design and construction and data analysis. Contributed to the first (5%) and final (5%) manuscript drafts.
M. Delanty	Contributed to initial concepting (5%) and circuit design (10%).
M. J. Steel	Contributed supervision to initial circuit design (10%).
A. Gilchrist	Contributed to initial concepting (10%). Primarily responsible for new theory and circuit modeling (60%). Contributed significantly to first (20%) and final (10%) manuscript drafts.
G. D. Marshall	Contributed to initial concepting for the optical circuit (5%).
A. G. White	Contributed to initial concepting (40%), and to supervision of experiment construction, data analysis, and the first manuscript draft. Contributed significantly to the final manuscript draft (10%).
M. J. Withford	Contributed to initial concepting (20%). Supervised and contributed to optical circuit design (10%) and fabrication (20%).

Contributions by others to the thesis

Research at its best is often collaborative, and others contributed greatly to the research that went in to the thesis. In particular their contributions to the articles which form the bulk of chapters 6 and 8 are detailed above. The material in Ch. 7 forms an early draft of manuscript which has, in more compact form and with further data, since been submitted for publication in *Nature Photonics*:

Chapter. 7: Simulating environmentally assisted quantum transport in integrated optics.

Contributor	Statement of contribution
D. N. Biggerstaff	Contributed to initial concepting (15%) and experiment design (25%). Contributed to broadband photon source construction (20%). Primarily responsible for design and construction of circuit testing apparatus (75%) and data acquisition (70%). Largely responsible for data analysis (90%). Significantly responsible for circuit modeling (40%). Responsible for writing the preliminary manuscript draft (90%) and the chapter (100%).
R. Heilmann	Primarily responsible for optical circuit design and fabrication (90%), and characterization of waveguide parameters (100%). Contributed to design and construction of circuit testing apparatus (25%). Contributed to circuit modeling (20%).
I. Kassal	Primarily responsible for initial concepting (60%) and experiment design (50%). Contributed significantly to circuit modeling (40%). Contributed significant supervision to the writing of the preliminary manuscript draft (10%) on which the chapter is partially based.
A. A. Zecevik	Primarily responsible for the construction of the broadband photon source (80%). Contributed significantly to data acquisition (30%) and analysis (10%).
A. Fedrizzi	Contributed to initial concepting (15%) and experiment design (25%). Contributed supervision to the experiment design and construction and data analysis, and contributed supervision to the writing of the preliminary manuscript draft on which the chapter is partially based.
A. Szameit	Contributed to initial concepting (5%). Contributed supervision to the design and fabrication of the optical circuit (10%).
A. G. White	Contributed to initial concepting (5%). Contributed supervision to experiment design and data analysis.

Furthermore Ivan Kassal, Thomas Meany, Alessandro Fedrizzi, Martin Ams, Michael Withford, and Andrew White contributed significantly to the research concerning simulating a biological Hamiltonian which constitutes a significant portion of chapter 5. In particular, the initial theory for that experiment was a product of Dr. Kassal's doctoral studies, and my further theoretical investigations were made in consultation and collaboration with him. M. Ams helped me fabricate waveguides for an initial parameter study, and T. Meany provided further parameter data and fabricated the waveguide sample which I tested in order to obtain the experimental results presented in that chapter. The others contributed to planning the device fabrication and the experimental investigations.

Figures 2.2, 5.3, and 5.4(b) and (c) were created by others and were reproduced with their permission for which I am thankful; in each case this has been noted in the figure caption or reference.

Finally, figures 5.1, 5.2, and 5.4(a) are reproductions from published sources and are noted as such in the captions.

Otherwise all the work presented is exclusively my own.

Statement of parts of the thesis submitted to qualify for the award of another degree

Section 2.1 is partially based on a similar introductory section of my M.Sc. thesis, and in particular Figures 2.1 and 2.3 are reproduced from that thesis, which was submitted at the University of Waterloo in Ontario, Canada in October 2009. The M.Sc. degree was awarded on 16 June 2010.

Acknowledgements

Many people deserve many heartfelt thanks for contributing to the success of my doctoral studies and my growth as a scientist. I will attempt to enumerate the major contributors here without leaving anyone out.

First, thank you to my supervisor Andrew White: for your guidance, enthusiasm, and encouragement when science stubbornly refused to work as planned. Also thanks to the other members of my advisory team: Alessandro Fedrizzi who advised me on countless aspects of experiment design and analysis as well as navigating collaborations and priorities, and Ivan Kassal who put up with my many questions and patiently helped me think through thorny theoretical questions and analysis.

The members of my research group, including other graduate students and postdoctoral researchers, greatly enhanced both my scientific learning and my enjoyment of graduate studies. So thank you to Till Weinhold and Marcelo Pereira de Almeida for your supervision and friendship; to Geoff Gillett for help with labview and matlab; to Matt Broome and Devin Smith for talking with me about physics when I needed to bounce ideas off of someone and about anything other than physics when that's what I needed; and to James Owens, Markus Rambach, Juan Loredo, Martin Ringbauer, Yarema Reshitnyk, Aidan Zecevik, Christina Giarmatzi, and Michael Stefsky for your camaraderie.

Many collaborators on the research presented in this thesis are already listed in the corresponding chapters, but special thanks go to Rene Heilmann and Tom Meany for fun and productive collaborative research visits to UQ. Thanks to Tom again as well as Mick Withford, Martin Ams, and Graham Marshall for hosting me on multiple productive visits to their lab at Macquarie University. I am also grateful to Alexei Gilchrist for all your work not only on theory for our collaborative efforts but also on helping me to understand it.

Without all my previous supervisors and mentors in physics I never would have made it in to a physics PhD program, let alone finished. Heartfelt thanks to Alan Thorndike at the University of Puget Sound who supervised me and collaborated on my first research project, to Kevin Resch and Rainer Kaltenbaek for supervising my Masters at the Institute for Quantum Computing at the University of Waterloo, and to Mike Raymer at the University of Oregon for the research experience I gained in his lab, and for suggesting I visit Andrew's lab in sunny Queensland in the first place.

Thanks to all the friends and family back in North America who kept in touch and helped me keep everything in perspective, and especially to those who visited me in Australia as well as to those who attended my wedding in the middle of my doctoral studies and helped make it a blast. Josh and Evan, I miss you guys and thanks for all the vacations and being Best Men!

Many thanks to my parents Dennis and Rae Lynn and my brother Tyson for all their love and support throughout my life. I miss you, please come visit soon!

Finally, the biggest thanks go to my lovely wife Katrina for supporting me in every sense throughout this process. I love you.

Keywords

photonics, integrated optics, quantum optics, quantum information, single photons, simulation.

Australian and New Zealand

Standard Research Classifications (ANZSRC)

ANZSRC code: 020604 Quantum Optics (20%)

ANZSRC code: 020504 Photonics, Optoelectronics and Optical Communications (20%)

ANZSRC code: 020603 Quantum Information, Computation and Communication (60%)

Fields of Research (FoR) Classification

FoR code: 0205 Optical Physics (40%)

FoR code: 0206 Quantum Physics (60%)

Contents

Abstract	i
Declaration by author	iii
Publications included in this thesis	v
Acknowledgements	ix
List of tables	xvi
List of figures	xviii
List of abbreviations and glossary of terms	xix
1 Preface	1
1.1 Overview of the thesis	2
1.1.1 A brief explanation of some features of this thesis	4
References	5
2 An overview of quantum information and computation	7
2.1 Quantum information	8
2.1.1 Quantum states	8
2.1.1.1 Mixed states and decoherence	8
2.1.1.2 Qubits	9
2.1.2 State evolution	12
2.1.3 Quantum measurement	13
2.1.3.1 Projective measurements	13
2.1.3.2 Fidelity of states	15
2.1.3.3 Generalized measurements and POVMs	16
2.1.4 Quantum correlations and entanglement	17
2.1.4.1 The partial trace	18
2.1.5 General quantum processes	19

2.1.5.1	Open quantum systems and master equations	22
2.1.6	Quantum tomography	23
2.1.7	Teleportation	25
2.2	Quantum computing	26
2.2.1	The quantum network model	26
2.3	Conclusion	28
	References	29
3	Quantum information experiments with photons	31
3.1	The quantized optical field	31
3.2	Encoding photonic qubits	33
3.2.1	Manipulating photons: Beamsplitters and phase-shifters	35
3.2.2	Manipulating polarization-encoded photons: birefringence	36
3.2.3	Waveplates	37
3.3	Creating Photons through Spontaneous Parametric Downconversion	39
3.3.1	(Quasi-)Phase Matching Conditions	39
3.4	Conclusion	40
	References	41
4	Quantum simulation and quantum walks	43
4.1	Introduction to quantum simulation	43
4.1.1	Quantum simulation procedure	44
4.1.2	Digital versus analog quantum simulation	45
4.1.3	Previous work	47
4.2	Quantum walks: a resource for quantum simulations	48
4.2.1	Discrete-time quantum walks	49
4.2.2	Continuous-time quantum walks	50
4.2.3	Applications of quantum walks	51
4.2.4	CTQWs: Models for coherent transport phenomena	52
	References	54

5	Coupled waveguide arrays, and their use in simulating quantum walks and biological Hamiltonians	58
5.1	Introduction	58
5.2	Laser-written waveguide arrays	59
5.2.1	Material modification mechanisms	60
5.2.2	Waveguide modes, coupling, phase shifts, and circuits	62
5.2.3	Practical fabrication considerations: waveguide profile and polarization dependence	65
5.3	Quantum simulation in coupled waveguide arrays	68
5.3.1	Simulating the LH-II B850 subunit in <i>Rhodobacter sphaeroides</i> : initial theory	69
5.3.2	Practical considerations: realistic coupling curves and determining dynamics	74
5.3.3	Modeling waveguide arrays	76
5.3.4	Preliminary results and accounting for strong coupling	78
5.3.5	Prototype measurement and results	82
5.3.6	Conclusions and prospects for further investigations	83
	References	87
6	Two-photon quantum walks in an elliptical direct-write waveguide array	91
6.1	Introduction	92
6.2	Device Description	93
6.3	Optical chip characterisation	94
6.4	Two-photon walks	97
6.5	Discussion	100
6.6	Appendix	102
	References	106
7	Simulating environmentally assisted quantum transport in integrated optics	109
7.1	Introduction	109
7.2	General theory of ENAQT	111
7.3	Waveguide implementation	114
7.3.1	Fabrication of ENAQT simulation circuits	117
7.4	First-generation ENAQT experiment	119
7.4.1	First-generation results	121
7.5	Second-generation ENAQT circuits and results	124

7.5.1	Modeling the effects of fabrication parameter variance	125
7.5.2	Monochromatic characterization results	126
7.6	Conclusions and future work	129
	References	131
8	Engineering integrated photonics for heralded quantum gates	133
8.1	Introduction	134
8.2	Materials and Methods	135
8.2.1	Circuit modelling and design.	135
8.2.2	Device fabrication	137
8.3	Results and Discussion	139
8.3.1	Coherent device characterisation.	139
8.3.2	Verification using two-photon interference.	141
8.4	Conclusions	144
	References	145
9	Conclusion and outlook	148
	References	151

List of tables

5.1	Hamiltonian of the B850 subunit of light-harvesting system II in <i>Rhodobacter sphaeroides</i>	72
6.1	The measured array of Mueller matrices.	105

List of figures

2.1	The Bloch Sphere	10
2.2	An illustration of quantum state tomography	24
2.3	Teleporation circuit	26
5.1	Illustration of the femtosecond laser direct waveguide-writing process.	60
5.2	A schematic of a directional coupler.	65
5.3	Before and after microscope images of waveguide annealing.	68
5.4	Simulating the B850 subunit of LH-II in <i>Rhodobacter sphaeroides</i>	71
5.5	Dynamics of the B850 Hamiltonian, and dynamics of computer models of waveguide arrays designed to simulate that Hamiltonian	80
5.6	Characterization measurements for a prototype B850 Hamiltonian simulation waveguide array circuit.	84
5.7	Relative output distribution for all 16 inputs for a prototype B850 Hamiltonian simulation waveguide circuit.	85
6.1	Schematic of the integrated waveguide circuit and associated output.	93
6.2	Experimental setup for characterizing the optical chip.	95
6.3	Comparison of numerical simulations and observed probability distributions for the optical chip.	96
6.4	Poincaré sphere representation of the measured Mueller matrices.	97
6.5	Example of two-photon interference.	99
6.6	Correlation matrices for nearest-neighbour input channels 1 and 2.	99
6.7	Correlation matrices for next-nearest neighbour input channels 2 and 4.	100
7.1	Describing and simulating environmentally-assisted quantum transport.	113
7.2	Simulated and measured propagation in the ENAQT circuit.	118
7.3	Measurement setup and photon spectra.	120

7.4	Annotated photographs of the experimental setup for measuring the ENAQT simulation chip.	122
7.5	Results from the first-generation ENAQT simulation.	123
7.6	Preliminary second-generation ENAQT simulation results.	125
7.7	Modeling effects of fabrication parameter variations on Hamiltonian condition for ENAQT.	127
7.8	Measured narrow-bandwidth bath occupancy vs. wavelength for the second-generation ENAQT simulator	129
8.1	Circuit for the Knill heralded CZ gate.	136
8.2	Variation of fidelity metrics with phase and reflectivity deviations.	138
8.3	Results from coherent circuit characterization.	140
8.4	Quantum interference measurement setup and results.	143

List of Abbreviations and Glossary of Terms

Glossary

Rhodobacter sphaeroides A purple photosynthetic bacteria which lives in dark conditions and has evolved light-harvesting efficiency of nearly 100%. The light harvesting complexes in this bacteria have been studied extensively. [3](#), [59](#), [69](#), [71](#), [149](#)

hcz Heralded controlled- Z linear-optic quantum logic gate, specifically referring to the efficient design found by E. Knill. [135–137](#), [141–144](#)

BosonSampling A protocol consisting of sampling the output distribution of many interacting bosons in a linear-optical network. Conjectured to be computationally hard to simulate on a classical computer but easy to implement in practice, at least relative to other large-scale quantum computations and simulations. [48](#), [49](#)

decoherence Generally irreversible loss or reduction of the coherence terms in the density matrix for a quantum state describing a system which occurs through interaction of the system with its environment. Usually decreases the purity of the quantum state for the system, *i. e.* results in a mixed state. [9](#)

efficient (In computational complexity theory:) Requiring resources (e.g. time, memory, number of logical gates) which scale at worst polynomially with the size of the problem. Problems for which resource requirements scale exponentially are computationally inefficient. [7](#), [45](#)

Fock states States consisting of well-defined integer numbers of photons in an optical field mode which form an orthonormal basis for that mode.. [33](#)

QC_N Network model for quantum computation, also often called the circuit model. [27](#)

qubit A quantum bit; a two-level quantum system; a quantum system with a Hilbert space of dimension two. [9](#), [27](#), [28](#), [44–47](#), [51](#)

Acronyms

- APD** avalanche photodiode single photon detector. 123
- AQS** analog quantum simulator. 47
- BBO** β -barium-borate. 144
- BS** beamsplitter. 135–139, 141, 142, 144
- BSM** Bell-state measurement. 25, 26
- CAD** computer-aided design. 77
- CCD** charge-coupled device. 82, 83
- CMT** coupled-mode theory. 76–80, 82
- CTQW** continuous-time quantum walk. 23, 51–54, 58, 67, 68
- CTRW** continuous-time random walk. 49, 53
- DQS** digital quantum simulator. 46
- DTQW** discrete-time quantum walk. 35, 50, 51
- DTRW** discrete-time random walk. 49, 51
- ENAQT** environmentally-assisted quantum transport. 3, 54, 110–118, 120–122, 124–128, 130, 150
- FD-BPM** finite-difference beam propagation methods. 77–80
- FLDW** femtosecond laser direct-write. 59, 64–66, 135, 138, 139, 143, 145
- FMO** Fenna-Matthews-Olson complex. 54
- FWHM** full width at half-maximum. 117, 118
- HOM** Hong-Ou-Mandel. 52
- LHC** light-harvesting complex. 53, 59, 69
- LOQC** linear optics quantum computing. 135, 143, 145
- NA** numerical aperture. 62, 67

- ppKTP** periodically-poled potassium titanyl phosphate. 120, 121
- QC** quantum computer. 7, 45, 46, 52
- QIP** quantum information processing. 7, 9, 12, 29, 35, 45, 59
- QPT** quantum process tomography. 24
- QS** quantum simulator. 7, 44, 45, 48, 59
- QST** quantum state tomography. 23, 47
- QW** quantum walk. 50, 52, 58
- RC** Reaction Center. 53, 54, 70
- RW** random walk. 49, 50
- SPDC** spontaneous parametric downconversion. 82, 120, 121, 123, 126, 131, 142–144
- UQC** universal quantum computer. 45
- UQS** universal quantum simulator. 45

Chapter 1

Preface

This thesis is about experiments with classical and quantum states of light in arrays of coupled laser-written waveguides. These experiments focus primarily on analog optical simulation of quantum phenomena, and on steps towards optical quantum computers which could be used for digital quantum simulations.

The analogy between optics and quantum mechanics dates back to even before the formalization of quantum theory: in 1928 J. Slater treated light quanta—photons—using wave mechanics developed for electrons [1], and showed that the photons’ “wave equation is the ordinary optical wave equation. Heisenberg’s principle of indeterminateness becomes a description of diffraction.” By 1974 an analogy had been established between coupled optical waveguides and the quantum mechanical double-well potential [2], and since then myriad experiments have demonstrated simulations of quantum effects using light, particularly guided optics [3].

Besides such simulations-by-analogy—or analog simulations—digital simulations of quantum phenomena are of course possible; however by 1982 it had become clear—as noted by Richard Feynman [4]—that simulating large quantum systems was exceedingly difficult on conventional digital computers. In the same reference he proposed the germ of an idea which would become the modern field of quantum computation research, with the goal of building a quantum computer, in which information can be stored in quantum superpositions and operated upon with quantum operations. Demonstrations by Shor [5] and Steane [6] that efficient error correction is in principle possible on such a machine, and by Lloyd that a universal quantum computer could also serve to digitally simulate any quantum system [7], set the stage for a different means by which light could be used for the simulation of quantum phenomena: by forming part of an optical digital quantum computer. This possibility was given a further boost by Knill, LaFlamme, and Milburn who showed in 2001 that linear optics

and quantum measurement could be combined to enable in-principle universal and efficient quantum computing employing nondeterministic—but heralded—multi-qubit quantum logic gates [8].

Integrated quantum photonics, wherein optical quantum states are manipulated—and possibly created and detected—in arrays of waveguides embedded in a monolithic chip, will be crucial to the further development of digital optical quantum simulation: without the miniaturization and intrinsic phase stability of this medium, a large-scale optical quantum computer would be a practical impossibility. The rapid pace of progress in this field has been a source of excitement throughout my graduate studies: the first integrated entangling quantum gate was demonstrated early during my Masters studies [9], closely followed by integrated proof-of-principle quantum algorithms [10], reconfigurable integrated quantum circuits, integrated photon sources, and detection [11–14]. Laser-written quantum photonic circuits, wherein waveguides are directly drawn into glass with a focused pulsed laser, have shown a particularly striking rate of maturation: quantum interference between photons was only first demonstrated in such circuits in 2009 [15]. They have since been used to demonstrate arbitrary beamsplitting and phase-shifting operations, which in turn allow implementation of arbitrary unitary operations on multiple spatial path modes [11, 16–18], and very recently arbitrary unitary operations on polarization as well [19, 20].

Arrays of evanescently coupled waveguides are also particularly well-suited for some analog optical simulations of quantum phenomena. This is ultimately due to the similarity between the scalar, paraxial optical wave equation and Schrödinger’s equation for a bound quantum particle. In particular, the behavior of light in an array of weakly-coupled waveguides is governed by the same Hamiltonian as the tight-binding model [21], which describes many quantum phenomena where the states of delocalized particles are described by superpositions of wavefunctions localized at discrete sites. This makes waveguide arrays an optimal candidate for analog simulations of quantum transport phenomena.

1.1 Overview of the thesis

The primary experimental results of this thesis are contained in Chapters 6-8, two of which are based on published or submitted manuscripts [22, 23]. Each of these chapters is largely self-contained and could be read in isolation by a reader knowledgeable in this field, although cross-referencing to material in the remainder of the thesis has been provided where appropriate. Chapters 2-4 provide background and introductory material on quantum information and computation, their implementation in optics, and quantum simulation and quantum walks,

respectively. Chapter 5 bridges these sections: it introduces laser-written waveguide arrays and their utility for quantum simulations using an experimental simulation as a working example. Chapters 2 through the first part of chapter 5 are also designed to be a useful introductory resource for beginning researchers in quantum photonics and simulations. The chapter contents are further detailed below:

Chapter 2 introduces the concepts and formalism of quantum information and quantum computation. Chapter 3 briefly introduces the encoding, manipulation, and creation of single photons for linear optics experiments in quantum information processing.

In Chapter 4, the history and theory of digital and analog quantum simulation are introduced in some detail. Quantum walks, the quantum analogues to classical random walks, are introduced in the second half of the chapter and their utility for quantum simulations is explored.

Chapter 5 describes the fabrication of laser-written waveguide arrays and their use for integrated quantum photonic circuits. In particular the second half of the chapter illustrates in detail how such arrays can be used for analog quantum simulations. This is explained via a working example: we present the theory, modeling, and experimental results for a waveguide array quantum simulator of the the Hamiltonian which governs exciton dynamics in a particular photosynthetic light harvesting subunit in the *Rhodobacter sphaeroides* purple bacteria.

In Chapter 6 we study the evolution of two-photon continuous-time quantum walks in an elliptic array of laser-written waveguides. This chapter is a reproduction of a published paper, which has only been reformatted for the thesis. We characterise the photonic chip via coherent-light tomography and use the results to predict distinct differences between temporally indistinguishable and distinguishable two-photon inputs which we then compare with experimental observations.

In Chapter 7 we detail the design and experimental implementation of a simulation, in a laser-written waveguide array, of environmentally-assisted quantum transport (ENAQT). This is a quantum transport phenomenon hypothesized to play an important role in explaining the high transport efficiency of photosynthetic light harvesting, where the efficiency of energy transport in a disordered network can be enhanced by the presence of moderate amounts of quantum noise or decoherence.

Scaling up linear-optics quantum computing will require multi-photon gates which are compact, phase-stable, exhibit excellent quantum interference, and have success heralded by the detection of ancillary photons. In Chapter 8 we investigate implementation of the optimal known gate design which meets these requirements: the Knill controlled- Z gate, implemented

in integrated laser-written waveguide arrays. This chapter is a reproduction of a paper which has recently been submitted for publication.

1.1.1 A brief explanation of some features of this thesis

The numbers listed after each item in the List of Abbreviations, Glossary of Terms, List of Acronyms, and in the Lists of References at the end of each chapter denote the pages on which that item was referenced. In the electronic version of the thesis, these numbers are hyperlinks to the page in question. Any acronyms in the text are also hyperlinks: clicking on the acronym will take you to its definition in the List of Acronyms. Finally all references to figures, tables, chapters, sections, and pages will be hyperlinks as well. Such an electronic copy of the thesis can be obtained by contacting the author.

References

- [1] Slater, J. C. Light quanta and wave mechanics. *Phys. Rev.* **31**, 895–899 (1928). [1](#)
- [2] Tsai, T. & Thomas, G. Analog between optical waveguide system and quantummechanical tunneling. *American Journal of Physics* **44**, 636–638 (1976). [1](#)
- [3] Longhi, S. Quantum-optical analogies using photonic structures. *Laser Photon. Rev.* **3**, 243–261 (2009). [1](#)
- [4] Feynman, R. Simulating physics with computers. *Int. J. Theor. Phys.* **21**, 467–488 (1982). [1](#)
- [5] Shor, P. W. Scheme for reducing decoherence in quantum computer memory. *Phys. Rev. A* **52**, R2493–R2496 (1995). [1](#)
- [6] Steane, A. M. Error correcting codes in quantum theory. *Phys. Rev. Lett.* **77**, 793–797 (1996). [1](#)
- [7] Lloyd, S. Universal quantum simulators. *Science* **273**, 1073–1078 (1996). [1](#)
- [8] Knill, E., Laflamme, R. & Milburn, G. J. A scheme for efficient quantum computation with linear optics. *Nature* **409**, 46–52 (2001). [2](#)
- [9] Politi, A., Cryan, M. J., Rarity, J. G., Yu, S. & O’Brien, J. L. Silica-on-silicon waveguide quantum circuits. *Science* **320**, 646–649 (2008). [2](#)
- [10] Politi, A., Matthews, J. C. F. & O’Brien, J. L. Shor’s quantum factoring algorithm on a photonic chip. *Science* **325**, 1221 (2009). [2](#)
- [11] Smith, B. J., Kundys, D., Thomas-Peter, N., Smith, P. G. R. & Walmsley, I. A. Phase-controlled integrated photonic quantum circuits. *Opt. Express* **17**, 13516–13525 (2009). [2](#)
- [12] Li, H. W. *et al.* Reconfigurable controlled two-qubit operation on a quantum photonic chip. *New J. Phys.* **13**, 115009 (2011). [2](#)
- [13] Shadbolt, P. J. *et al.* Generating, manipulating and measuring entanglement and mixture with a reconfigurable photonic circuit. *Nature Photon.* **6**, 45–49 (2012). [2](#)
- [14] Sprengers, J. P. *et al.* Waveguide superconducting single-photon detectors for integrated quantum photonic circuits. *Appl. Phys. Lett.* **99**, 181110 (2011). [2](#)

-
- [15] Marshall, G. D. *et al.* Laser written waveguide photonic quantum circuits. *Opt. Express* **17**, 12546–12554 (2009). 2
- [16] Crespi, A. *et al.* Integrated multimode interferometers with arbitrary designs for photonic boson sampling. *Nature Photon.* **7**, 545–549 (2013). 2
- [17] Heilmann, R., Keil, R., Grfe, M., Nolte, S. & Szameit, A. Ultraprecise phase manipulation in integrated photonic quantum circuits with generalized directional couplers. *Applied Physics Letters* **105**, – (2014). 2
- [18] Reck, M., Zeilinger, A., Bernstein, H. & Bertani, P. Experimental realization of any discrete unitary operator. *Phys. Rev. Lett.* **73**, 58–61 (1994). 2
- [19] Corrielli, G. *et al.* Rotated waveplates in integrated waveguide optics. *Nature Commun.* **5** (2014). 2
- [20] Heilmann, R., Grafe, M., Nolte, S. & Szameit, A. Arbitrary photonic wave plate operations on chip: Realizing hadamard, pauli-x, and rotation gates for polarization qubits. *Sci. Rep.* **4** (2014). 2
- [21] Kassal, I. *Quantum Computation for Chemical Problems*. Ph.D. thesis, Harvard University (2010). 2
- [22] Owens, J. O. *et al.* Two-photon quantum walks in an elliptical direct-write waveguide array. *New J. Phys.* **13**, 075003 (2011). 2
- [23] Biggerstaff, D. N. *et al.* Engineering integrated photonics for heralded quantum gates. Submitted to: *Light: Science and Applications* (2014). 2

Chapter 2

An overview of quantum information and computation

All of modern digital information processing can be reduced to algorithms running on strings of binary digits or *bits*. Each bit has only two possible states, zero or one, and yet by applying complex algorithms consisting of acting on bit strings with many simple arithmetic operations, we can use digital information processors, more commonly known as computers, to solve a vast range of problems.

Yet there are many information processing tasks which modern computers cannot perform efficiently, meaning the number of bits and/or the number of mathematical operations required grows exponentially as the size of the problem increases. Prominent examples include factoring the products of large prime numbers, searching large databases, and perhaps most importantly, simulating the dynamics of systems consisting of many particles interacting at the quantum level.

The idea behind quantum information processing (QIP) is to process information in quantum states using coherent quantum operations, and thereby to take advantage of certain properties of quantum states, particularly *superposition*, *interference*, and *entanglement*, to solve certain problems more efficiently than possible classically. Richard Feynman first suggested the idea of a quantum computer just over three decades ago [1]. Since then the theory of QIP has been formalized, and Feynman's seed of an idea has spawned multiple new areas of academic investigation, as well as considerable experimental and engineering efforts towards processing quantum information and simulating quantum systems using quantum computers (QCs) and quantum simulators (QSS) [2]. This chapter provides a summary of concepts in QIP and QC which are important throughout the rest of the thesis.

2.1 Quantum information

2.1.1 Quantum states

In quantum theory the state of an isolated physical system can be represented as a unit vector $|\psi\rangle$ in an abstract Hilbert space \mathcal{H} . A Hilbert space is complex vector space with a defined inner product and distance measure. Valid quantum states must be normalized, meaning the inner product $\langle\psi|\psi\rangle = 1$. Such states $|\psi\rangle$ are often called wavefunctions. If $\{|\psi_i\rangle\}$ are all physically valid states then any superposition $|\phi\rangle = \sum_i c_i |\psi_i\rangle$, $c_i \in \mathbb{C}$ will also be a physically valid state, as long as $\langle\phi|\phi\rangle$ is still equal to unity, or equivalently $\sum_i |c_i|^2 = 1$. This is known as the *superposition principle*.

If \mathcal{H} is of finite dimension then $|\psi\rangle$ can be represented as a d -vector in a particular orthonormal basis $\{|\chi_j\rangle\}$ with $j = \{1, \dots, d\}$ and $\langle\chi_i|\chi_k\rangle = \delta_{ik}$. The normalization condition implies the following restriction on the d elements of the vector c_i : $\sum_i |c_i|^2 = 1$. A d -dimensional system will be termed a qudit.

The state space of a composite system consisting of subsystems $\{\mathcal{H}^j\}$, $j = \{0, 1, \dots\}$, each with respective dimension d_j , is given by the tensor product $\bigotimes_j \mathcal{H}^j = \mathcal{H}^0 \otimes \mathcal{H}^1 \otimes \mathcal{H}^2 \otimes \dots$, and will have dimension $\prod_j d_j$.

2.1.1.1 Mixed states and decoherence

The preceding discussion and the notion of wavefunctions suffices to describe *pure* states, the fully-coherent superpositions of basis states which occur when the physical system described is completely isolated from interactions with its environment. However, the system in question may not be isolated, and may in fact have become correlated with its environment. In fact in experiment this is unavoidable¹. Furthermore we may wish to describe a state taken from an ensemble which is formed from a statistical mixture of pure states.

In these cases the system must be described using the *density operator* formalism: a state is represented by an $d \times d$ nonnegative operator ρ acting on \mathcal{H}_d which is Hermitian (self-adjoint; $\rho^\dagger = \rho$) and has trace one ($\text{Tr}\rho \equiv \sum_{i=1}^d |\rho_{ii}| = 1$). Any density matrix can be written as $\rho = \sum_i p_i |\psi_i\rangle\langle\psi_i|$ for at least one choice of $\{|\psi_i\rangle\}$, and if the set $\{|\psi_i\rangle\}$ are orthonormal then the p_i will be nonnegative probabilities that sum to unity. If in at least one orthogonal basis all p_i but one (say, $i = \alpha$) are equal to zero, $\text{Tr}\rho^2$ will equal one, and we say the system

¹Of course, we could just expand the definition of “system” at the expense of “environment” in order to include those (previously external) physical systems with which our original system has become correlated, though this is sometimes cumbersome in theoretical and experimental practice

is in a *pure state* $\rho = |\psi_\alpha\rangle\langle\psi_\alpha|$. Otherwise if more than one p_i are necessarily greater than zero, we say the state is *mixed*, and $P = \text{Tr}\rho^2$ is a measure of the degree of mixedness called the *purity*. Note that $\frac{1}{d} \leq P \leq 1$ for a qudit.

Although d linearly independent vectors suffice to span the space of *pure* states in \mathcal{H}_d , due to the greater complexity allowed by mixed states d^2 matrices are required to span the space of possible density operators. Note that these basis matrices need not necessarily be density operators themselves; for instance the basis $e_{jk} = |j\rangle\langle k|$ may suffice but for $j \neq k$ do not represent physical states. An orthonormal operator basis can be defined under the *Hilbert-Schmidt inner product* [2, p.76], defined for matrices A and B as $(A, B) = \text{Tr}(A^\dagger B)$.

The process whereby a system becomes mixed as a result of coupling to its environment is called *decoherence*. The off-diagonal terms in the density matrix (ρ_{ij} , $i \neq j$) are called the coherence terms as they describe the coherence between the basis states. Decoherence can be viewed as a loss of quantum information from the system into the local environment, specifically information about the coherence terms between basis states of the system. This tends to decrease the purity of the state needed to describe the system without reference to the environment, and will be discussed further in section 2.1.5.

2.1.1.2 Qubits

The simplest quantum system is two-dimensional i.e. has state space \mathcal{H}_2 . In QIP this is called a quantum bit or *qubit*. This is a direct quantum analogue of the (classical) bit, the simplest unit of classical information, which is a binary system with states **0** and **1**. A qubit has two logical basis states,

$$|0\rangle = \begin{bmatrix} 1 \\ 0 \end{bmatrix} \text{ and } |1\rangle = \begin{bmatrix} 0 \\ 1 \end{bmatrix}. \quad (2.1)$$

However, unlike a classical bit, a qubit can also occupy any superposition $|\psi\rangle = c_0|0\rangle + c_1|1\rangle$, with $|c_0|^2 + |c_1|^2 = 1$ if the state is normalized. The set $\{|0\rangle, |1\rangle\}$ is called the logical or computational basis for \mathcal{H}_2 .

A particularly useful operator basis for representing the state of a qubit in density matrix

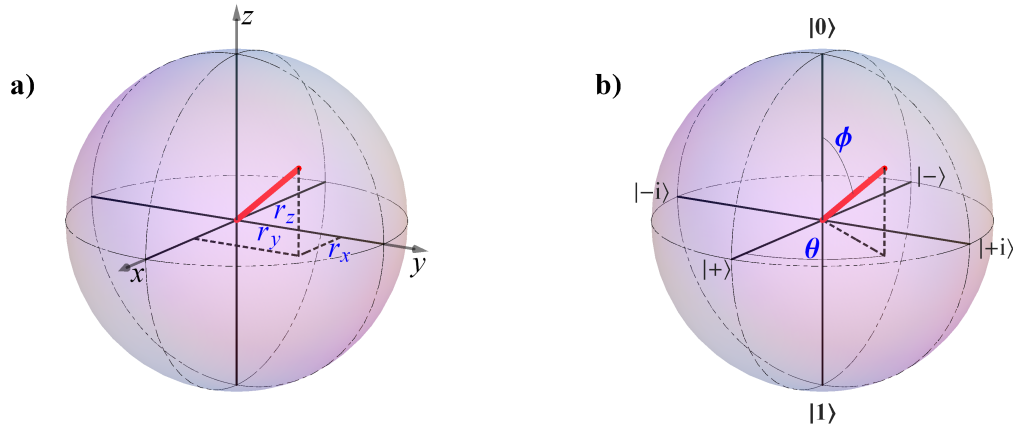


Figure 2.1: The Bloch sphere. a) A qubit state represented as a Bloch vector with Cartesian coordinates (r_x, r_y, r_z) . b) The same qubit state, but now represented as a Bloch vector with spherical polar coordinates ϕ and θ . In both cases $r = \sqrt{\sum_i r_i^2} = 1$, so the state shown is pure, but Bloch vectors with length $r < 1$ are also possible and represent mixed states. Whereas the only possible values for a classical bit are $\mathbf{0}$ and $\mathbf{1}$, equivalent to the ‘North pole’ and ‘South pole’ on a Bloch sphere, a qubit in contrast has a state-space isomorphic to the *entire surface* of the sphere, and even the interior of mixed states are considered.

form consists of the three 2×2 *Pauli matrices* and the identity matrix:

$$\begin{aligned}
 \sigma_1 = X &= \begin{bmatrix} 0 & 1 \\ 1 & 0 \end{bmatrix} & \sigma_2 = Y &= \begin{bmatrix} 0 & -i \\ i & 0 \end{bmatrix} \\
 \sigma_3 = Z &= \begin{bmatrix} 1 & 0 \\ 0 & -1 \end{bmatrix} & \sigma_0 = \mathbb{1} &= \begin{bmatrix} 1 & 0 \\ 0 & 1 \end{bmatrix}
 \end{aligned} \tag{2.2}$$

In this basis any arbitrary qubit state ρ can be written as²

$$\rho = \frac{\mathbb{1} + \vec{r} \cdot \vec{\sigma}}{2}, \tag{2.3}$$

where $\vec{\sigma} = (X, Y, Z)$, $|\vec{r}| \leq 1$, and \vec{r} is a vector whose components (r_x, r_y, r_z) are respectively given by the Hilbert-Schmidt inner product of the state with the respective Pauli operator, i.e. $r_i = \text{Tr}(\sigma_i \rho)$. The x -, y -, and z -axes will be called the *Bloch axes* as they serve to orient

² This equation can be simplified to $\rho = \frac{1}{2} \vec{r}' \cdot \vec{\sigma}'$ where $\vec{\sigma}'$ is the ordered set *including* σ_0 . However $\text{Tr}(\sigma_0 \rho) = \frac{1}{2}$ for *any* valid qubit state and thus the ‘ r'_0 -component’ of a state is neither useful nor necessary for orienting the state e.g. in the Bloch sphere representation.

the *Bloch sphere*, a useful representation of the state space of a qubit as a three-dimensional unit sphere, shown in Fig. 2.1. Points on the surface of the Bloch sphere represent possible pure qubit states, and points inside the sphere represent mixed states.

Notably, just as the state-space of a quantum bit is isomorphic to a ball—the surface and interior points of a sphere—so is the space of possible *polarization*-states of light. This is useful, as the polarization of a single photon forms a useful qubit! In the context of polarization, the ball is called the Poincaré sphere, and perhaps confusingly is often oriented differently, with the horizontal and vertical polarizations—usually taken to represent $|0\rangle$ and $|1\rangle$ in photonic quantum information studies—at the poles of the x -axis. The Poincaré sphere representation is used in Ch. 6.

The points at ± 1 on the three orthogonal axes of the Bloch sphere represent eigenstates of the respective Pauli operators:

$$\begin{aligned}
 \text{The eigenstates of } X : \quad & |\pm\rangle & \equiv \frac{1}{\sqrt{2}}(|0\rangle \pm |1\rangle) & \mapsto \frac{1}{2}(\sigma_0 \pm \sigma_1) \\
 \text{The eigenstates of } Y : \quad & |\pm i\rangle & \equiv \frac{1}{\sqrt{2}}(|0\rangle \pm i|1\rangle) & \mapsto \frac{1}{2}(\sigma_0 \pm \sigma_2) \\
 \text{The eigenstates of } Z : \quad & |0\rangle, |1\rangle & & \mapsto \frac{1}{2}(\sigma_0 \pm \sigma_3)
 \end{aligned} \tag{2.4}$$

Note that right-most terms above represent the states in density operator form whereas the others are in state vector form. These three eigenbases of the Pauli operators are here termed the *standard* bases, and the six states themselves the *standard* states.

Alternatively, an arbitrary qubit state can be written as

$$\rho(\phi, \theta, r) = r |\psi(\phi, \theta)\rangle\langle\psi(\phi, \theta)| + (1 - r)(\mathbb{1}/2), \tag{2.5}$$

where

$$|\psi(\phi, \theta)\rangle = \cos(\phi/2)|0\rangle + e^{i\theta} \sin(\phi/2)|1\rangle \tag{2.6}$$

and $\mathbb{1}$ is the identity matrix. Here $\phi \in [0, \pi)$ and $\theta \in [0, 2\pi)$ are the polar and azimuthal angles of ρ in the Bloch sphere representation, respectively, and $r = |\vec{r}| = \sqrt{2(\text{Tr}\rho^2 - \frac{1}{2})} \in [0, 1]$ is the radius of the state's Bloch vector. Note the straightforward relation between the Bloch radius and the purity $P = \text{Tr}\rho^2$. In the remainder of this thesis I may sometimes refer to a qubit's state vector, density operator, or Bloch vector as the *state* of the qubit; my meaning should be clear from the context.

Note finally that a qubit, like a classical bit, is a unit of information, but in any experimental application must be *represented* by the state of a physical system, or (more likely)

by a particular, defined subspace of states of a physical system. For instance, classical bits are represented in solid-state computer memory by a charge across a tiny capacitor, with some threshold separating the *high*-charge state **1** from the *low*-charge state **0**. Obviously, the charge on a capacitor cannot be simultaneously *above* and *below* the threshold, and thus the bit can only be on one state or the other.

Similarly, qubits must be represented by a physical system, *e.g.* the charge (or flux or phase) in a superconducting Josephson junction circuit, the spin orientation of an electron or nuclear particle, the ground and first excited energy levels of quantum dot, or the polarization of a single photon—which forms a particularly natural qubit as it has a Hilbert space of dimension 2. Notably, all of these can be in superpositions: qubits can in some sense be in both states at once.

2.1.2 State evolution

In quantum theory the evolution of any closed system must be described by a *unitary transformation*, represented by the action of a unitary operator. If the system is a qudit this operator can be represented by a $d \times d$ unitary matrix U ; U is unitary if and only if $U^\dagger U = \mathbb{1}$. In quantum theory, an operator \hat{O} acts on a state vector $|\psi\rangle$ as $\hat{O}|\psi\rangle$, and on other operators, including a density operator ρ , as $\hat{O}\rho\hat{O}^\dagger$.³ Unitary operators are trace-preserving and therefore purity-preserving, and also preserve inner products [2].

In non-relativistic quantum theory, the unitary evolution can be found by solving the Schrödinger equation, which relates the time-evolution of the state $|\psi(t)\rangle$ to the Hamiltonian operator \mathcal{H} , a hermitian operator quantifying the total energy of the system and whose eigenstates are energy eigenstates of the system:

$$i\hbar \frac{\partial |\psi(t)\rangle}{\partial t} = \mathcal{H}(t)|\psi(t)\rangle. \quad (2.7)$$

If \mathcal{H} is time-independent, the solution is simply $U = \exp(-i\mathcal{H}t/\hbar)$ and $|\psi(t)\rangle = U|\psi(0)\rangle$. An operator \hat{O} is hermitian if $\hat{O}^\dagger = \hat{O}$.

In QIP, it is useful to consider implementing specific unitary operations without reference to the generating Hamiltonian. Some important unitary operators on qubits have already been encountered: the Pauli operators in Eq. (2.2), which each act on a qubit state by rotating it by π about the respective Bloch axis. In fact, all unitary transformations on a qubit correspond to geometric rotations of the state in the qubit sphere. Other important examples include

³Hats will not always be used to denote operators in this thesis, as mostly they should be clear from the context.

rotations about the three Bloch axes by an *arbitrary* angle ξ :

$$X_{(\xi)} \equiv e^{-i\xi X/2}, \quad Y_{(\xi)} \equiv e^{-i\xi Y/2}, \quad Z_{(\xi)} \equiv e^{-i\xi Z/2}. \quad (2.8)$$

Any rotation in 3-space can be written in the Euler representation as a product of three rotations by arbitrary angles around two non-parallel axes, e.g. $U_{\text{rot}} = \hat{n}_{(\alpha)}\hat{m}_{(\beta)}\hat{n}_{(\gamma)}$. Thus, any unitary on a qubit can, for instance, be decomposed into three successive rotations about two different Bloch axes (see [2], pp.175-6.)

Another important unitary operation on qubits is the *Hadamard* operation H , which maps Z to X and vice-versa:

$$\begin{aligned} H &= \frac{1}{\sqrt{2}}(Z + X) &= \frac{1}{\sqrt{2}} \begin{bmatrix} 1 & 1 \\ 1 & -1 \end{bmatrix} \\ HZH &= X, & HXH &= Z, \\ H|0, 1\rangle &= |\pm\rangle, & H|\pm\rangle &= |0, 1\rangle. \end{aligned} \quad (2.9)$$

The purity-preserving properties of unitary operators are important, as one does not expect the purity of a closed quantum system to change. However, when the system is allowed to interact with other systems or more generally with its environment, the resulting evolution will be from a broader, more general class known as quantum processes. The only requirements for valid quantum processes is that when acting on physically-valid input states, they yield valid output states. General quantum processes will be discussed further in section 2.1.5, but first we must address the measurement of quantum states.

2.1.3 Quantum measurement

2.1.3.1 Projective measurements

In addition to density operators and unitary operators, another important type of operator in quantum theory is the *projection operator*, or *projector*. A projector P acting on a qudit in \mathcal{H}_d is used to find the *projection* of the qudit into an n -dimensional subspace W^n (where $n < d$.) In fact if $n = 1$ then P looks just like a pure state density operator $|\phi\rangle\langle\phi|$, where $|\phi\rangle$ is the state onto which one is projecting; if $1 < n \leq d$ then the projector is given by

$$P \equiv \sum_{j \in W^n} |\phi_j\rangle\langle\phi_j|, \quad (2.10)$$

where the entire set $\{|\phi_j\rangle\}$ forms a basis for \mathcal{H}_d . The action of a projector P on a state ρ can be interpreted as ‘filtering out’ only that part of ρ which lives in W^n (i.e. those components of ρ parallel to some $|\phi\rangle \in W^n$). Projectors are hermitian and also satisfy $P^2 = P$.

A projective measurement on a qudit is defined by an *observable* O , a hermitian operator acting on \mathcal{H}_d which can be written as⁴:

$$O = \sum_m \lambda_m P_m, \quad (2.11)$$

where $\{P_m\}$ are orthogonal projectors ($P_{m'}P_m = \delta_{m,m'}P_m$) that sum to unity ($\sum_m P_m = \mathbb{1}$), and P_m projects onto the eigenspace of O with eigenvalue λ_m [2, pp. 70 & 87-88]. When one performs a projective measurement on a system in state ρ , outcome m is obtained with probability $p(m) = \text{Tr}(P_m\rho)$, and the state ρ' of the system after measurement is

$$\rho' = \frac{P_m\rho P_m}{p(m)}. \quad (2.12)$$

The Hamiltonian \mathcal{H} from section 2.1.2 is an example of an observable; it corresponds specifically to the total system energy.

Clearly the number n of possible outcomes of a projective measurement on a qudit must be at most as large as the dimension d of the system being measured, or else the corresponding projectors could not all be orthogonal. The special case where $n = d$, and each P_m is a rank-one projector $P_m = |\phi_m\rangle\langle\phi_m|$ for some orthonormal basis $\{|\phi_m\rangle\}$, is called a Von Neumann measurement, a *complete* projective measurement, or to be specific a ‘measurement in the basis $\{|\phi_m\rangle\}$ ’. The simplest example is a measurement in the computational basis $\{|k\rangle\}$, $k = \{0, 1, \dots, d-1\}$. Note that measurement, in this formulation, causes an instantaneous change in the state of the system: before the measurement, the system may have been in a superposition of many eigenstates of the measured observable, and perhaps even in a mixed state, but afterwards it will be in a single pure eigenstate $|\psi_m\rangle$. Though there has been considerable debate over the best interpretation of this phenomenon it is often referred to as the collapse of the wavefunction.

Note finally that any complete projective measurement on a qudit specified by observable $\Omega = \sum_j \lambda_j |\psi_j\rangle\langle\psi_j|$ can be implemented as a unitary U on the system, followed by a projective measurement in the computational basis, where $U_{jk} = \langle\psi_j|k\rangle$ ⁵. For instance a measurement of X on a qubit can be accomplished by a Hadamard operation before a computational-basis

⁴This is called a spectral decomposition.

⁵Alternately, the columns of U^\dagger are the eigenvectors of Ω . All of this is a consequence of the spectral theorem.

measurement (see Eq. (2.9).)

Projective measurements have the nice property that it is straightforward to calculate their expectation value, which is the expected average of the outcome over many measurements on the same state. The average value $\langle O \rangle$ of an observable O for a state ρ , given by $\sum_m \lambda_m p(m)$, simplifies to $\text{Tr}(O\rho)$.

To measure an expectation value $\langle O \rangle$ in the laboratory, one can repeat the projective measurement on a large number n of identically prepared systems, recording the outcome $m_i, i \in \{1, \dots, n\}$, and then take the mean $(\sum_i \lambda_{m_i})/n$. However it is often the case (in particular when working with photons) that a measurement apparatus only records a single outcome, while the others are discarded. In this case, it is often more convenient to calculate the expectation value of the observable from the expectation values of the projectors. The expectation value of a projector P_m for a state ρ is just the probability $p(m)$ that ρ is found in the subspace W_m associated with P_m .

For example, in laboratory measurements it is possible to measure the value of a projector on the unknown state of identically-prepared photons by counting photon arrivals at detectors. Each $p(m) = \text{Tr}(P_m\rho)$ can be calculated from easily-measurable quantities such as the photon arrival rates, suitably normalized. The expectation value of the observable is then given by the weighted average of the average values of the projectors: $\langle O \rangle = \sum_m \lambda_m \langle P_m \rangle = \sum_m \lambda_m p(m)$.

In addition to being unitary operators and forming a Hilbert-Schmidt-orthogonal operator basis for qubits, the Pauli matrices $\{\sigma_j\}$ are all also important qubit observables, especially in the context of quantum state tomography (section 2.1.6). A measurement of Z is a measurement in the computational basis of a qubit.

2.1.3.2 Fidelity of states

In quantum information it is often desirable to quantify the ‘closeness’ of two quantum states ρ_1 and ρ_2 . A conventional metric to quantify this closeness is the *fidelity*, which, if at least one of the two states is pure e.g. $\rho_1 = |\phi\rangle\langle\phi|$, is given by

$$F(|\phi\rangle\langle\phi|, \rho_2) = \langle\phi|\rho_2|\phi\rangle. \quad (2.13)$$

This has a nice interpretation: it is equivalent to $F(P, \rho_2) = \text{Tr}(P\rho_2)$ where P is the projector $|\phi\rangle\langle\phi|$, and this is just the probability that ρ_2 will be projected onto $|\phi\rangle$. Like any probability, F varies between 0, meaning ρ_2 is orthogonal to ρ_1 , and 1 meaning $\rho_2 = P = \rho_1$. For two pure qubit states in the Bloch sphere representation, the fidelity can be calculated via a convenient

geometrical relation: if the states are separated by a central angle ζ , then

$$F = \cos^2 \left(\frac{\zeta}{2} \right). \quad (2.14)$$

A generalization of the fidelity to mixed states should: (i) reduce to Eq: 2.13 if one of the states is pure, (ii) yield $F = 1$ if $\rho_1 = \rho_2$, and (iii) yield $F = 0$ if ρ_1 is orthogonal to ρ_2 . The function which accomplishes this is given by [3]:

$$F(\sigma, \tau) = \left[\text{Tr} \left(\sqrt{\sqrt{\sigma} \tau \sqrt{\sigma}} \right) \right]^2. \quad (2.15)$$

Unfortunately, this definition of the fidelity does not have a physical interpretation which this author finds to be as intuitive or enlightening when both states are mixed as when at least one is pure.

2.1.3.3 Generalized measurements and POVMs

The formalisms of mixed states and general quantum processes serve both to greatly simplify some calculations and to provide a mathematical representation which may bring different physical features to light, in some cases enabling different insights. The formalism of generalized measurements or POVMs can serve the same purposes with respect to quantum measurement theory.

A general quantum measurement on a qudit can be represented by any set of operators $\{M_m\}$ acting on \mathcal{H}_d such that $\sum_m M_m^\dagger M_m = \mathbb{1}$. In particular, $\{M_m\}$ need not be projectors, nor need they be orthogonal, and the number n of possible measurement outcomes may be greater than d . After a measurement $\{M_m\}$ is performed on a system in state ρ yielding outcome m , the resulting state will be

$$\rho' = \frac{M_m \rho M_m^\dagger}{p(m)}, \quad (2.16)$$

where $p(m) = \text{Tr}(M_m^\dagger M_m \rho)$ is the probability that outcome m is obtained. We can define $M_m^\dagger M_m = E_m$, and $\{E_m\}$ will then be a set of positive operators such that $\sum_m E_m = \mathbb{1}$ and $p(m) = \text{Tr}(E_m \rho)$. The set $\{E_m\}$ is called a POVM for *Positive Operator-Valued Measure*. Any n -outcome POVM can be implemented by performing a projective measurement on some \mathcal{H}_n , of which \mathcal{H}_d is a subspace. In practice this means that any POVM on a physical system S with associated Hilbert space \mathcal{H}_d^S can be implemented by coupling the system to some

ancillary system A (which may itself be a composite system), and performing a projective measurement in the combined Hilbert space $\mathcal{H}_d^S \otimes \mathcal{H}^A$ [4, pp. 283-289].

2.1.4 Quantum correlations and entanglement

Quantum states in a composite Hilbert space $\bigotimes^i \mathcal{H}^i$ can be simple tensor products of states in the subsystems $\bigotimes^i |\psi\rangle_i$, where $|\psi\rangle_i \in \mathcal{H}^i$. For instance, for a composite system of two qubits $\mathcal{H} = \mathcal{H}^A \otimes \mathcal{H}^B$, such product states include $|0\rangle_A \otimes |0\rangle_B$, $|0\rangle_A \otimes |1\rangle_B$, $|1\rangle_A \otimes |0\rangle_B$, $|1\rangle_A \otimes |1\rangle_B$, or any $|\phi\rangle_A \otimes |\chi\rangle_B$. We often omit the tensor product, the labels, and even the separate kets, writing e.g. $|00\rangle$, understood to mean $|0\rangle_A \otimes |0\rangle_B$. Such a state is called separable, and a mixed state is said to be separable if it can be written as a convex sum of separable states: $\rho = \sum_i p_i (\rho_A)_i \otimes (\rho_B)_i$ where $\{p_i\}$ are positive and sum to one.

However, due to the superposition principle (p. 8) any normalized sum of valid states is *also* a valid state, including those that cannot be written as a product state. Important examples include the *Bell states*, named after J. S. Bell due to his seminal work on entanglement and its consequences [5]:

$$|\Phi^\pm\rangle = \frac{1}{\sqrt{2}}(|00\rangle \pm |11\rangle) \quad |\Psi^\pm\rangle = \frac{1}{\sqrt{2}}(|01\rangle \pm |10\rangle). \quad (2.17)$$

The Bell states form an often-convenient orthonormal basis for $\mathcal{H}_2 \otimes \mathcal{H}_2$, hereafter called the *Bell basis*. Another example of entangled states is the family of so-called Greenberger-Horne-Zeilinger or GHZ states [6], $|GHZ\rangle_n = \frac{1}{\sqrt{2}}(|0\rangle^{\otimes n} + |1\rangle^{\otimes n})$.

These states have several interesting and (some might say) counter-intuitive properties which have incited much research and debate in the history of quantum theory, its interpretation or foundations, and quantum information. Consider performing a measurement in the computational basis on one qubit (say A) from a Bell state, without measuring qubit B : both outcomes are equally probable. In fact, if particle B is discarded or ignored, the outcomes will be equiprobable for *any* binary observable on A : in other words, qubit A appears to be maximally-mixed. However, consider measuring *both* qubits in the computational basis: although the specific outcome of the measurement on the first qubit is completely random, it completely determines the outcome of the measurement on the second qubit. For the $|\Phi\rangle$ states the outcomes will be perfectly correlated; for the $|\Psi\rangle$ states they will be anticorrelated. In 1935 Einstein, Podolsky, and Rosen famously used these correlations as the basis of an argument against the completeness of quantum theory [7].

Remarkably, the strength of these correlations is independent of the measurement basis. For instance the ‘singlet’ state $|\Psi^-\rangle$ can be written as $\frac{1}{\sqrt{2}}(|\psi\rangle|\psi_\perp\rangle - |\psi_\perp\rangle|\psi\rangle)$ for *any* orthonormal basis $\{|\psi\rangle, |\psi_\perp\rangle\}$. Thus the measurement outcomes in such a basis will always be perfectly anticorrelated, and the outcomes of measuring A and B respectively in two different bases will be imperfectly correlated in a straightforward way⁶. Furthermore, the correlations persist even if qubits A and B are spacelike-separated at the time of measurement so that neither measurement can properly be said to have occurred ‘first,’ regardless of inertial reference frame. Bell’s famous theorem shows that these correlations are stronger than would be possible for classical systems, which always inhabit defined states rather than superpositions [5], and experimental tests confirm that the correlations observed for some systems in nature obey the predictions of quantum theory, rather than conforming to classically intuitive notions [8–11].

Viewed as a resource, entanglement enables many of the most famous and useful experiments and applications in quantum information and quantum computing, including Bell inequality violations, quantum teleportation (see section 2.1.7) quantum key distribution [12–19], and cluster-state quantum computation [20, Sec. 2.2.2]. In fact, entanglement is widely conjectured to be a critical factor in explaining the increased efficiency of quantum computation for some tasks [21].

2.1.4.1 The partial trace

Examined on its own, each subsystem of an entangled quantum system will appear at least partially mixed. This becomes apparent when one uses the partial trace operation to examine each subsystem individually. My discussion of the partial trace closely follows that in Ref. [2, pp.105-107]. Our example will be two subsystems labeled A and B in the state ρ_{AB} . The state of subsystem A is given by using the partial trace to ‘trace out’ subsystem B , denoted by

$$\rho_A = \text{Tr}_B(\rho_{AB}). \quad (2.18)$$

Let $|a_1\rangle$ and $|a_2\rangle$ be any two different wavefunctions in \mathcal{H}_A , and $|b_1\rangle$ and $|b_2\rangle$ be any two different wavefunctions in \mathcal{H}_B . Then the partial trace is defined as the unique linear operation

⁶In particular if observable $r_A \cdot \vec{\sigma}$ is measured on qubit A and $r_B \cdot \vec{\sigma}$ is measured on qubit B , where $r_{A(B)}$ are two different pure-state Bloch vectors, then the expectation value of the product of the two observables $\langle r_A \cdot \vec{\sigma} \otimes r_B \cdot \vec{\sigma} \rangle$ is given by $-r_A \cdot r_B$ [5].

which satisfies

$$\mathrm{Tr}_B(|a_1\rangle\langle a_2| \otimes |b_1\rangle\langle b_2|) \equiv |a_1\rangle\langle a_2| \mathrm{Tr}(|b_1\rangle\langle b_2|) = |a_1\rangle\langle a_2| \langle b_1|b_2\rangle. \quad (2.19)$$

The state ρ_A determined via tracing out subsystem B is called the reduced density operator for system A .

To see that tracing out over part of an entangled system yields mixture for the remaining subsystem, let us take as an example a maximally-entangled state, specifically the Bell state $|\Phi^+\rangle = \frac{1}{\sqrt{2}}(|0\rangle_A \otimes |0\rangle_B + |1\rangle_A \otimes |1\rangle_B)$. We then have

$$\rho_{AB} = \frac{|00\rangle\langle 00| + |11\rangle\langle 00| + |00\rangle\langle 11| + |11\rangle\langle 11|}{2}, \quad (2.20)$$

and

$$\begin{aligned} \rho_A &= \mathrm{Tr}_B(\rho_{AB}) & (2.21) \\ &= \frac{\mathrm{Tr}_B(|00\rangle\langle 00|) + \mathrm{Tr}_B(|11\rangle\langle 00|) + \mathrm{Tr}_B(|00\rangle\langle 11|) + \mathrm{Tr}_B(|11\rangle\langle 11|)}{2} \\ &= \frac{\langle 0|0\rangle |0\rangle\langle 0| + \langle 0|1\rangle |1\rangle\langle 0| + \langle 1|0\rangle |0\rangle\langle 1| + \langle 1|1\rangle |1\rangle\langle 1|}{2} \\ &= \frac{|0\rangle\langle 0| + |1\rangle\langle 1|}{2} \\ &= \frac{\mathbb{1}}{2}. \end{aligned}$$

This is a maximally-mixed state because our qubits are maximally entangled; in general the degree of mixedness of the traced-out subsystem will be correlated with the degree of entanglement of said subsystem to the remainder of the system.

2.1.5 General quantum processes

As stated in section 2.1.2, unitary operators cannot adequately describe all the processes that can happen to a quantum state. Measurement is an important example of a non-unitary process. However, even in the absence of measurement, unitary operations are insufficient to describe quantum systems which are not completely isolated, often termed *open* quantum systems. The preceding discussions of entanglement and the partial trace yield a hint as to why. Imagine for instance a quantum system A initially in a pure state $\rho(t=0) = |\psi\rangle\langle\psi|$ which subsequently, through purely unitary evolution, becomes entangled with another system B . At the end of this process, if we trace out system B , system A will necessarily appear mixed.

In other words, interaction with outside systems leads to purity-reducing and thus non-unitary evolution for the reduced density operator for system A .

Analogously to the way density operators are needed to represent mixed states of non-isolated systems, more general quantum operations \mathcal{E} are needed to describe the evolution of non-closed systems. Just as unitary operations for closed quantum systems stem from evolution under a Hamiltonian, non-unitary quantum processes result from finite-time evolution under a global Hamiltonian, the effects of which on the system can be treated using quantum master equations, described further in Sec. 2.1.5.1. If we are interested in the evolution of a quantum system initially in state ρ , which then interacts with some (initially un-correlated) environment ρ_{env} via the unitary evolution U of the combined system, then the quantum process \mathcal{E} which yields the final reduced density matrix of the system ρ is defined by

$$\mathcal{E}(\rho) = \text{Tr}_{\text{env}} [U(\rho \otimes \rho_{\text{env}})U^\dagger]. \quad (2.22)$$

There are at least three different mathematical ways of representing general quantum processes, which are described in more detail in Refs. [22, pp.20-23] and [2, Ch. 8]. The first, the operator-sum representation, stems from the intuitive idea of a general process \mathcal{E} occurring when many pure operators $\{E_j\}$ (which could include both unitary and measurement operators), suitably normalized, are probabilistically applied to a state ρ ; such a process yields decoherence and a reduction in state purity if the minimum number of non-zero elements E_j needed to describe the process is greater than one. Such a *superoperator*, as quantum processes represented in this way are termed, acts on a state as

$$\mathcal{E}(\rho) = \sum_j E_j \rho E_j^\dagger, \quad (2.23)$$

and the operators must satisfy the inequality $\sum_j E_j^\dagger E_j \leq \mathbb{1}$ in order for the state to be physically valid. If the inequality is saturated the process is said to be trace-preserving; otherwise it will decrease the trace of the state and thus represents loss.

Given an orthonormal operator basis $\{A_m\}$, $\text{Tr}(A_m^\dagger A_n) = \delta_{mn}$, the operators $\{E_j\}$ can be expanded in this basis as $E_j = \sum_m a_{jm} A_m$ and the output of the operation can be written as

$$\mathcal{E}(\rho) = \sum_{mn} (\chi_{\mathcal{E}})_{mn} A_m \rho A_n^\dagger \quad (2.24)$$

where $\chi_{\mathcal{E}}$ is called the *process matrix* and has elements $(\chi_{\mathcal{E}})_{mn} = \sum_j a_{jm} a_{jn}^*$. This process matrix representation resolves some of the ambiguity inherent in the operator-sum represen-

tation, where different sets of operators $\{E_j\}$ can represent the same physical process; the process matrix $\chi_{\mathcal{E}}$ is unique given the choice of an operator basis $\{A_m\}$. Further the process matrix has several analagous properties to the density matrix: recall from Sec. 2.1.1.1 that with density matrices, the diagonal elements ρ_{jj} represent the occupation of the basis states $|\psi_j\rangle\langle\psi_j|$ while the off-diagonal elements represent coherences between basis states. Similarly, in a process matrix $\chi_{\mathcal{E}}$ the diagonal elements $(\chi_{\mathcal{E}})_{jj}$ represent the occurrence probabilities of the different operators E_j while the off-diagonal elements represent the coherences between these pure process operators.

A third, and quite useful, way of representing quantum processes relies on the *Jamiolkowski isomorphism* between quantum states and quantum processes [23]. Every quantum process \mathcal{E} acting on \mathcal{H}_d can be mapped to an abstract quantum state $\rho_{\mathcal{E}}$ called the process state or Choi matrix:

$$\rho_{\mathcal{E}} \equiv (\mathbb{1} \otimes \mathcal{E})(|\Phi_{\max}\rangle\langle\Phi_{\max}|), \quad (2.25)$$

where $|\Phi_{\max}\rangle = \frac{1}{\sqrt{d}} \sum_j |\psi_j\rangle_A |\psi_j\rangle_B$ is a maximally-entangled state acting on $\mathcal{H}_d \otimes \mathcal{H}_d$, and $\{|\psi_j\rangle\}$ is an arbitrary orthonormal basis for \mathcal{H}_d . Given the process state $\rho_{\mathcal{E}}$, the output state resulting from the process acting on ρ can be calculated as

$$\mathcal{E}(\rho) = \text{Tr}_A \{(\rho^T \otimes \mathbb{1})\rho_{\mathcal{E}}\}. \quad (2.26)$$

This representation has several useful features discussed in more detail in Ref. [22], but in particular allows for straightforward calculation of the *process purity* and *process fidelity* by analogy with the calculation of state purity and state fidelity. The process purity is calculated as

$$P_{\text{process}}(\mathcal{E}) = \text{Tr}(\rho_{\mathcal{E}}^2), \quad (2.27)$$

and quantifies the amount of decoherence induced by the process \mathcal{E} . Meanwhile the process fidelity between two quantum processes \mathcal{E} and \mathcal{G} , one of which is pure, can simply be calculated as

$$F(\mathcal{E}, \mathcal{G}) = \text{Tr}\{\rho_{\mathcal{E}}^\dagger \rho_{\mathcal{G}}\}, \quad (2.28)$$

which is closely analagous to Eq. (2.13).⁷

⁷Just as the state fidelity which requires a slightly more complex definition when neither of the states is pure, the process fidelity also requires a slightly more complex definition when neither process is pure; this

The Jamiolkowski isomorphism is used to find the fidelity of candidate circuits for heralded entangling quantum gates in Ch. 8.

2.1.5.1 Open quantum systems and master equations

Just as unitary evolutions of closed quantum systems stem from finite-time evolution under the system's Hamiltonian as described in section 2.1.2, general quantum processes stem from finite-time evolution of an open system and the environment with which it interacts. Determining the continuous-time evolution of the system, often without a complete description of the environment, is accomplished via quantum master equations. A complete description of open quantum systems theory [24] is beyond the scope of this thesis but some relevant points will be summarized here. My treatment largely follows ref. [25].

Let $\rho_{\text{Tot}}(t)$ be the total density operator of a system interacting with an environment; $\rho(t) = \text{Tr}_{\text{env}}(\rho_{\text{Tot}})$ is the reduced density operator of the system. The total system will still evolve unitarily according to Schrödinger's equation, or more specifically according to the Liouville-von Neumann equation which is the density-operator equivalent of the Schrödinger equation:

$$\frac{d\rho_{\text{Tot}}}{dt} = -\frac{i}{\hbar}[\mathcal{H}_{\text{Tot}}, \rho_{\text{Tot}}], \quad (2.29)$$

where $[\cdot, \cdot]$ represents the commutator, and \mathcal{H}_{Tot} is the total system Hamiltonian.

One can approximate the total Hamiltonian as $\mathcal{H}_{\text{Tot}} = \mathcal{H}_s + \mathcal{H}_{\text{env}} + \mathcal{H}_{S,\text{env}}$, consisting of a local Hamiltonian for the system \mathcal{H}_S , one for the environment \mathcal{H}_{env} , and a term $\mathcal{H}_{S,\text{env}}$ governing their coupling.

Via several approximations—in particular the *Born approximation* that the system-environment coupling is sufficiently weak, so that the total state is always well-approximated as a non-entangled product state, and the *Markov approximation* that the environment is 'memory-less' (e.g. $\rho_{\text{env}}(\tau + \delta t)$ depends only on $\rho_{\text{env}}(\tau)$ and not on $\rho_{\text{env}}(t < \tau)$)—one can derive the dynamics of the reduced system density operator as a *Lindblad form* master equation:

$$\frac{d\rho}{dt} = -\frac{i}{\hbar}[\mathcal{H}_S, \rho(t)] + \sum_j \left[2L_j\rho(t)L_j^\dagger - L_j^\dagger L_j\rho(t) - \rho(t)L_j^\dagger L_j \right]. \quad (2.30)$$

can be found in Ref. [22].

Here the L_j are Lindblad operators which represent the system-environment coupling and must be derived for a specific case by consideration of the specific physics of the system and environment.

Lindblad-form master equations can be applied to the study of decoherence in continuous-time quantum walks (CTQWs), as well as the physically-related phenomenon of quantum transport in noisy systems, discussed further in the next chapter. In Ch. 7 the experimental simulation of open quantum systems using coupled arrays of optical waveguides is explored, and compared with a theoretical description using Lindblad quantum master equations.

2.1.6 Quantum tomography

In quantum theory no single measurement can completely determine the state ρ of a quantum system. This is because, after an observable is measured on a system, the subsequent state of that system will be an eigenstate of that observable, nullifying the chance to obtain information about the original state with respect to other observables. However, it is possible to estimate ρ for a large number of *identically-prepared* systems via a finite number of measurements of different observables. This task is called quantum state tomography (QST) and is a valuable tool for assessing the outcomes of experiments and the success of quantum information, computation, and communication protocols.

As an illustrative example, let us consider tomography of the state of a single qubit. Recall from equation 2.3 that the state ρ of a single qubit can be expanded in terms of the Pauli matrices as $\frac{1}{2} + \frac{1}{2} \sum_j \text{Tr}(\sigma_j \rho) \sigma_j$. Because these operators are linearly independent and span the qubit Hilbert space they are said to be *tomographically complete*; the Pauli matrices for a qubit have the added benefit of being orthogonal under the Hilbert-Schmidt inner product. Recall that $\text{Tr}(\sigma_j \rho)$ is the average value of an *observable*, and as such can be measured in the lab as described on p. 15. Measuring the average value of each σ_j amounts to determining the three (Cartesian) coordinates of the state's Bloch vector, which uniquely determine the state. Quantum state tomography of a qubit is illustrated schematically in Fig. 2.2.

One need not even measure all six projectors corresponding to the six standard states (the eigenstates of $\{\sigma_j\}$); projections onto one eigenstate of each σ_j are sufficient to determine ρ : the $2^2 = 4$ parameters of a qubit are constrained by normalization so that there are really only three *free* parameters. However in practice the normalization rate usually also needs to be determined, which necessitates a fourth projection; a standard tomographic set is then to measure the average values of the projectors $\{|0\rangle\langle 0|, |1\rangle\langle 1|, |+\rangle\langle +|, |+i\rangle\langle +i|\}$. In practice

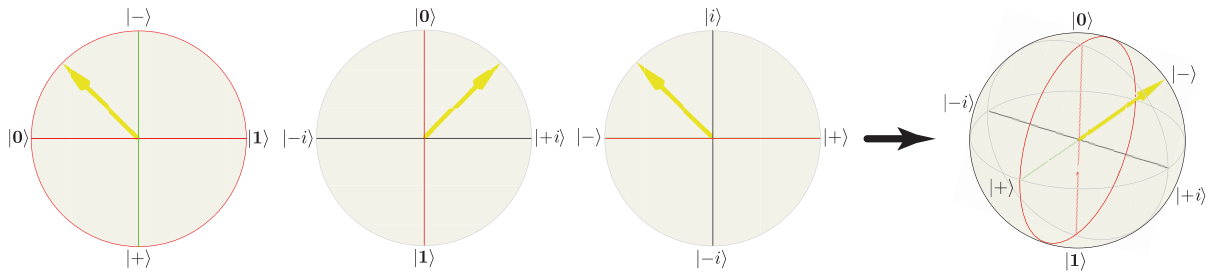


Figure 2.2: An illustration of quantum state tomography of a qubit. Given many identically-prepared qubits, one can estimate the state in which they were prepared by determining the average values of the projections of the qubits onto the axes of the Bloch sphere. Reproduced with permission courtesy of M. Broome.

a more accurate reconstruction can be obtained by measuring the projections onto all six standard states [22]. Such a set is an example of an *overcomplete* tomographic set, so called because they contain more projectors than required to span the Hilbert space.

State tomography extends easily to larger quantum systems: Any set of d^2 linearly independent operators acting on \mathcal{H}_d are tomographically complete and will allow determination of the qudit state. In particular, the state of a composite system of n qubits can be tomographically reconstructed using measurements of observables which are tensor products of Pauli operators, e.g. $\bigotimes_{i=1}^n \sigma_j^i$, $j \in \{x, y, z\}$. James *et. al.* showed that measurements of 4^n projections are sufficient for tomographic reconstruction [26]. However, again overcomplete tomography with 6^n projections leads to more accurate reconstructions.

An additional problem is that, due to measurement noise (e.g., in the case of counting photons, the aforementioned Poissonian fluctuations) sometimes the density matrix ρ_r estimated via standard techniques (linear tomography) is not physically valid: it may have negative eigenvalues, or eigenvalues greater than unity. A solution is to find the physically valid quantum state which is most likely to have produced the obtained measurement results. This technique is called *maximum-likelihood tomography*, and is detailed further in refs. [22, 26].

Quantum process tomography (QPT) is formally quite similar to state tomography; however in QPT the goal is to reconstruct a quantum process by controlling the input states to the process and measuring a large number of output states for each input state. For QPT not only the set output measurements but also the set of input states must be tomographically complete, meaning for the latter that it spans the Hilbert space of possible input states. QPT is described in further detail in Ref. [22]. The coherent-light tomography discussed in

Ch. 6 is equivalent to tomographic reconstruction of a single-qubit process in the combined spatial-mode and polarization Hilbert space.

2.1.7 Teleportation

As an example of a useful quantum information protocol as well as an introduction to the circuit model of quantum computation, I will briefly describe the *quantum teleportation* of a qubit state. My treatment of teleportation largely follows Ref. [27].

Consider two separated parties, Alice and Bob, who share an entangled state $|\Phi^+\rangle$, i.e. they each have one qubit from the state. Further, Alice also has a qubit in the pure state $|\psi\rangle$ which she would like to transmit to Bob. Using only classical communication, this would normally require a double-infinity of classical bits to fully specify the arbitrary real numbers θ and ϕ (see Eq. 2.5). However, by exploiting the shared entangled state we will see that Alice can allow Bob to recreate her qubit by sending him only two classical bits. This is called quantum teleportation.

The protocol can be explained as follows: the initial state of the three qubits is $|\psi\rangle \otimes |\Phi^+\rangle$. However, the state of the two qubits in Alice's possession can be rewritten in the Bell basis:

$$|\psi\rangle|\phi^+\rangle = \frac{1}{2} [|\Phi^+\rangle|\psi\rangle + |\Psi^+\rangle(X|\psi\rangle) + |\Phi^-\rangle(Z|\psi\rangle) + |\Psi^-\rangle(XZ|\psi\rangle)]. \quad (2.31)$$

Alice measures her two qubits in the Bell basis and transmits the result to Bob, encoded in two classical bits as follows:

$$\begin{aligned} |\Phi^+\rangle &\mapsto \mathbf{00} & |\Psi^+\rangle &\mapsto \mathbf{01} \\ |\Phi^-\rangle &\mapsto \mathbf{10} & |\Psi^-\rangle &\mapsto \mathbf{11} \end{aligned} \quad (2.32)$$

To complete the protocol, Bob performs a Z operation on his qubit if and only if the first bit of his received message is $\mathbf{1}$, and likewise an X on his qubit if and only if the second bit is $\mathbf{1}$ (otherwise performing the identity operation $\mathbb{1}$.) Bob's resulting output state will be $|\psi\rangle$.

The teleportation protocol is shown in the form of a *quantum circuit diagram* in Fig. 2.3. Note that Alice's measurement of her two qubits in the Bell basis, or Bell-state measurement (BSM) is shown as a unitary—specifically a CNOT operation (see Sec. 2.2.1) and a Hadamard—followed by a measurement in the computational basis. However this is not the only possible means of performing a BSM, and the teleportation protocol succeeds regardless of the method used.

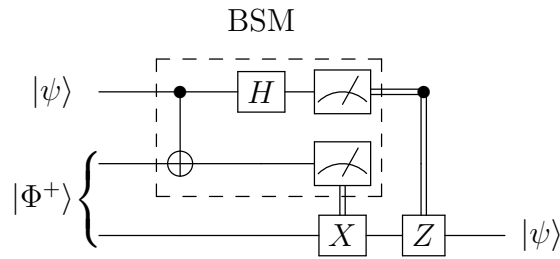


Figure 2.3: Teleportation circuit. The top two rails represent Alice’s qubits whereas the bottom represents Bob’s. Alice possesses a qubit in the (possibly unknown) state $|\psi\rangle$ as well as one qubit from a $|\Phi^+\rangle$ Bell pair; Bob has the other. Alice measures the combined state of her two qubits in the Bell basis (Bell-state measurement (BSM)) and encodes the measurement result in two cbits sent to Bob. The cbits control which Pauli operation(s) Bob performs on his qubit, which will then be left in state $|\psi\rangle$.

2.2 Quantum computing

2.2.1 The quantum network model

Quantum computers promise great speedups in solving certain classes of problems and in simulating physical systems [2]. The most common model of quantum computation is the quantum circuit or network model $QC_{\mathcal{N}}$, which is an analogue of the circuit model of classical computation based on boolean operators such as NOT, AND and NAND. In $QC_{\mathcal{N}}$, quantum bits (qubits) are prepared in some initial state, usually some fiduciary state such as $|0\rangle^{\otimes n}$, and then propagated through a succession of *gates*, which represent unitary operators acting on one, two, or more qubits. The final state of the qubits after these operations constitutes the output of the quantum computation.

The diagram shown for quantum teleportation, Fig. 2.3, represents a quantum circuit, which processes quantum information in $QC_{\mathcal{N}}$: In this diagram the horizontal lines are called *quantum wires*, and each represents the progression through time of a qubit. Boxes on quantum wires represent quantum gates, which act on the qubits passing through the box with the unitary operation denoted by the contents of the box. Vertical lines with boxes or other markers at the endpoints (on quantum wires) also represent multiple-qubit gates, unitary operations involving the qubits on those quantum wires. Meters represent measurements, usually taken to be Von Neumann measurements in the computational basis. Double-lines

represent classical information flow (in this case the outcome of the computational basis measurements).

The processing of quantum information in the $QC_{\mathcal{N}}$ model proceeds by enacting the operations represented by the gates in the circuit diagram, in left-to-right order, on some input state of qubits. Important single-qubit gates already encountered include the Pauli operators (Eq. (2.2)), general rotations in the Bloch sphere (Eq. (2.8)), and the hadamard operator (Eq. (2.9)).

Gates involving multiple qubits are of course essential for quantum computation and in particular for the creation and measurement of entanglement. A crucial step in the development of quantum computing theory was the realization that all possible quantum computations could, in fact, be performed using only many instances of arbitrary single-qubit gates⁸ as well as any two-qubit gate representing a unitary which could transform some input two-qubit product state into a maximally-entangled state [27]. In other words, such maximally-entangling gates along with arbitrary single-qubit operations form a *universal gate set*.

Frequently-used maximally-entangling gates include *controlled* operations, where the state of one qubit input to the gate, termed the *control* qubit, determines whether or not a specific single-qubit unitary is applied to the second qubit, often termed the *target*. The following represents an important two-qubit gate, the controlled- Z or CZ gate.

$$\begin{array}{c}
 \begin{array}{c} \bullet \\ | \\ \bullet \end{array} \equiv \begin{array}{c} \bullet \\ | \\ \boxed{Z} \end{array} = \begin{array}{c} \boxed{Z} \\ | \\ \bullet \end{array} \\
 \equiv \begin{bmatrix} 1 & 0 & 0 & 0 \\ 0 & 1 & 0 & 0 \\ 0 & 0 & 1 & 0 \\ 0 & 0 & 0 & -1 \end{bmatrix} \quad (2.33)
 \end{array}$$

Here the small bullet indicates that the bulleted qubit *controls* the action of the connected gate: the connected operation occurs if the control is in state $|1\rangle$, but not if the control is in state $|0\rangle$. The action of the CZ gate is such that it can equivalently be described as a Z operation on the second qubit, controlled by the first, or as a Z on the first, controlled by the second. Another important two-qubit gate is the controlled- X , CX , or CNOT, where the latter term stems from viewing the Pauli X operation as the qubit equivalent of a classical

⁸In fact arbitrary $QC_{\mathcal{N}}$ computations can be performed with an arbitrarily-small error using only a maximally-entangling gate and a *discrete* set of single-qubit rotations.

NOT gate on a single bit.

$$\begin{array}{c}
 \begin{array}{ccc}
 \begin{array}{c} \bullet \\ | \\ \text{---} \\ | \\ \square X \\ | \\ \text{---} \end{array} & \equiv & \begin{array}{c} \bullet \\ | \\ \text{---} \\ | \\ \oplus \\ | \\ \text{---} \end{array} \\
 \equiv & & \begin{array}{c} \left[\begin{array}{cccc} 1 & 0 & 0 & 0 \\ 0 & 1 & 0 & 0 \\ 0 & 0 & 0 & 1 \\ 0 & 0 & 1 & 0 \end{array} \right] \\
 \end{array}
 \end{array} \tag{2.34}
 \end{array}$$

Either of these is said to be an *entangling gate* because for some input product state $|\psi\rangle|\chi\rangle$, the output will be maximally entangled. As an example, if the input state to the c-NOT is $|+0\rangle = \frac{1}{\sqrt{2}}(|00\rangle + |10\rangle)$, meaning the control qubit is in $|+\rangle$ and the target qubit in $|0\rangle$, the output will be $\frac{1}{\sqrt{2}}(|0\rangle|0\rangle + |1\rangle X|0\rangle) = \frac{1}{\sqrt{2}}(|00\rangle + |11\rangle)$, the $|\Phi^+\rangle$ Bell state. Note also that, just as the X and Z gates are related by the Hadamard operation by Eq. (2.9), the CNOT and CZ gates are related by Hadamards on the target qubit:

$$\begin{aligned}
 (\mathbb{1} \otimes H) \times CX \times (\mathbb{1} \otimes H) &= CZ, \text{ and} \\
 (\mathbb{1} \otimes H) \times CZ \times (\mathbb{1} \otimes H) &= CX.
 \end{aligned} \tag{2.35}$$

2.3 Conclusion

Armed with the basic tools of quantum information processing and a description of quantum computation, we proceed in the next chapter to discuss photonic implementations of QIP specifically before covering quantum simulation and quantum walks in chapter 4.

References

- [1] Feynman, R. Simulating physics with computers. *Int. J. Theor. Phys.* **21**, 467–488 (1982). 7
- [2] Nielsen, M. & Chuang, I. *Quantum Computation and Quantum Information* (Cambridge Univ. Press, Cambridge, 2000). 7, 9, 12, 13, 14, 18, 20, 26
- [3] Jozsa, R. Fidelity for mixed quantum states. *J. Mod. Opt.* **41**, 2315–2324 (1994). 16
- [4] Peres, A. *Quantum theory: concepts and methods* (Dordrecht: Kluwer, 1993). 17
- [5] Bell, J. On the Einstein Podolsky Rosen paradox. *Physics* **1**, 195–200 (1964). 17, 18
- [6] Greenberger, D. M., Horne, M. A. & Zeilinger, A. Going beyond bell’s theorem. In Kafatos, M. (ed.) *Bell’s Theorem, Quantum Theory, and Conceptions of the Universe*, 73–76 (Kluwer, Dordrecht, 1989). 17
- [7] Einstein, A., Podolsky, B. & Rosen, N. Can quantum-mechanical description of physical reality be considered complete? *Phys. Rev.* **47**, 777–780 (1935). 17
- [8] Clauser, J., Horne, M., Shimony, A. & Holt, R. Proposed experiment to test local hidden-variable theories. *Phys. Rev. Lett.* **23**, 880 (1969). 18
- [9] Aspect, A., Grangier, P. & Roger, G. Experimental realization of Einstein-Podolsky-Rosen-Bohm gedankenexperiment: A new violation of Bell’s inequalities. *Phys. Rev. Lett.* **49**, 91–94 (1982). 18
- [10] Weihs, G., Jennewein, T., Simon, C., Weinfurter, H. & Zeilinger, A. Violation of Bell’s inequalities under strict Einstein locality conditions. *Phys. Rev. Lett.* **81**, 5039–5043 (1998). 18
- [11] Rowe, M. *et al.* Experimental violation of Bell’s inequality with efficient detection. *Nature* **409**, 791–794 (2001). 18
- [12] Bennett, C. H. & Brassard, G. Quantum cryptography: Public key distribution and coin tossing. In *Proceedings of the IEEE International Conference on Computers, Systems, and Signal Processing*, 175 (New York, 1984). 18
- [13] Ekert, A. Quantum cryptography based on Bell’s theorem. *Phys. Rev. Lett.* **67**, 661 (1991). 18

- [14] Bennett, C., Brassard, G. & Mermin, N. Quantum cryptography without Bell's theorem. *Phys. Rev. Lett.* **68**, 557 (1992). 18
- [15] Bennett, C., Brassard, G., Salvail, L. & Smolin, J. Experimental quantum cryptography. *Journal of Cryptology* **5**, 3 (1992). 18
- [16] Gisin, N., Ribordy, G., Tittel, W. & Zbinden, H. Quantum cryptography. *Rev. Mod. Phys.* **75**, 145–195 (2002). 18
- [17] Beveratos, A. *et al.* Single photon quantum cryptography. *Phys. Rev. Lett.* **89**, 187901 (2002). 18
- [18] Hughes, R., Nordholt, J., Derkacs, D. & Peterson, C. Practical free-space quantum key distribution over 10km in daylight and at night. *New J. Phys* **4**, 43.1 (2002). 18
- [19] Marcikic, I., Lamas-Linares, A. & Kurtsiefer, C. Free-space quantum key distribution with entangled photons. *Appl. Phys. Lett.* **89**, 101122 (2006). 18
- [20] Biggerstaff, D. N. *Experiments with generalized quantum measurements and entangled photon pairs*. Master's thesis, University of Waterloo (2009). 18
- [21] Steane, A. Quantum computing. *Rep. Prog. Phys.* **61**, 117 (1998). 18
- [22] Langford, N. K. *Encoding, Manipulating and Measuring Quantum Information in Optics*. Ph.D. thesis, University of Queensland (2007). 20, 21, 22, 24
- [23] Jamiołkowski, A. Linear transformations which preserve trace and positive semidefiniteness of operators. *Rep. Math. Phys.* **3**, 275 – 278 (1972). 21
- [24] Breuer, H.-P. & Petruccione, F. *The Theory of Open Quantum Systems* (Oxford University Press, USA, 2007). 22
- [25] Mülken, O. & Blumen, A. Continuous-time quantum walks: Models for coherent transport on complex networks. *Phys. Rep.* **502**, 37–87 (2011). 22
- [26] James, D. F. V., Kwiat, P. G., Munro, W. J. & White, A. G. Measurement of qubits. *Phys. Rev. A* **64**, 052312 (2001). 24
- [27] Kaye, P., LaFlamme, R. & Mosca, M. *An Introduction to Quantum Computing* (Oxford Univ. Press, Oxford, 2007). 25, 27

Chapter 3

Quantum information experiments with photons

Thus far quantum computation and simulation have been outlined mostly in general terms, independent of the physical system used for implementation. However the experiments in this thesis were carried out using optical implementations. This chapter provides a short introduction to optical quantum information science focusing on generation and manipulation of single optical photons.

3.1 The quantized optical field

Photons are elementary quanta of the electromagnetic field and were the first quantum particles hypothesized, first as part of Max Planck's efforts to derive a phenomenologically adequate description of the blackbody radiation spectrum, and later by Albert Einstein to explain the photoelectric effect [1, 2].

The following discussion of photons was inspired in part by Refs. [3, 4]. Modes of the quantum electromagnetic field are described by field operators a_j and a_j^\dagger , respectively called annihilation and creation operators, which respectively decrease or increase by one the number of photons in optical mode j :

$$a_j |n_j\rangle = \sqrt{n_j} |n_j - 1\rangle \quad (3.1)$$

$$a_j^\dagger |n_j\rangle = \sqrt{n_j + 1} |n_j + 1\rangle. \quad (3.2)$$

The operator $a_j^\dagger a_j$ is called the number operator and has the action

$$a_j^\dagger a_j |n_j\rangle = n_j |n_j\rangle. \quad (3.3)$$

States of a single optical mode with well-defined photon number $|n_j\rangle$, $n \in \{0, 1, 2, \dots\}$, are called Fock states, and form an orthonormal basis for the state of that optical mode, as well as a well-defined although infinite-dimensional Hilbert space. As photons are bosons, *i.e.* indistinguishable and with states that are symmetric under particle exchange if the photons are in the same mode, the field operators obey the commutation relations

$$[a_j, a_k] = 0 \quad (3.4)$$

$$[a_j^\dagger, a_k^\dagger] = 0 \quad (3.5)$$

$$[a_j^\dagger, a_k] = \delta_{jk}. \quad (3.6)$$

The hamiltonian describing the quantized optical field modes is given by

$$\mathcal{H}_{\text{EM}} = \sum_j \hbar\omega_j \left(a_j^\dagger a_j + \frac{1}{2} \right), \quad (3.7)$$

where ω_j is the angular frequency of the j th mode, and the factor of $\frac{1}{2}\omega_j$ is called the zero-point or vacuum energy. In this thesis we generally are interested in *single* photons, which can be represented as a superposition of creation operators for many modes acting on a multimode vacuum state $|\mathbf{0}\rangle$:

$$|\psi^{(1)}\rangle = \left[\sum_j c_j a_j^\dagger \right] |\mathbf{0}\rangle \quad (3.8)$$

Here the $|c_j|$ represent the population of the photon in mode j , or the probability of finding the photon in the j th mode after a von Neumann measurement in the mode basis. Given the Hamiltonian above, the time evolution can be found by solving the Schrödinger equation, yielding

$$|\psi^{(1)}(t)\rangle = \left[\sum_j c_j e^{i\omega_j t} a_j^\dagger \right] |\mathbf{0}\rangle. \quad (3.9)$$

Each mode-component of the photon accumulates phase at a rate dependent on the angular frequency in that mode, as expected.

In quantum information with low-number Fock states (*i.e.* with one or a few photons) it

is often useful to work in the Heisenberg picture, where the field operators undergo unitary temporal evolution instead of the states. For example, the effect on the creation operator for a mode j of propagating a distance L in free space would be

$$a_j^\dagger \rightarrow e^{i\omega_j L/c} a_j^\dagger, \quad (3.10)$$

where c is the speed of light. Should a single photon be in mode j , its state would of course transform as

$$a_j^\dagger|0\rangle = |1_j\rangle \rightarrow e^{i\omega_j L/c} a_j^\dagger|0\rangle = e^{i\omega_j L/c} |1_j\rangle. \quad (3.11)$$

Often it is easier during calculations to work exclusively in terms of evolving field operators and apply them all to the vacuum at the end of the computation in order to determine the amplitudes and Fock occupancies of modes. A much more in-depth discussion contrasting the Heisenberg and Schrödinger pictures for quantum optics can be found in Ref. [4].

3.2 Encoding photonic qubits

Single optical photons are in several respects ideal for quantum information protocols: they travel at the speed of light for quick communication, they are relatively easy to manipulate—especially, as we shall see, when encoded in polarization—and perhaps most importantly they interact weakly with other electromagnetic fields and with many transparent matter media, leading to exceptionally low decoherence rates in free space and in guiding media for optical communications such as optical fiber. This property renders them ideal for communicating quantum information. However, it poses a problem as well: due to their weak interaction, multi-qubit gates are experimentally difficult to implement. Furthermore, both reliable, deterministic sources of isolated single photons and highly efficient detectors have proven difficult to achieve, the latter especially if *non-demolition* detection is desired, meaning detecting the photon without destroying it *i.e.* through absorption in the detector. Before addressing some means used to overcome these difficulties, I will address the encoding of photons for quantum information processing.

By restricting a single photon, represented as in Eq. (3.8), to d orthogonal modes, one obtains a qudit. If these modes are orthogonal longitudinal spatial modes, *i.e.* different spatial paths for the photon propagation, this is often called path-encoding or multi-rail encoding. In particular, if restricting to superpositions of only two modes $\mathbf{0}$ and $\mathbf{1}$, a general state of a

photon in these two modes takes the form

$$\begin{aligned} (c_0 a_0^\dagger + c_1 a_1^\dagger) |\mathbf{0}\rangle &= c_0 |1\rangle_0 |0\rangle_1 + c_1 |0\rangle_0 |1\rangle_1 \\ &= c_0 |0\rangle + c_1 |1\rangle \end{aligned} \quad (3.12)$$

where—to clarify notation— $|\mathbf{0}\rangle$ (**boldface**) still represents a general multimode optical vacuum state, but in the last line $|0\rangle$ and $|1\rangle$ now represent logical qubit states of a single photon, as opposed to the Fock occupancy of a mode. If the two modes are again longitudinal spatial paths this is termed dual-rail encoding. This is the most important encoding scheme for the experiments presented in this thesis.

Many other possibilities exist for the two optical modes representing the qubit computational basis states. A particularly natural choice for many photonic quantum information processing (QIP) applications is to use the polarization state of the optical field, which naturally has a Hilbert space of dimension two. This encoding scheme has been used in *e.g.* entangling quantum gates [5], implementations of quantum cryptographic protocols [6], and discrete-time quantum walks (DTQWs) in bulk optics [7], and is thoroughly reviewed in Refs. [3, 4].

When encoded in polarization, defined as the direction of the electric field vector, the convention is to represent the logical basis states $|0\rangle$ and $|1\rangle$ by the orthogonal horizontal and vertical polarization components $|H\rangle$ and $|V\rangle$, respectively. The eigenstates of the X and Y operators are then respectively represented by the (Anti-)Diagonal and Right/Left circular polarization components as follows:

$$\begin{aligned} |0\rangle &\mapsto |H\rangle & |1\rangle &\mapsto |V\rangle \\ |+\rangle &\mapsto |D\rangle & |-\rangle &\mapsto |A\rangle \\ |+i\rangle &\mapsto |L\rangle & |-i\rangle &\mapsto |R\rangle. \end{aligned} \quad (3.13)$$

Besides polarization, the other degrees of freedom of a single photon are its *time-frequency* and *spatial-momentum* distributions. Photons have been entangled in the former, both in the form of time-bin entanglement *e.g.* [8] and frequency entanglement *e.g.* [9, 10]. Dual-rail encoding and path entanglement [11] are examples of longitudinal spatial mode encoding, but photons can also be encoded and entangled in their transverse spatial mode, see *e.g.* Ref. [12]. Note that the given references represent just a sample of the many experiments using these encoding schemes. It is also possible to create photon pairs entangled in multiple degrees of freedom, *e.g.* $\frac{1}{2}(|HH\rangle + |VV\rangle) \otimes (|1\rangle_0 |0\rangle_1 + |0\rangle_0 |1\rangle_1)$, where $\mathbf{0}$ and $\mathbf{1}$ once again label two

longitudinal spatial modes, but all the encoding is done on the same two photons (i.e. the first position in each ket refers to the same photon). This is termed hyperentanglement.

3.2.1 Manipulating photons: Beamsplitters and phase-shifters

In an important result, all unitary operations on photons can be accomplished using two classes of elements: phase shifters which impart a phase between two optical modes, and beamsplitters which coherently mix them [13]. In the most general formulation; this applies to all encodings of optical qubits, but the phase-shifting and beam-splitting elements will take different forms depending on the encoding. Phase shifters implement the unitary

$$U_{\text{PS}} = e^{i\phi a_k^\dagger a_k} \quad (3.14)$$

on a photon in mode k , where the phase induced is ϕ . Beamsplitters, in the symmetric convention, transform two modes a_1 and a_2 as

$$\text{BS}(\theta): \quad a_1^\dagger \rightarrow a_1^\dagger \cos \theta + i a_2^\dagger \sin \theta, \quad a_2^\dagger \rightarrow a_2^\dagger \cos \theta + i a_1^\dagger \sin \theta, \quad (3.15)$$

where θ controls the reflectivity of the beamsplitter, and would for instance take the value $\pi/2$ for a conventional 50/50 splitting operation.

In dual-rail encoding, phase shifters can be implemented by changing the optical path length experienced by one rail, either by adding physical length or by a refractive index increase in part of the path. Beamsplitters meanwhile are implemented by partially-reflecting mirrors or dielectric stacks.

In polarization-encoding, by contrast, both elements are implemented through the use of birefringent elements, described in further detail below. Such elements have two different refractive indices depending on the orientation of the polarization of the incident light field with respect to birefringent axes in the material. These can be used to form waveplates, which introduce a phase between two orthogonal polarizations and are described further in Sec 3.2.3. Waveplates can implement a phase shift on a polarization mode relative to the orthogonal mode if oriented with its birefringent axes parallel to those respective modes, but can also act as beamsplitters between those modes when the birefringent axes are oriented differently.

3.2.2 Manipulating polarization-encoded photons: birefringence

A common way of manipulating the polarization of light is through the use of *birefringent* materials. These are materials for which the light will experience a different index of refraction and therefore travel at a different speed depending on its polarization with respect to the crystallographic axes of the material. Of course, the index of refraction also depends on the frequency; the following best applies to monochromatic plane waves. My discussion of birefringence and optical components employing this effect is drawn from Refs. [4, 14, 15]. Regardless of the direction of propagation and angle of incidence, any birefringent medium will split the incoming light into two *normal modes*, orthogonal polarization states which are unchanged by propagation through the medium (they're eigenstates of the transformation it induces on the polarization state). Generally light in one of these modes will travel faster through the medium than light in the other, and thus the normal modes define a 'fast axis' and 'slow axis', both perpendicular to the direction of propagation. The simplest birefringent materials are *uniaxial* meaning they have a single crystallographic axis of symmetry, the *optic axis* \hat{a}_o . Light polarized parallel to this axis is said to have *extraordinary* polarization and will experience an index of refraction n_e , while light polarized perpendicular to \hat{a}_o is said to be *ordinary* and will experience an index n_o .

Consider a beam propagating through a uniaxial material, without loss of generality along the axis z . If $z = \hat{a}_o$ then all polarizations of the beam are ordinary. Otherwise z and \hat{a}_o define a *principal plane*; any component of the beam polarized perpendicular to this plane will be ordinary and experience index of refraction n_o , while the component in the plane is called the *e-ray* and will experience an index $n(\theta)$ defined by:

$$\frac{1}{n^2(\theta)} = \frac{\cos^2 \theta}{n_o^2} + \frac{\sin^2 \theta}{n_e^2}, \quad (3.16)$$

where θ is the angle between z and \hat{a}_o .

When the optic axis is neither parallel nor perpendicular to the direction of propagation of the beam as it enters the crystal, birefringent media can lead to the effect of *double refraction* or *walkoff*,¹ where the ordinary-polarized component of the input ray and the extraordinary-polarized component refract at different angles. For an angle of incidence θ_i , the angles of

¹sometimes called spatial walkoff, as it involves differing propagation directions in the crystal for *e*- and *o*-rays, to distinguish it from temporal walkoff which results from a difference in the *phase velocities* of *e* and *o* polarizations.

refraction θ_o and θ_e of the o - and e -rays are given by a modified Snell's law:

$$\begin{aligned}\sin \theta_i &= n_o \sin \theta_o \\ \sin \theta_i &= n(\theta_e) \sin(\theta_e),\end{aligned}\tag{3.17}$$

where $n(\theta_e)$ is given by Eq. (3.16). A thorough treatment of this and related birefringent phenomena can be found in Ref. [15].

3.2.3 Waveplates

An important optical component constructed from birefringent materials, in particular quartz, is the phase retarder or waveplate. These are birefringent uniaxial crystals cut and mounted such that the optic axis is parallel to the entrance face, and therefore one component of the incoming beam always experiences n_e and the perpendicular component n_o . The difference in refractive index means that the e -component will have experienced a phase shift $\Delta\phi$ relative to the o -component when they exit the waveplate, given by $\Delta\phi = k_0 d |n_o - n_e|$, where d is the thickness of the plate and k_0 the magnitude of the wavevector of the incident light in free space.

The action of a waveplate with the optic axis oriented horizontally is described (up to an unimportant global phase) by the Jones matrix:

$$U_{wp}(\phi) = \begin{bmatrix} e^{i\phi/2} & 0 \\ 0 & e^{-i\phi/2} \end{bmatrix}.\tag{3.18}$$

Notice that this is the same operator as for a rotation about the *Bloch* z -axis by ϕ .

The action in the H, V -basis of any polarizing optical component when rotated by an angle θ from the horizontal around the direction of propagation can be found by applying the two-dimensional rotation operator² $R(-\theta)$ to the corresponding Jones matrix, where

$$R(\theta) = \begin{bmatrix} \cos \theta & \sin \theta \\ -\sin \theta & \cos \theta \end{bmatrix}.\tag{3.19}$$

For instance the action of a ϕ -waveplate, rotated around the direction of propagation by θ is

$$U_{rwp}(\phi, \theta) \equiv R(-\theta)U_{wp}(\phi)R^\dagger(-\theta) = R(-\theta)U_{wp}(\phi)R(\theta).\tag{3.20}$$

²The basis in which the optical element operates is related by a rotation of *positive* θ to the H, V -basis, therefore the transformation to find its action in the H, V -basis is a rotation by *negative* θ .

This is a fairly general unitary, describing a rotation by ϕ about the *real* superposition of the computational basis states (i.e. the linear polarization) making an angle *in the Bloch sphere* of θ with $|H\rangle$.

Fortunately, most applications do not require control over the retardance ϕ of a waveplate, but rather use combinations of just two: the *half-waveplate* (HWP)

$$\begin{aligned} HWP(\theta) &= -iU_{rwp}(\pi, \theta) \\ &= \begin{bmatrix} \cos 2\theta & \sin 2\theta \\ \sin 2\theta & -\cos 2\theta \end{bmatrix}, \end{aligned} \quad (3.21)$$

and the *quarter-waveplate* (QWP), which I define for my calculations as

$$\begin{aligned} QWP(\theta) &= iU_{rwp}\left(\frac{-\pi}{2}, \theta\right) \\ &= \frac{1}{\sqrt{2}} \begin{bmatrix} i + \cos 2\theta & \sin 2\theta \\ \sin 2\theta & i - \cos 2\theta \end{bmatrix}. \end{aligned} \quad (3.22)$$

These are called as such because they retard one polarization by a half (quarter) wavelength with respect to the other. Note that the global phases ($-i$ and i respectively) are added only for convenience, and also that $HWP(0) = Z$, $HWP(\pi/4) = X$, and $HWP(\pi/8) = H$. Finally, notice that the HWP and QWP operators are both unitary and Hermitian.

QWPs can transform linear polarizations to elliptical, and vice-versa, while HWPs can rotate any linear polarization to any other, or rotate the axes of the ellipse of an elliptically polarized beam. An arbitrary unitary rotation can be achieved by concatenating three waveplate rotations at arbitrary angles, specifically in the order $QWP(\alpha)HWP(\beta)QWP(\gamma)$ or QHQ [4]. It is interesting to contrast this decomposition of an arbitrary unitary—into rotations about three arbitrary linear-polarization axes by two fixed amounts (π and $\frac{\pi}{2}$)—with the Euler decomposition (p. 13) of an arbitrary unitary into rotations by three arbitrary angles about two different fixed non-parallel axes.

Birefringence can also be used to construct several types of *polarizing beamsplitters*, devices which separate an input beam into two orthogonally-polarized and spatially-separated output modes. If one looks only at one output mode of a polarizing beamsplitter, i.e. by blocking or simply failing to detect the other mode, then their action is to project onto a single polarization, and their action is given by e.g. $|H\rangle\langle H|$ or $|V\rangle\langle V|$, depending on the output mode considered. These devices can be used to interface path- and polarization-encoded photonic qubits.

3.3 Creating Photons through Spontaneous Parametric Downconversion

While several methods exist for producing photons for use in quantum information tasks, the most successful and widely-applied has doubtless been *spontaneous parametric downconversion* (SPDC) in nonlinear crystals [16]. The presentation of this material draws on Refs. [4, 17, 18], which can be seen along with references therein for further information.

SPDC is a non-linear optical process relying on the second-order coefficient $\chi^{(2)}$ of the polarization response of some media to an applied propagating electromagnetic field. In SPDC a high-energy “pump” field is mixed with two lower-energy vacuum fields, known for historical reasons as the *signal* and *idler*, in such a nonlinear medium. This three-wave mixing process is described by an interaction Hamiltonian of the form

$$\mathcal{H} = \gamma(\chi^{(2)})a_s^\dagger a_i^\dagger a_p + \gamma(\chi^{(2)})a_s a_i a_p^\dagger, \quad (3.23)$$

where the a_j and a_j^\dagger are respectively annihilation and creation operators for a photon in the j^{th} mode. The first term in this Hamiltonian describes SPDC while the second describes the reverse process *sum-frequency generation* (SFG). While SFG is a classical effect describable via Maxwell’s equations, SPDC admits no such classical description due to the mixing of pump light with previously-unpopulated vacuum fields and is thus a distinctly quantum-mechanical effect.

Although SPDC can lead to higher order photon-number states in the signal and idler fields (i.e. multiple photons in the same mode at the same time instead of one photon each in the signal and idler modes), the coupling constant γ is small enough in most media that even with bright coherent pump fields the vacuum and single-photon terms vastly exceed the multi-photon terms.

3.3.1 (Quasi-)Phase Matching Conditions

In the downconversion process energy must be conserved, and usually for any significant efficiency momentum must be nearly conserved among the three photons as well³. Usually this

³For crystals of finite length, momentum will not be *exactly* conserved between the three photons, but only approximately.

requires that the signal and idler frequencies sum to the pump frequency, and their wavevectors sum to the pump wavevector. These conditions require the three interacting fields to be in phase along their direction of propagation and are thus often called the *phase-matching conditions*. This is often accomplished via manipulating the geometry of the interaction such that the indices of refraction of the pump, signal and idler fields are matched for certain propagation directions (with respect to the crystallographic axes) and polarization directions of each field; these are respectively called angle phase-matching and birefringent phase-matching.

A more recently-developed technique takes advantage of *periodically-poled* crystal structures, where the nonlinear material is specially grown such that its effective nonlinearity is flipped with a period equal to the coherence length of the pump and signal/idler phases. This allows for *quasi-phase-matching*, where the effective wavevector of the structure contributes to the momentum conservation condition, allowing greater experimental freedom for the pump and downconversion directions, wavelengths, and polarizations [17]. In particular, the poling period and operating temperature can be tuned such that the signal and idler are orthogonally polarized and all three propagation directions are collinear along one of the crystallographic axes. This rids the interaction of the birefringent walkoff problems that plague angle- and birefringent-phase-matched downconversion setups, and thereby allows for much longer crystals, and thus longer interaction times and higher SPDC rates.

3.4 Conclusion

This chapter provides the basics in laboratory creation and manipulation of single photons which underlie the experiments described in the remainder of this thesis. The next chapter will describe the theory of optical quantum simulations and quantum walks, the subjects of photonic experiments in chapters 5, 6, and 7.

References

- [1] Planck, M. On the law of distribution of energy in the normal spectrum. *Annalen der Physik* **4**, 553 (1901). [31](#)
- [2] Einstein, A. Concerning an heuristic point of view toward the emission and transformation of light. *Annalen der Physik (Translated into English by American Journal of Physics, 33, 1965)* **17**, 132 (1905). [31](#)
- [3] Broome, M. A. Photonic quantum information and quantum walks (2012). [31](#), [34](#)
- [4] Langford, N. K. *Encoding, Manipulating and Measuring Quantum Information in Optics*. Ph.D. thesis, University of Queensland (2007). [31](#), [33](#), [34](#), [36](#), [38](#), [39](#)
- [5] O’Brien, J. L., Pryde, G. J., White, A. G., Ralph, T. C. & Branning, D. Demonstration of an all-optical quantum controlled-not gate. *Nature* **426**, 264 (2003). [34](#)
- [6] Bennett, C., Bessette, F., Brassard, G., Salvail, L. & Smolin, J. Experimental quantum cryptography. *Journal of Cryptology* **5**, 3 (1992). [34](#)
- [7] Broome, M. A. *et al.* Discrete single-photon quantum walks with tunable decoherence. *Phys. Rev. Lett.* **104**, 153602 (2010). [34](#)
- [8] Franson, J. D. Bell inequality for position and time. *Phys. Rev. Lett.* **62**, 2205–2208 (1989). [34](#)
- [9] Law, C. K., Walmsley, I. A. & Eberly, J. H. Continuous frequency entanglement: Effective finite hilbert space and entropy control. *Phys. Rev. Lett.* **84**, 5304–5307 (2000). [34](#)
- [10] Barreiro, J. T., Langford, N. K., Peters, N. A. & Kwiat, P. G. Generation of hyperentangled photon pairs. *Phys. Rev. Lett.* **95**, 260501 (2005). [34](#)
- [11] Boschi, D., Branca, S., Martini, F. D., Hardy, L. & Popescu, S. Experimental realization of teleporting an unknown pure quantum state via dual classical and Einstein-Podolsky-Rosen channels. *Phys. Rev. Lett.* **80**, 1121–1125 (1998). [34](#)
- [12] Mair, A., Vaziri, A., Weihs, G. & Zeilinger, A. Entanglement of the orbital angular momentum states of photons. *Nature* **412**, 313–316 (2001). [34](#)
- [13] Reck, M., Zeilinger, A., Bernstein, H. & Bertani, P. Experimental realization of any discrete unitary operator. *Phys. Rev. Lett.* **73**, 58–61 (1994). [35](#)

-
- [14] Hecht, E. *Optics* (Addison Wesley, San Francisco, 2002), fourth edn. 36
- [15] Saleh, B. & Teich, M. *Fundamentals of Photonics* (John Wiley & Sons Inc., Hoboken, N.J., 2007), second edn. 36, 37
- [16] Burnham, D. C. & Weinberg, D. L. Observation of simultaneity in parametric production of optical photon pairs. *Phys. Rev. Lett.* **25**, 84–87 (1970). 39
- [17] Fedrizzi, A. *Fundamental experiments with a high brightness source of entangled photons*. Ph.D. thesis, Universität Wien (2008). 39, 40
- [18] Resch, K. J. *Making photons talk to each other—Nonlinear optics in the quantum domain*. Ph.D. thesis, University of Toronto (2002). 39

Chapter 4

Quantum simulation and quantum walks

4.1 Introduction to quantum simulation

The simulation of physical systems is a crucial task in modern science. It allows for relatively quick and easy testing and optimization of parameters for engineering and design problems, as well as the ability to generate specific predictions from theoretical models, either for comparison with experiment or in cases where experiments would be expensive, difficult, or even impossible. Many quantum systems of interest are hard to control and thus to study in detail; quantum systems are also notoriously difficult to simulate. This notion was famously made explicit by Richard Feynman in 1982, who also hinted at a solution: create quantum simulators (Qs) which function according to the laws of quantum mechanics [1]. The idea behind quantum simulation is to map the dynamics of such a quantum system of interest onto the dynamics of another quantum system which is more readily controllable.

While modern computers rely on quantum mechanics for the functioning of transistors and gates, the information they store and manipulate is fundamentally classical: it is in the form of bits, each of which has only two possible states, zero and one. However, even the simplest quantum system, with only two levels, can be in any of an uncountably infinite number of states, each consisting of a superposition of those two levels. The state of N two-level quantum systems, or qubits, thus requires 2^N complex numbers to specify, in contrast to N classical 2-level systems which could be specified with only N bits. Furthermore calculating the dynamics of such a quantum system requires exponentiating matrices of size $2^N \times 2^N$. In other words, the

difficulty of classically simulating quantum systems grows exponentially with the size of the system, making the simulation of even moderately-sized quantum systems into a demanding task. When the resources required for a computational problem scale exponentially with the size of the problem rather than only polynomially, it is said to be computationally inefficient. The simulation of many quantum systems is known to be inefficient on a classical computer. Certainly efficient approximate classical computational methods exist for many problems *e.g.* density functional theory for finding molecular electronic states [2]; however all of these are limited to calculating certain properties on quantum systems that are well-behaved for some definition thereof [3]. For many other quantum problems all such approximation methods fail and the solutions are provably¹ in a complexity class which is not efficiently calculable on a classical computer. In contrast, quantum simulations of at least some such systems could be made efficient, at least in theory.

Seth Lloyd proved in 1996 that a *universal* quantum computer (QC) would also function as a universal quantum simulator (UQS) [4]. There has been significant theoretical and experimental progress towards universal quantum computation in architectures including neutral atoms, ion-traps, superconducting quantum devices, isolated spins in semiconductors, and linear optics. However, a large-scale universal quantum computer (UQC) with fully-implemented quantum error correction is still likely to be decades in the future, assuming that the significant technical obstacles are ever overcome sufficiently to build one at all.

However, a useful QS need not necessarily be *universal*—capable of simulating *any* other quantum system of sufficiently small size—nor need it be *digital*—working via quantum gates, and thus dependent on quantum error correction like universal quantum computation. In particular, interest has grown recently in the possibility that purpose-built, dedicated, analog QSS, designed to simulate only a particular quantum system or class of systems, may be practically demonstrable far more easily than UQCs. Such devices are likely to be among the first quantum information processing (QIP) devices to outperform a classical computer, *i.e.* to solve a problem which is intractable with current classical computers and algorithms [3]. Such a feat has been estimated to require only a few tens of well-controllable qubits [3].

4.1.1 Quantum simulation procedure

The implementation of a useful quantum simulation requires three main steps:

1. Initialize a quantum state representing the initial state of the system to be simulated.

¹Provably insofar as computational complexity theorists ever prove such results, which is debatable.

2. Apply quantum dynamics to evolve this initial state.

In the simplest case the temporal evolution of the system being simulated is generated by a known, potentially time-dependent Hamiltonian \mathcal{H} , and the evolution during a specific interval is described by a unitary operator $U = \exp(-i\hbar\mathcal{H}t)$, where t is the simulation time. However, instead of a simple unitary the evolution could conceivably be any general quantum process as described in section 2.1.5. In particular, non-unitarity might be unavoidable due to experimental imperfections leading to loss or decoherence, but might also be intended for the purpose of simulating either general open-system quantum dynamics, or dissipative dynamics in order to prepare a particular stationary state [5].

3. Measure the output state so as to obtain the desired information.

Note that the final state cannot be determined with a single measurement as this would collapse any superposition. For this reason the simulation should be designed such that at least one property of interest can be determined from one or a small number of measurements on the output state, and preferably via collective measurements instead of individual measurements on each subsystem. Examples of such output quantities include the collective magnetization of a set of spins [6] and the spectra of operators [3].

4.1.2 Digital versus analog quantum simulation

Quantum simulators can be classified according to different criteria: universal quantum simulators versus those dedicated to a specific problem or class of problems; closed-system versus open-system quantum simulators; as well as physical implementation of course. However perhaps the most significant distinguishing factor is between digital and analog quantum simulations [3, 7]. While the same three steps are required to carry out the simulation in either case, the method of implementing them differs significantly.

In a digital quantum simulator (DQS) the initial state must first be encoded in the qubits of the input register of the QC. This is sometimes straightforward, as when simulating a system of consisting of many initially-unentangled spin-1/2 particles; in this case the state in the spin basis $\{|\uparrow\rangle, |\downarrow\rangle\}$ is mapped directly to the computational basis $\{|0\rangle, |1\rangle\}$. However in other cases, such as when the initial state represents the ground state of a system of spins in a complicated potential or the wavefunction of molecular orbitals in real space, quantum computational algorithms are themselves required to find this initial state, determine its representation in the computational basis, and prepare that input register.

The evolution of the initial state must then be effected by applying a sequence of quantum logic gates. Methods for obtaining the efficient decomposition into gates are known in some cases. Crucially, such methods are *stroboscopic* in that they require approximating the continuous temporal evolution through a large but finite number of smaller time steps: $U = \exp(-i\hbar\mathcal{H}t) \approx \exp(-i\hbar\mathcal{H}\Delta t)^{t/\Delta t}$. The most widely known such method is called the Trotter approximation², and applies in the case that the Hamiltonian is well-approximated by a sum of many *local* Hamiltonians $\mathcal{H} = \sum_k \mathcal{H}_k$ (*i.e.* interactions between subsystems are limited in range.) In this case the Trotter formula states

$$U \approx \left(\prod_k \exp(-i\mathcal{H}_k\Delta t) \right)^{t/\Delta t}, \quad (4.1)$$

and the accuracy of this approximation obviously increases as the time step Δt is decreased.

Analog quantum simulators (AQSs), by contrast, require no quantum gates or encoding, but the dynamics of the system of interest are mapped—at least in part—to another, more easily controllable quantum system. Not all the dynamics need be simulated; rather the level of detail needed will depend on the properties being investigated. For instance the AQS may often be simulating a theoretical toy model such as an effective many-body Hamiltonian [7]. In general the couplings between particles in an AQS will be constant, or slowly varying in the case of a time-dependent simulated Hamiltonian, although the additional implementation of fast controllable local unitary interactions is also possible [5]. There is therefore no need for stroboscopically discretizing the time evolution as in Trotterization.

Notably, in order for the quantum simulation to be efficient, each step—initial state preparation, time evolution, and measurement—must be performed efficiently. This is not possible in general. The preparation of general quantum states of N qubits requires $\Omega(2^N)$ quantum gates³ and is therefore inefficient, however many states of physical interest can be prepared efficiently through known algorithms or adiabatic methods [8, 9]. In digital quantum simulation, arbitrary Hamiltonians cannot be efficiently reduced to stroboscopic application of gate sequences via Trotterization or similar methods, and even when such methods are possible they often scale poorly when significant quantum error correction techniques are included [5]. For AQSs, in contrast, there is no proven methods of error correction or guarantee of fault tolerance; however such devices are often “expected to be more robust against imperfections than a [digital] quantum computer” [6]. Finally, complete determination of the output state of a quantum simulation is not efficiently possible, as quantum state tomography (QST) re-

²Or sometimes the Lie-Trotter, Trotter-Suzuki, or Lie-Trotter-Suzuki approximation.

³Roughly, this notation means “at least on the order of, in the asymptotic limit.”

quires an exponential number of measurements (see section 2.1.6); it is for this reason that the simulation must be devised such that properties of interest are determinable with fewer measurements.

Notably, some authors have employed the terminology of quantum simulation versus quantum emulation to distinguish between what has here been termed digital versus analog quantum simulation. In particular, the term emulation is used in Ref. [10] which has been reproduced as Ch. 6; the term emulation is therefore used in that chapter.

4.1.3 Previous work

There exist several ample reviews of the theory, implementations, and progress in quantum simulation. The most general, by Georgescu, Ashhab, and Nori [3] makes use of several worked examples drawn from theoretical and experimental papers to illustrate the concepts, achievements and difficulties in various aspects of quantum simulation. Hauke *et. al.* focus on the reliability, scalability, and efficiency of quantum simulation, especially on questions of the degree to which different types of simulators (analog, digital, open-system, etc.) are likely to prove more efficient than classical techniques in the presence of noise and experimental imperfections [5]; they especially emphasize remaining open questions and areas for further research. Aspuru-Guzik and Walther [11] review quantum simulation with photonic technologies, as does Longhi [12] with a particular focus on simulations of quantum phenomena using coherent light in engineered waveguide structures with non-constant couplings. Prominent examples of proof-of-principle Qs using photons include an analog simulation of fractional anyon statistics [13], a digital simulation to calculate energy spectra of molecular hydrogen [2], and analog simulation of a small frustrated spin tetramer [14].

Notably, much attention has recently been devoted to the assertion by Aaronson and Arkhipov [15] that it is not possible to efficiently classically simulate sampling from the output distribution of many interacting bosons in a linear optical network. If correct, and if the sampling remains difficult to simulate classically even if experimentally unavoidable noise is taken into account, such a so-called BOSONSAMPLING machine has a good chance at the first demonstration of a quantum information protocol that is demonstrably faster on a quantum machine than a classical one. This is because BOSONSAMPLING should be much easier to implement than a quantum simulation or quantum computational algorithm of sufficient size to be classically unmanageable. A BOSONSAMPLING implementation consisting of only tens of bosons has been conjectured to be large enough. Though it is not really an example of one quantum system being used to simulate another, but rather of a quantum system that

is straightforward to implement but classically difficult to simulate, several authors *e.g.* [3] have referred to `BOSONSAMPLING` implementations in the context of quantum simulation. Several proof-of principle demonstrations of `BOSONSAMPLING` have been implemented using photons [16–19].

4.2 Quantum walks: a resource for quantum simulations

Classical random walks (RWs) have been utilized extensively in development of computing algorithms as well as for modeling phenomena ranging from molecular diffusion to stock prices. As the simplest example of a RW, imagine standing at zero on the infinite number line and deciding randomly by flipping a coin whether to move one whole number in the positive or negative direction, then repeating this n times. The probability distribution for your resulting position after n steps will be given by a binomial distribution centered around zero, which approaches a normal or Gaussian distribution as n becomes large.⁴

More formally, a RW describes a Markovian process on an undirected graph G with vertices $\{V(G)\}$ and edges $\{E(G)\}$ which specify the connections between vertices. Walker(s) move randomly between connected vertices. In a discrete-time random walk (DTRW) a walker moves from a given vertex to a randomly-chosen adjacent one at each time step. In continuous-time random walks (CTRWs), walkers move along edges at a constant rate γ ; in other words the probability that a walker moves to an adjacent vertex in an infinitesimal time dt is γdt . Specifying G as well as initial position(s) of walker(s) allows the calculation of the probability distribution $P(V, N)$ [$P(V, T)$] of finding each vertex V occupied after N steps [total time T] in the discrete [continuous] case. From there other quantities of interest can be calculated, such as the rate of spreading—usually specified by $\sigma(V, N)$ or $\sigma(V, T)$, the standard deviation of position as a function of steps or time. Other calculable results include the time required to reach a (near-)uniform distribution, or the expected time until the occupancy of a given vertex is high relative to some threshold [20, 21].

Quantum analogs exist for both the discrete- and continuous-time RW; however the resulting dynamics and output probability distributions are often very different due to the quantum phenomena of superposition and interference. The theory of quantum walks is reviewed in

⁴Noting of course that after an odd number of steps all even integers will have zero occupation probability and vice-versa.

an introductory but thorough fashion by Kempe [20] and in more detail with a focus on the effects of decoherence by Kendon [21].

In quantum walks (QWs), the walker(s) are now quantum particles and their position-state must be specified by a wavefunction:

$$|\psi_{\text{pos}}(t)\rangle = \sum_v c_v(t)|v\rangle, \quad (4.2)$$

where $\{|v\rangle\}$ are orthonormal position eigenstates corresponding to the vertices in $V(G)$, where $\sum_v |c_v|^2 = 1$ and $\langle v|w\rangle = \delta_{vw}$. Note that the walker is in a coherent superposition of vertex positions; indeed instead of evolving via hopping at random between vertices, a quantum walker at a given vertex evolves via moving to all neighboring vertices *in superposition*. This eventually leads to interference between different Feynman paths taken by the walker(s) and it is this interference that is responsible for the sometimes vast differences between the output probability distributions of quantum and (classical) random walks.

Notably, unlike a classical RW, the evolution of a QW is unitary and thus deterministic; randomness is only present once the walker(s) is measured in which case the probabilities that it can be found at the various vertices will be determined from the wavefunction in accordance with the Born rule. We will briefly discuss discrete quantum walks as many readers may be more familiar with them before moving on to explain the continuous case and its connections to the simulation of coherent transport phenomena.

4.2.1 Discrete-time quantum walks

None of the experiments in this thesis concern discrete-time quantum walks (DTQWs), but it will nonetheless be useful to describe them briefly both for completeness and to contrast with the continuous-time case. Further general introduction to DTQWs can be found in [20–22], and a good reference for optical implementations is [23].

In DTQWs, the total Hilbert space of each walker includes not just its position state specified by a wavefunction as in Eq. (4.2), but also a separate space of states which determine the direction the walker will take from each vertex. This state is encoded in a separate, internal degree of freedom of the walker, and is often termed the ‘coin’ state in analogy with the classical one-dimensional case where a walker on a line might be said to ‘flip a coin’ at each time step and travel left or right depending on the outcome. In the simplest case of DTQW,

also on a line, the coin state would be a qubit $|\psi_{\text{coin}}\rangle = \alpha|0\rangle + \beta|1\rangle$ (see section 2.1.1.2). The total state is $|\Psi\rangle = |\psi_{\text{pos}}\rangle \otimes |\psi_{\text{coin}}\rangle$.

The spatial evolution of a discrete quantum walker is governed by a unitary shift operator S which couples the coin degree of freedom to the lattice positions. For example, in the case of DTQW on a line S would act such that $S|v, 0\rangle \rightarrow |v - 1, 0\rangle$ and $S|v, 1\rangle \rightarrow |v + 1, 1\rangle$. In total a single step of a DTQW is then composed of two operations: the shift operator S and a coin operator C which can be any unitary acting only on the coin space. In the one-dimensional linear case a common choice for the coin operator is the Hadamard (Eq. (2.9)), which—like a classical unbiased coin—gives a walker in a position eigenstate an equal probability of moving left or right during the subsequent time step.

In a DTQW the final probability distribution for the walker depends heavily on the initial coin state as well as the initial position. This is in opposition to the classical DTRW where, for example, any unbiased coin will always lead to a symmetric output distribution; in the quantum case even unbiased coin operators such as the Hadamard—where unbiased means that C takes any basis state for the coin subspace to an equally-weighted superposition of all coin basis states—can lead to asymmetric output distributions depending on $|\psi_{\text{coin}}(t = 0)\rangle$. Finally note that in the most general case C may depend on the time step or lattice position; this is called an *inhomogeneous* DTQW [24].

4.2.2 Continuous-time quantum walks

Continuous-time quantum walks (CTQWs) require no separate ‘coin’ subspace; rather the walk occurs entirely in graph-position space and a walker at vertex $|v\rangle$ is continuously coupled to all connected vertices on the graph. Such walks were first studied by E. Farhi and S. Gutman [25]. More specifically, in a CTQW the walker’s position state as given in equation (4.2) evolves according to the Schrödinger equation

$$i\frac{dc_v(t)}{dt} = \sum_w \mathcal{H}_{vw}c_w(t). \quad (4.3)$$

The entries $\mathcal{H}_{vw} = \langle v|\mathcal{H}|w\rangle$ are given by

$$\mathcal{H}_{vw} = \mathcal{H}_{wv} = \begin{cases} -\gamma_{v,w} & \text{if } e_{vw} \in E(G) \\ d_v\gamma_{v,w} & \text{if } v = w \\ 0 & \text{otherwise} \end{cases}, \quad (4.4)$$

where e_{vw} denotes an edge connecting vertices v and w , and d_v is the *degree* of vertex v , giving the number of other vertices to which it is connected. Note that in many treatments of CTQW it is assumed that $\gamma_{v,w} = \gamma \forall \{v,w\}$, *i.e.* that the hopping rate per edge is independent of the edge in question [21], but it is certainly possible to consider cases where these rates are different and in fact this would be necessary to describe many common experimental implementations of CTQWs where non-nearest-neighbor coupling may be unavoidable.

Both the discrete and continuous cases of QWs can also, as hinted previously, be generalized to include the presence of multiple walkers. Whereas in the classical case, the total output probability distribution from multiple walkers is simply the sum of the individual distributions, in the quantum case the interaction of the walks must be treated coherently, meaning that it is the complex probability amplitudes for different outcomes which must be summed, prior to taking absolute squares in order to find probabilities. If the walkers are at least partially indistinguishable, this leads to quantum interference, in particular a generalized form of Hong-Ou-Mandel (HOM) interference [26] wherein the walkers display bunching and/or anti-bunching behavior. Further details concerning methods for predicting the nonclassical interference effects between multiple photons in quantum walks can be found in appendix 6.6.

4.2.3 Applications of quantum walks

In addition to their intrinsic interest, several practical motivations exist for studying CTQWs. The first concerns their utility for quantum computation: A. Childs *et al.* [27] and N. Lovett *et al.* [28] respectively showed that single-walker discrete- and continuous-time QWs were universal for QC; however such scalable QC using single walkers would be computationally inefficient. A more exciting prospect is provided by the recent demonstration by Childs *et al.* that walks of multiple, coherently-interacting quantum walkers CTQWs are both universal and efficient for quantum computation [29]. The study of CTQWs has also inspired the development of several quantum algorithms [21].

CTQWs have additionally formed a useful framework for several types and implementations of coherent simulations of quantum effects, as well as for fully-quantum simulations—both proposed and actualized. As thoroughly reviewed by S. Longhi [12], continuous walks with time-dependent Hamiltonians have in particular allowed the simulation of physically interesting quantum effects including the quantum Zeno effect [30], the trembling motion of a relativistic free electron known as Zitterbewegung [31], Klein tunnelling [32], and Anderson

localisation [33]; notably the optical implementation of the time-dependent *discrete* case has also yielded an optical simulation of topological phases [34].

4.2.4 CTQWs: Models for coherent transport phenomena

Another interesting application of CTQWs is as models for transport on complex networks. Many physical processes of interest involve transport of *e. g.* charge or energy in structures that can be modeled as networks of discrete sites. O. Mülken and A. Blumen review models of energy transport between coupled sites as CTQW and CTRW, which “act as the two cases of purely coherent and purely incoherent transport, respectively” [35]. They focus particularly on the efficiency of transport processes in different systems, and the ways in which these will be affected by the level of coherence of the transport. In particular, there has been much interest in the past three to five years in the use of CTQWs, especially with the addition of decoherence, as models for energy transport in biological photosynthetic complexes. In these systems, absorption of solar radiation excites chromophores such as chlorophylls from the ground state to the first excited state⁵. The resulting molecular excitations are called excitons and act as quasiparticles which can couple between networks of chromophores held in position in the light-harvesting complex (LHC) by a protein matrix. Eventually the excitons can be trapped by some particular chromophore or subset of chromophores, which then feed the exciton to Reaction Centers (RCs), where they are transferred into chemical energy and subsequently into sugars. Fluorescence studies in LHCs of some photosynthetic bacteria have found evidence for coherence in exciton transport along chromophore networks [37].

Tight-binding models are used to describe quantum systems consisting of many weakly-coupled sites wherein the set of all the eigenfunctions for each individual site forms an approximate basis for the whole system. Such models are used in solid-state physics, with individual atoms as the sites, for calculating electronic band structures [38], and can also be applied to many transport phenomena including excitons in chromophoric networks as well as charges in molecular crystals and quantum dots [39, 40]. For a single quantum excitation in a network of N coupled lattice sites, the tight-binding Hamiltonian is given by:

$$H = \sum_{m=1}^N \varepsilon_m |m\rangle\langle m| + \sum_{n<m}^N V_{mn} (|m\rangle\langle n| + |n\rangle\langle m|). \quad (4.5)$$

Here the sites are labeled $m \in \{1, N\}$ with the kets $|m\rangle$ representing localization of the excitation at one such site, the individual site energies are ε_m , and V_{mn} gives the coupling

⁵Under biological conditions the remaining excited states are rarely excited and can be neglected [36].

rate between two such sites. This Hamiltonian is notably of the same form as that given for CTQWs above in Eq. (4.4), with the couplings V corresponding to the hopping rates $-\gamma$.

However, the Hamiltonian as written here in Eq. (4.5) represents a further generalization of a CTQW wherein the site energies V can take on differing values; this is known as static disorder. Notably in chromophoric systems, where each chromophore constitutes a site, this can occur even with near-identical chromophores due to their differing local environments within the cell. Such random static disorder often decreases diffusion as first noticed by P. Anderson [41]; this phenomenon is therefore known as Anderson localization. Coupling and therefore diffusion and eventual transport to the RCs can also be suppressed by the well-known quantum Zeno effect, wherein a noisy environment—in this case the relatively wet and warm biological cell—effectively induces repeated measurements in quick succession and thereby inhibits the free evolution of the system according to the Schrödinger equation.

The effects of such noisy environments on quantum transport and CTQWs can be modeled using the Lindblad quantum master equation formalism presented in Sec. 2.1.5.1; see *e.g.* Ref. [21, 42–44].

Interestingly, exciton transport in some studied systems, particularly the Fenna-Matthews-Olson complex (FMO), appears to be both highly *efficient*—meaning the exciton has a high probability to be absorbed at the reaction center instead of lost through relaxation or environmental interactions—and also relatively fast. This is despite the wet, warm environment and associated loss and localization mechanisms such as the Zeno effect, and also despite disorder in the lattice leading to Anderson localization. In fact it has recently been repeatedly theorized that the interplay between these two mechanisms which, individually, generally limit transport—Anderson localization and the quantum Zeno effect—may in fact increase transport efficiency. This phenomenon, known as environmentally-assisted quantum transport (ENAQT) [42] or dephasing-assisted energy transport [43, 44], is described further and explored experimentally in Ch. 7.

References

- [1] Feynman, R. Simulating physics with computers. *Int. J. Theor. Phys.* **21**, 467–488 (1982). [43](#)
- [2] Lanyon, B. P. *et al.* Towards quantum chemistry on a quantum computer. *Nature Chem.* **2**, 106–111 (2010). [44](#), [47](#)
- [3] Georgescu, I. M., Ashhab, S. & Nori, F. Quantum simulation. *Rev. Mod. Phys.* **86**, 153–185 (2014). [44](#), [45](#), [47](#), [48](#)
- [4] Lloyd, S. Universal quantum simulators. *Science* **273**, 1073–1078 (1996). [44](#)
- [5] Hauke, P., Cucchietti, F. M., Tagliacozzo, L., Deutsch, I. & Lewenstein, M. Can one trust quantum simulators? *Rep. Prog. Phys.* **75**, 082401 (2012). [45](#), [46](#), [47](#)
- [6] Cirac, J. I. & Zoller, P. Goals and opportunities in quantum simulation. *Nature Phys.* **8**, 264–266 (2012). [45](#), [46](#)
- [7] Buluta, I. & Nori, F. Quantum simulators. *Science* **326**, 108–111 (2009). [45](#), [46](#)
- [8] Nielsen, M. & Chuang, I. *Quantum Computation and Quantum Information Theory* (Cambridge Univ. Press, Cambridge, 2000). [46](#)
- [9] Ward, N. J., Kassal, I. & Aspuru-Guzik, A. Preparation of many-body states for quantum simulation. *J. Chem. Phys.* **130**, – (2009). [46](#)
- [10] Owens, J. O. *et al.* Two-photon quantum walks in an elliptical direct-write waveguide array. *New J. Phys.* **13**, 075003 (2011). [47](#)
- [11] Aspuru-Guzik, A. & Walther, P. Photonic quantum simulators. *Nature Phys.* **8**, 285–291 (2012). [47](#)
- [12] Longhi, S. Quantum-optical analogies using photonic structures. *Laser Photon. Rev.* **3**, 243–261 (2009). [47](#), [51](#)
- [13] Lu, C.-Y. *et al.* Demonstrating anyonic fractional statistics with a six-qubit quantum simulator. *Phys. Rev. Lett.* **102**, 030502 (2009). [47](#)
- [14] Ma, X.-S., Daki, B., Naylor, W., Zeilinger, A. & Walther, P. Quantum simulation of the wavefunction to probe frustrated heisenberg spin systems. *Nature Phys.* **7**, 399 – 405 (2011). [47](#)

- [15] Aaronson, S. & Arkhipov, A. The computational complexity of linear optics. In *Proceedings of the Forty-third Annual ACM Symposium on Theory of Computing*, STOC '11, 333–342 (ACM, New York, NY, USA, 2011). 47
- [16] Broome, M. A. *et al.* Photonic boson sampling in a tunable circuit. *Science* **339**, 794–798 (2013). 48
- [17] Crespi, A. *et al.* Integrated multimode interferometers with arbitrary designs for photonic boson sampling. *Nature Photon.* **7**, 545–549 (2013). 48
- [18] Spring, J. B. *et al.* Boson sampling on a photonic chip. *Science* **339**, 798–801 (2013). 48
- [19] Tillmann, M. *et al.* Experimental boson sampling **7**, 540–544 (2013). 48
- [20] Kempe, J. Quantum random walks: An introductory overview. *Contemp. Phys.* **44**, 307–327 (2003). 48, 49
- [21] Kendon, V. Decoherence in quantum walks: a review. *Math. Structures Comput. Sci.* **17**, 1169–1220 (2007). 48, 49, 51, 53
- [22] Owens, J. O. *A continuous-time quantum walk of single photons in integrated optics*. Honours thesis, University of Queensland (2010). 49
- [23] Broome, M. A. Photonic quantum information and quantum walks (2012). 49
- [24] Linden, N. & Sharam, J. Inhomogeneous quantum walks. *Phys. Rev. A* **80**, 052327 (2009). 50
- [25] Farhi, E. & Gutmann, S. Quantum computation and decision trees. *Phys. Rev. A* **58**, 915–928 (1998). 50
- [26] Hong, C. K., Ou, Z. Y. & Mandel, L. Measurement of subpicosecond time intervals between two photons by interference. *Phys. Rev. Lett.* **59**, 2044–2046 (1987). 51
- [27] Childs, A. M. Universal computation by quantum walk. *Phys. Rev. Lett.* **102**, 180501 (2009). 51
- [28] Lovett, N. B., Cooper, S., Everitt, M., Trevers, M. & Kendon, V. Universal quantum computation using the discrete-time quantum walk. *Phys. Rev. A* **81**, 042330 (2010). 51
- [29] Childs, A. M., Gosset, D. & Webb, Z. Universal computation by multiparticle quantum walk. *Science* **339**, 791–794 (2013). <http://www.sciencemag.org/content/339/6121/791.full.pdf>. 51

- [30] Biagioni, P. *et al.* Experimental demonstration of the optical Zeno effect by scanning tunneling optical microscopy. *Opt. Express* **16**, 3762–3767 (2008). 51
- [31] Dreisow, F. *et al.* Classical simulation of relativistic Zitterbewegung in photonic lattices. *Phys. Rev. Lett.* **105**, 143902 (2010). 51
- [32] Dreisow, F. *et al.* Klein tunneling of light in waveguide superlattices. *Europhysics Letters* **97**, 10008 (2012). 51
- [33] Naether, U. *et al.* Anderson localization in a periodic photonic lattice with a disordered boundary. *Opt. Lett.* **37**, 485–487 (2012). 52
- [34] Kitagawa, T. *et al.* Observation of topologically protected bound states in photonic quantum walks. *Nat. Commun.* **3** (2012). 52
- [35] Mülken, O. & Blumen, A. Continuous-time quantum walks: Models for coherent transport on complex networks. *Phys. Rep.* **502**, 37–87 (2011). 52
- [36] Kassal, I. *Quantum Computation for Chemical Problems*. Ph.D. thesis, Harvard University (2010). 52
- [37] Panitchayangkoon, G. *et al.* Long-lived quantum coherence in photosynthetic complexes at physiological temperature. *Proc. Natl. Acad. Sci. U.S.A.* **107**, 12766–12770 (2010). 52
- [38] Ashcroft, N. W. & Mermin, D. N. *Solid State Physics* (Thomson Learning, Toronto, 1976), 1 edn. 52
- [39] Cho, M., Vaswani, H. M., Brixner, T., Stenger, J. & Fleming, G. R. Exciton analysis in 2D electronic spectroscopy. *J. Phys. Chem. B* **109**, 10542 (2005). 52
- [40] Nazir, A., Lovett, B. W., Barrett, S. D., Reina, J. H. & Briggs, G. A. D. Anticrossings in Förster coupled quantum dots. *Phys. Rev. B* **71**, 045334 (2005). 52
- [41] Anderson, P. W. Local moments and localized states. *Rev. Mod. Phys.* **50**, 191 (1978). 53
- [42] Reberntrost, P., Mohseni, M., Kassal, I., Lloyd, S. & Aspuru-Guzik, A. Environment-assisted quantum transport. *New J. Phys* **11**, 033003 (2009). 53
- [43] Plenio, M. B. & Huelga, S. F. Dephasing-assisted transport: quantum networks and biomolecules. *New J. Phys* **10**, 113019 (2008). 53

- [44] Chin, A., Datta, A., Caruso, F., Huelga, S. & Plenio, M. Noise-assisted energy transfer in quantum networks and light-harvesting complexes. *New J. Phys.* **12**, 065002 (2010).

53

Chapter 5

Coupled waveguide arrays, and their use in simulating quantum walks and biological Hamiltonians

5.1 Introduction

There has been recent rapid progress in the field of integrated quantum photonics: the first integrated entangling quantum gate was demonstrated in 2008 [1] and there have since been demonstrations of quantum algorithms [2], reconfigurable integrated quantum circuits, integrated photon sources, and integrated detectors [3–6]. Progress has been particularly fast in laser-written waveguides, where femtosecond lasers are used to directly and accurately write arrays of waveguides into dielectric substrates. Evanescent coupling between pairs of waveguides in an array can be used to create arbitrary beamsplitters, as well as multi-mode splitters and interferometric networks. Systems of coupled waveguides can also be used for implementing continuous-time quantum walks (CTQWs), and thereby for quantum simulations.

Unlike arrays of waveguides produced through conventional lithographic methods, laser-written arrays can be fully three-dimensional. This greatly expands the possible applications for coupled waveguide arrays, for instance by significantly simplifying waveguide crossovers in order to mix initially non-adjacent modes in an interferometric network; by enabling quantum walks (QWs) with periodic boundary conditions where the first and final graph vertices are coupled through *e.g.* a circular geometry; and by allowing QWs on multiply-connected graphs where some vertices have more than two adjacent edges. These capabilities render the femtosecond laser direct-write (FLDW) technique particularly well-suited for some applications

in photonic quantum information processing (QIP), in particular the simulation of non-trivial Hamiltonians.

In Sec 5.2 of this chapter we describe the fabrication of FLDW waveguide arrays, with a particular focus on those features and difficulties which are most relevant to experimental quantum simulators (Qs). We also describe how such arrays can be used to generate interferometric networks, which can in turn be employed for photonic QIP. In section 5.3, we illustrate how laser-written waveguide arrays can be employed for analog quantum simulations, using as a working example a proposal for simulating the Hamiltonian which governs exciton dynamics in the B850 subunit of the light-harvesting complex (LHC) II of the *Rhodobacter sphaeroides* purple photosynthetic bacteria. We detail experimental considerations and difficulties which arose when designing and implementing a practical simulation of this Hamiltonian, and present the theoretical and experimental results of these efforts. Finally we discuss prospects and considerations for improved implementations of this simulation in FLDW waveguide arrays in the future.

5.2 Laser-written waveguide arrays

The direct-write technique for creating waveguide arrays uses a pulsed femtosecond laser to produce local modifications to the optical properties and refractive index of a dielectric material. The writing beam is typically from a strong Titanium:Sapphire laser, and the material is typically a transparent glass which has no linear absorption at the wavelength of the writing laser, but in which nonlinear processes can lead to localized structural changes where the laser illumination is sufficiently intense, such as at the focus. By translating the sample through the focus, regions of modified refractive index can be directly written into the substrate. These can form a high-index guiding core which is surrounded by the lower-index unmodified substrate and can act as a waveguide, supporting one or more bound transverse spatial modes. This process is illustrated schematically in Fig. 5.1.

Before discussing laser-written waveguides in further detail we should note that many applications of integrated photonics to quantum information and simulation have taken place in lithographic rather than laser-written waveguide technologies. Silica-on-silicon circuits were used in 2008 to demonstrate the first integrated two-qubit photonic entangling quantum gate [1], and silica-on-insulator circuits have been used for demonstrations including Shor's factoring algorithm [2], one-dimensional quantum walks of correlated photons [7], generation and measurement of entanglement using a reconfigurable circuit [4, 5], and quantum interference between photons generated on-chip [8]. Lithium niobate circuits have also been used to

demonstrate on-chip photon pair generation and fast active switching [9–11], as has lithium tantalate [12], and superconducting photon detectors have been integrated into both lithium niobate and gallium arsenide photonic circuits [6, 13, 14].

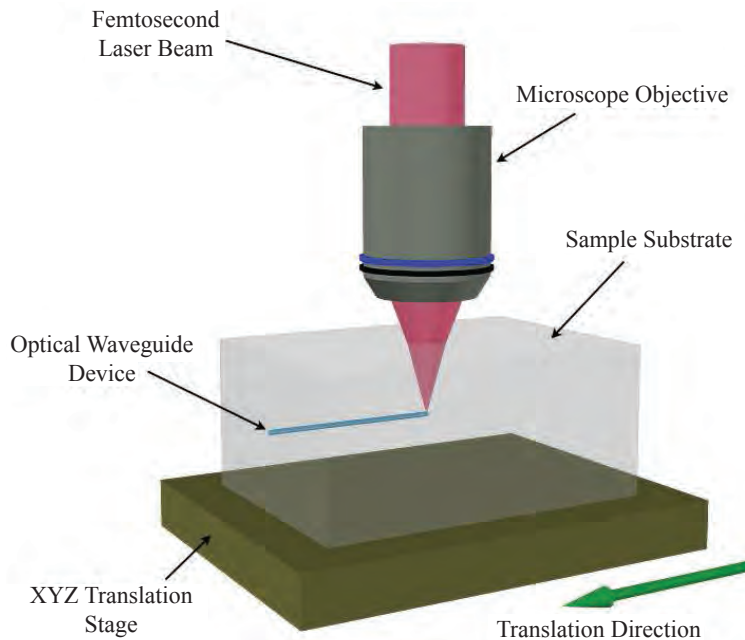


Figure 5.1: An illustration of a typical process for creating femtosecond laser-written waveguide arrays. The pulsed laser beam is tightly focused with a microscope objective into the sample, which can then be precisely translated in three dimensions to produce waveguides. This figure is reproduced from Ref. [15].

5.2.1 Material modification mechanisms

A general description of the interactions between the laser and the substrate which yield index change involves several interacting mechanisms. We will summarize them here but direct the reader to Refs. [15–17] and references therein for further details.

When a focused laser pulse strikes the glass substrate, atoms in the glass can initially become ionized due to two different processes: multi-photon ionization, where the combined energy of multiple simultaneously-absorbed incident photons is enough to promote an electron from the valence to the conduction band, and tunneling ionization, where the strong electric field at the laser focus reduces the Coulombic bandgap thereby allowing some electrons to tunnel into the conduction band. The interaction of the laser field with these free electrons can in turn result in further avalanche ionization, wherein ionized electrons transfer energy absorbed from the laser field to other bound electrons through collisions. These processes

result in an exponentially-increasing avalanche of ionization during the duration of the laser pulse [17], which is generally on the order of 100 fs. Changes in incident pulse duration result in shorter or longer periods of interaction between the laser field and this free electron plasma, and can therefore yield differing results for the net index modification.

The resulting plasma of electrons and ions is initially confined to the focal volume of the laser. As the electrons recombine with the ions in the lattice, which generally occurs on a picosecond time scale [17], index changes can occur through some combination of three different mechanisms: formation of color centers, photo-induced chemical-bond restructuring, and thermally-induced density modification [17]. The former, consisting of defects in the atomic lattice, are not currently understood to be a major contributor to any resulting index change, as evidenced by the fact that such changes persist even after thermal annealing which should remove the color centers [18]. Thermally-induced densification occurs because the final density of melted and cooled glasses depends on both the peak temperature reached and the rate of cooling. If the time between writing laser pulses is long compared to the timescale of thermal diffusion in the glass—generally on the order of microseconds [17]—then only the glass within the focal volume will melt and it will cool quickly. In this case, the structural changes in the glass are essentially caused by each pulse in isolation [16]. However, for higher repetition rates where the glass does not cool completely between pulses, heat can accumulate in the focal region and diffuse into the surrounding material, leading to a larger melt volume. This is known as the cumulative heating regime and is generally reached for repetition rates higher than 1 MHz.

The details of these effects as well as their interactions and the degree to which each contributes to index changes in the glass will be influenced by many factors: the type of glass (*i.e.* pure fused silica vs. borosilicate or crown glass), the pulse duration, repetition rate, polarization, central wavelength, the size and shape of the laser focus, and the translation speed of the substrate through the focus. In this chapter we refer to a particular set of all such factors, used for creating waveguides in a manner which is made as repeatable as possible, as a waveguide *reci-pe*. In general the resulting net structural changes come in three qualitatively different varieties and correspond to three different pulse energy regimes, all else being constant [16]:

1. Voids can be created in the glass when the material in the volume rapidly becomes highly excited and vaporized and expands into the surrounding material in a so-called microexplosion; this leaves a core of zero or decreased density surrounded by a higher-density shell, and only occurs at high pulse energies.

2. Intermediate pulse energies result in the formation of *nanogratings* in the focal volume with alternating nanometer-scale stripes of high- and low-density oriented perpendicular to the polarization of the writing laser [19]. The exact formation mechanism is unclear. However, these sub-wavelength-scale structures yield both index change and significant birefringence.
3. At pulse energies which are lower, yet still above the threshold for glass modification, smoothly-varying and isotropic index changes result. These are thought to be mostly a result of the heating, melting, and rapid cooling of the glass the focal volume, and—if the writing conditions are in the cumulative heating regime—in the surrounding volume as well.

As an example, in fused silica with 100 fs laser pulses at 800nm and focused with a numerical aperture (NA) of 0.65, smooth isotropic index changes will result from pulse energies in the range 40 to 150 nJ, pulse energies between 150 and 500 nJ will result in birefringent nanogratings, and energies above 500 nJ will yield void formation [16].

For the creation of isotropic, single- or few-mode waveguides with minimal birefringence, operation in the regime of smoothly-varying, isotropic index change is desired. Given a recipe suitable for smooth index modification, translating the sample in the z -direction results in a waveguide with an approximately constant index profile $n(x, y)$.

The ability to produce complicated three-dimensional waveguide structures, one of the principal advantages of the laser-written waveguide approach, stems from the possibility of also translating the sample slowly in x and y .

5.2.2 Waveguide modes, coupling, phase shifts, and circuits

Given a structure which is weakly-guiding in the z -direction¹ and slowly varying in the x - and y -directions, the scalar and paraxial approximations can be applied to Maxwell's equations. For monochromatic light of vacuum wavelength λ , the propagation within the structure is

¹The weak guiding approximation is essentially that $\max(V(x, y)) \ll 1$, where $V(x, y)$ is the index 'potential' defined previously.

then described by the slowly-varying electric field amplitude ψ which obeys the equation²

$$\frac{i}{k} \frac{\partial \psi}{\partial z} = -\frac{1}{2k^2 n_0} \left(\frac{\partial^2}{\partial x^2} + \frac{\partial^2}{\partial x y} \right) \psi + V(x, y) \psi, \quad (5.1)$$

where $k = 2\pi/\lambda$ is the vacuum wavenumber, n_0 is the index of the unmodified substrate which acts as the waveguide ‘cladding’, and $V(x, y) = [n_0^2 - n^2(x, y)]/(2n_0)$. We use this terminology because Eq. (5.1) can be viewed as an analogue of the Schrödinger equation, where $1/k$ takes the role of \hbar and $V(x, y)$ that of the potential. We will return to this analogy in Sec. 5.3.

The number of transverse spatial guided modes supported by the waveguide, as well as the transverse spatial profile $\psi(x, y)$ of those modes, will be determined by the index potential $V(x, y)$. Several other parameters can also be defined which characterize the bound modes. The most important of these is the propagation constant β , which gives the effective wavenumber, $\beta = 2\pi n_{\text{eff}}/\lambda$, where n_{eff} is the effective index experienced by the mode. The profile $\psi(x, y)$ and propagation constant β can not in general be calculated analytically. Many scholarly works are, however, devoted to the calculation or approximation of these properties and we will not rehash this waveguide theory in detail here, but instead refer the reader to Refs. [15, 21, 22] and references therein. For the experiments in this thesis we are exclusively concerned with single-mode waveguides, which support only one transverse spatial mode at the operating wavelength. Note that in general the term single-mode waveguide refers only to the transverse spatial mode; such waveguides will support a range of frequency modes and will generally support two orthogonal polarization modes as well.

Outside the waveguide core where the index has been modified, the amplitude profiles of bound modes have evanescent tails which asymptote towards zero. The precise shape of the amplitude in these tails as a function of position relative the waveguide core will depend on the shape of the index potential. For instance, in the (unphysical) case of a single-mode waveguide where $V(x, y)$ is infinitely parabolic, the bound mode profile will be Gaussian, and when $V(x, y)$ has a circular step function or ‘top hat’ profile, the mode profile outside the core will be a zeroth-order modified Bessel function of the second kind [21]. If two single-mode waveguides are sufficiently close together, the modes of the individual waveguides will not be eigenmodes of the resulting double-well potential. The waveguides will then be able to exchange power through the overlapping portion of their evanescent tails. In the regime where the coupling is weak³, the coupling constant—which determines the rate of power

² Note that if the x - and y -coordinates of the center of the waveguide vary in z , a correction must be applied to this equation which amounts to a gauge transformation from the laboratory reference frame into the waveguide reference frame. This has interesting effects, in particular for multimode waveguides with significant curvature, but is not relevant here. Details can be found in Ref. [20].

³The weak coupling approximation is $C \ll \beta$ where C is the coupling constant and β the propagation

transfer—will be proportional to the overlap between the individual waveguide modes. The coupling will thus decrease with waveguide separation. The weak coupling approximation applies as long as the total system eigenmodes can be well-approximated as superpositions of the individual waveguide modes, and the theory which describes the resulting coupling is analogous to the tight-binding model in solid-state theory.

Given those approximations, we can describe a general array of N coupled waveguides using the Heisenberg picture: we associate a creation operator $a_k^\dagger(z)$ to each waveguide which creates a photon in waveguide $k \in N$ at position z , and only the creation operators and not the mode shapes vary during propagation. The photon occupation of the waveguides is then governed by the equation

$$i \frac{\partial}{\partial z} a_k^\dagger(z) = \beta_k(z) a_k^\dagger(z) + \sum_{j \neq k}^N C_{jk}(z) a_j^\dagger(z), \quad (5.2)$$

where β_k and C_{jk} represent coupling and propagation constants respectively.

Integrated waveguide ‘beamsplitters’ with variable reflectivity can be created by changing the transverse separation of two waveguides, both propagating in the z -direction, so that they couple for some length before separating. These are called directional couplers, and an example is shown in Fig. 5.2. The effective splitting ratio can be controlled by changing the separation distance and angle as well as the coupling length. Such directional couplers are described in further detail in Ch. 8. They can then be concatenated to form interferometric networks for quantum circuits, as in Ch. 8 where they are employed to create an integrated photonic quantum gate. The use of laser-written directional couplers for photonic quantum circuits was first reported in Ref. [23], where they were shown to support quite high-visibility two photon quantum interference, suggesting highly-indistinguishable spatial modes between waveguides.

Accurate control of the optical phase difference between modes in laser-written waveguide circuits is difficult to achieve by merely changing relative optical path length, as this requires control of relative waveguide length on the order of 100 picometers. However, accurate *active* phase control has been demonstrated using surface thermo-optic phase shifts [3]. More recently passive control over relative phase in FLDW circuits has been achieved using slight changes in the curvature of the S-shaped bend regions—which can be seen in Fig. 5.2—in directional couplers [25], as well as by detuning the effective propagation constant in one arm of a directional coupler using temporary coupling to a tertiary waveguide with full constant.

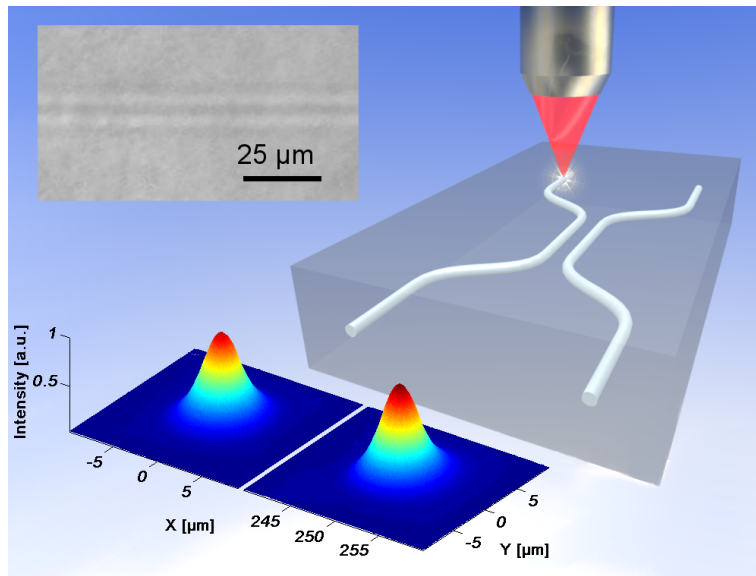


Figure 5.2: An illustrative schematic of a 50/50 laser-written directional coupler reproduced from Ref. [24]. The upper-left inset shows a microscope image of the two parallel waveguides in the interaction region, while the bottom inset shows the output mode intensity profiles.

power return into the coupler waveguide [26]. In Ch. 8, we demonstrate another method to achieve a relative phase shift which exploits the oscillatory nature of the power exchange between the waveguides in a directional coupler. The ability to create arbitrary-reflectivity beamsplitters—directional couplers—combined with phase shifts, and recently developed control over polarization-dependence of couplers and over ‘waveplate’ operations as described in the following section (5.2.3), allows for arbitrary unitary operations on path- and polarization-encoded photonic qubits in FLDW circuits [27].

5.2.3 Practical fabrication considerations: waveguide profile and polarization dependence

Particular mode characteristics are often desirable in a waveguide array for a specific application. In addition to assuring that the waveguides are single-mode at the desired operation wavelength, one may for instance wish to maximise the overlap between the waveguide mode and the mode of commercial single-mode fiber in order to minimize coupling loss. It may also be desirable to precisely engineer $C_{jk}(\Delta x, \Delta y)$, the coupling constant between two waveguides in the array separated by distances $\Delta x = x_k - x_j$ and $\Delta y = y_k - y_j$, by changing the shape and size of the index potential V of the waveguides. In particular, for simulation applications a circular index potential may be desirable so that inter-waveguide coupling is isotropic, *i.e.*

depends only on the separation between the waveguide cores and not on the direction of that separation in the (x, y) -plane.

Another fabrication consideration is polarization-dependence, specifically birefringence and polarization-dependence of the inter-waveguide coupling. In addition to being caused by nanograting formation during writing, the former may result from ellipticity of the waveguide mode [28] or from strain in the glass [29]. It is often desirable to reduce the polarization dependent behavior of waveguide array circuits. Birefringence, particularly in combination with polarization-dependent coupling, may result in initially-indistinguishable photons undergoing different rotations in a quantum circuit before interfering. This will result in lower quantum interference visibility. Even without interference to consider, birefringence will cause deviations from desired dynamics if the array Hamiltonian was optimized for one particular polarization.

It has been demonstrated that, under certain writing conditions, the intrinsic birefringence of coupled laser-written waveguides may be sufficiently low to enable their use with polarization-encoded photonic qubits [24]. The intrinsic birefringence has also been exploited, first to produce partially-polarizing couplers which could be combined to form an integrated CNOT gate for polarization-encoded photons [30]. The strain-induced polarization-dependence may be intrinsic, resulting from the thermally-induced density modification during the writing process, or externally-induced; the latter has recently been used for active polarization-dependent phase-shifting by applying pressure over a small area of the glass surface above the waveguides with a piezoelectric actuator [31]. Permanent strain induced by the presence of a laser-written defect near the waveguide has also recently been used to create arbitrary waveplate rotations in laser-written waveguides [32]. Similar waveplate operations have recently been obtained where the birefringence stems from waveguide ellipticity; in this case the birefringent axes are rotated by changing the laser incidence angle [33].

The mode shape, propagation constant, and the birefringence can all—to some extent—be controlled by varying the fabrication recipe, particularly factors such as the glass composition and laser pulse properties. However due to the complexity of the laser-matter interactions as explained in Sec. 5.2.1, it is usually not possible to accurately predict the effect of specific fabrication parameter changes from first principles; rather parameter studies must be performed wherein the effects of changes in a specific fabrication parameter on a particular waveguide characteristic are measured over a range of variations, and interpolation can then be used to home in on the optimal recipe. While this may be time-consuming, the ability to rapidly prototype several circuits with slight recipe variations constitutes a further significant advantage of the FLDW technique over lithographic methods, which usually require the time-consuming

creation of a new photo-resistive mask for each different waveguide array [17].

The most obvious means to affect the index profile $n(x, y)$ —and thereby the shape of the guided mode—are: (i) to change the waveguide writing speed, (ii) to change the laser parameters such as pulse energy and repetition rate, or (iii) to modify the focal shape by changing the objective NA or adding cylindrical lenses or slits. The latter method (iii) has been used to achieve near-isotropic coupling [34], and was employed to produce the waveguides for the CTQW on an ellipse presented in Ch. 6. Another method involves writing each waveguide with multiple passes of the writing laser. This is appropriate with fabrication recipes where only a small index change can be achieved in a single pass without causing undesired cumulative heating or birefringent nanograting formation; multiple passes can then accentuate the index change in the waveguide core without these deleterious effects [15]. This can also yield a more step-like index profile when the focal volume is *e.g.* a three-dimensional gaussian, as later passes will effect less additional modification in the already highly-modified center of the core than at the less-modified edges. This technique was used to create the waveguides in Ch. 6.

Another recently-developed post-processing technique involves thermally annealing the sample after writing the waveguides by heating it to above its annealing point before cooling slowly to below the strain point [29, 35, 36]. This has been shown to result in rounder and more Gaussian index profiles with lower bend losses [35], possibly reduced coupling losses [36], and a reduced birefringence [29]. We hypothesize that the more circular resulting index profile would also yield more isotropic coupling. As an example, pre- and post-annealing microscopy images of laser written waveguides are shown in Fig. 5.3. Unfortunately, our fabrication collaborators had not yet developed this technique during the design and fabrication of the waveguide array circuits described in the subsequent sections of this chapter.

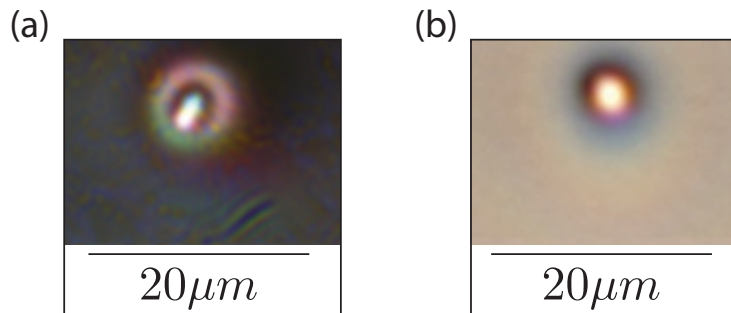


Figure 5.3: (a) Transmission differential interference microscope image of a laser written waveguide which is single mode at 800 nm prior to annealing. (b) Bright field microscope image of a different but similarly-written waveguide after annealing over a 40 hour duration. The latter is single mode at 800 nm after annealing but not before. Figure used with permission from T. Meany [36].

5.3 Quantum simulation in coupled waveguide arrays

It is perhaps not surprising that optics have proven useful for simulating quantum mechanics, as even ‘classical’ optical coherent states exhibit coherent superpositions, interference, and even ‘tunneling’ in the form of evanescent coupling. The analogy between coupled waveguides and the quantum mechanical double-well potential was established by 1974 [37]. Fundamentally the utility of waveguide arrays for simulating quantum systems can be traced to the similarity between the scalar, paraxial optical wave equation, Eq. (5.1), and Schrödinger’s equation: the spatial evolution of the light in the paraxial direction corresponds to the temporal evolution of a quantum system in a binding potential [20, 38]. Several waveguide simulations of quantum phenomena have been briefly described in Sec. 4.1.3 and many more can be found in Ref. [20] and references therein.

We will focus specifically on the behavior of N coupled waveguides in the tight-binding approximation, as described in Eq. (5.2), which has the same form as that describing a continuous-time quantum walk, Eq. (4.3). Waveguide arrays can thus be used to simulate a large class of generalized $N \times N$ quantum walk Hamiltonians of the form

$$\mathcal{H} = \begin{pmatrix} \varepsilon_1 & V_{12} & \dots & V_{1N} \\ V_{21} & \varepsilon_2 & & \\ \vdots & & \ddots & \\ V_{N1} & & & \varepsilon_N \end{pmatrix}. \quad (5.3)$$

This Hamiltonian, a slightly more generalized form of that given previously for CTQWs in

Eq. (4.4), is also recognizable as the tight-binding Hamiltonian from Eq. (4.5), with site energies ε_k , and inter-site couplings V_{jk} . The simulation will be possible provided the waveguides can be fabricated and arranged such that the propagation and coupling constants β_j and C_{jk} sufficiently well approximate the diagonal entries ε_j and off-diagonal entries V_{jk} of the target Hamiltonian, respectively. In fact, in a further generalization, changing the propagation constants and relative (x, y) positions of the waveguides in a manner which is slow relative to the paraxial propagation can be used to simulate time-dependent Hamiltonians.

Of course not all Hamiltonians of the form (5.3) can be simulated in waveguides, but rather only those for which the waveguides can be arranged such that the inter-waveguide coupling constants sufficiently match the off-diagonal entries V_{jk} . In general \mathcal{H} has on the order of N^2 entries whereas the N waveguides have only N positions to adjust. This may make it impossible, for instance, to set coupling between non-nearest neighboring vertices strictly to zero in the simulation of a continuous quantum walk. However, in many systems where quantum transport—as discussed in Sec. 4.2.4—is of interest, the coupling between sites decreases rapidly with increasing distance, just as for evanescently-coupled waveguides. In particular, this is the case for exciton transport between networks of coupled chromophores in biological light-harvesting complexes, where the coupling at large separations is dominated by Coulombic dipole-dipole interactions [38].

This three-way analogy—between an array of coupled waveguides, a continuous-time quantum walk, and the tight-binding Hamiltonian describing quantum transport in a network of coupled lattice sites—underlies the experiments presented in Chs. 6 and 7, and will be further explored in the remainder of this chapter, using as a working example the simulation of the Hamiltonian of a photosynthetic light-harvesting complex (LHC).

5.3.1 Simulating the LH-II B850 subunit in

Rhodobacter sphaeroides: initial theory

Rhodobacter sphaeroides, shown in Fig. 5.4(a), is a photosynthetic purple *proteobacteria* which lives in dark conditions such as deep lakes. It has evolved near-unit efficiency in harvesting photons for photosynthesis and is consequently very well studied [38]. It contains two types of LHCs called LH-I and LH-II as shown in Fig. 5.4(b). The LH-II complex, in return, has two prominent subunits—shown in Fig. 5.4(c)—each consisting of coupled bacteriochlorophylls, respectively called the B800 and B850 subunits due to their light absorbance near 800 and 850 nm, respectively. The B850 subunit consists of a ring of 16 chromophores as shown

in Fig. 5.4(c), which come in 8 pairs of two adjacent, differently-oriented bacteriochlorophylls [38].

In his doctoral thesis Ref. [38], I. Kassal initially suggested that the Hamiltonian governing exciton coupling in the B850 subunit could be simulated using a three-dimensional arrangement of coupled single-mode waveguides, and found an explicit geometrical arrangement for doing so based on waveguide coupling parameters estimated from Ref. [34]. My initial discussion of the theory behind such a simulation follows his.

Because *Rhodobacter sphaeroides* lives in exceedingly low-light conditions it is reasonable to neglect the rare cases when more than one exciton is present in a B850 subunit. The dynamics of the unexcited case are uninteresting; the remaining case with exactly one exciton is called the single-exciton manifold. In biological conditions, states in this manifold will be subject to deherence and loss mechanisms—in fact, a significant motivator for undertaking quantum simulations of this organism in the first place is in order to study its notably high quantum transport efficiency despite the presence of such decoherence and loss. These issues are explored further in Ch. 7, and a waveguide array simulation which includes decoherence is undertaken. However, in the first instance we neglect such effects here and focus on simulating the remaining unitary dynamics, which will then be described by a 16×16 Hamiltonian of the form (5.3). Non-unitary dynamics could potentially be added back in to the simulation using methods similar to those in Ch. 7 after first succeeding in faithfully reproducing the Hamiltonian.

The target Hamiltonian $\mathcal{H}_{\text{B850}}$, calculated in Ref. [38] using measured data [42, 43], is shown in Table 5.1. Note that all the diagonal entries are equal, which means each waveguide will need to have the same propagation constant. Also of note are the negative values for some coupling constants. While the couplings between waveguide pairs are always positive, simulating the absolute value of $\mathcal{H}_{\text{B850}}$ will yield the same dynamics for the site occupancy in the single-exciton manifold.

Due to the distance dependence of dipole-dipole coupling, the coupling terms between chromophores separated by more than a few sites on the ring is very small compared to that between neighboring sites. The initial idea for this simulation [38] was therefore to neglect those V_{jk} in $\mathcal{H}_{\text{B850}}$ of less than 50 cm^{-1} . This leaves only four coupling terms: $V_{12} = 806 \text{ cm}^{-1}$, $V_{13} = -152 \text{ cm}^{-1}$, $V_{23} = 377 \text{ cm}^{-1}$, and $V_{24} = -102 \text{ cm}^{-1}$. Simulating the remaining dynamics requires arranging 16 waveguides in a ring such that $C_{12} = b|V_{12}|$, $C_{13} = b|V_{13}|$, $C_{23} = b|V_{23}|$, and $C_{24} = b|V_{24}|$, and so forth for all the other chromophore pairs separated by three or less sites, with the remaining C_{jk} much smaller. Here b is a proportionality constant

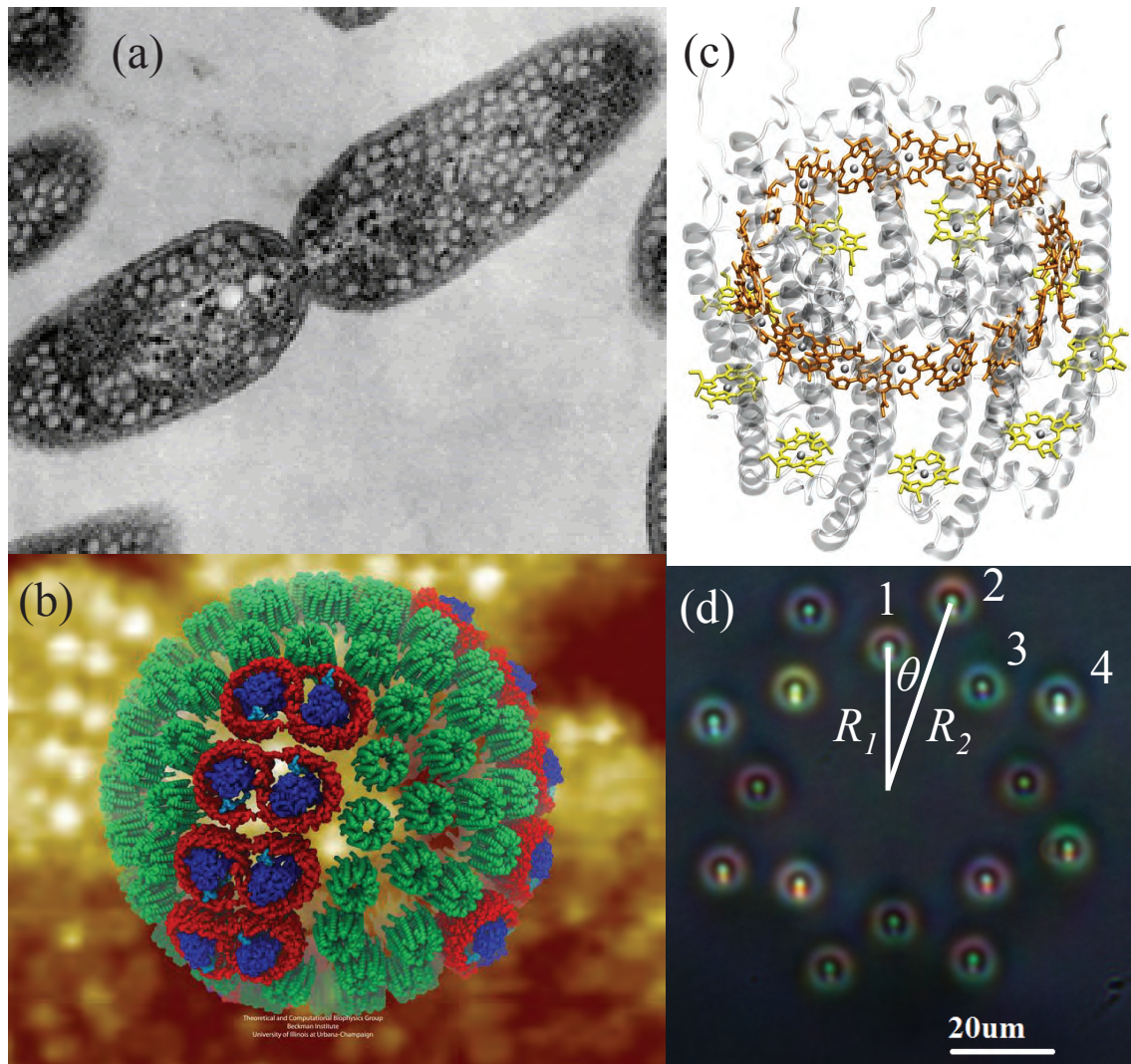


Figure 5.4: (a) Microscope image of a *Rhodospirillum rubrum* purple photosynthetic proteobacterium [39]. (b) A model of a purple bacteria chromatophore vesicle, an organelle involved bacterial light harvesting. Photoinduced excitons in the light-harvesting system I (red) and light-harvesting system II (LH-II; green) complexes are eventually transferred to the Reaction Centers (RCs) (blue) with near unit efficiency. Image sourced from Ref. [40]. (c) Model of the LH-II structure from Ref. [41], showing two subunits: the B800 subunit consisting of 9 bacteriochlorophylls shown in yellow, and the B850 subsystem consisting of 16 bacteriochlorophylls shown in orange. Exciton coupling in the latter can be described by a 16×16 Hamiltonian. (d) An annotated transmission differential interference contrast microscopy image of a prototype waveguide array for simulating the LH-II B850 Hamiltonian. The simulation goal is to engineer the waveguide index profiles and their geometrical arrangement, as parametrized here by R_1 , R_2 , and θ , such that the waveguide Hamiltonian approximates the B850 Hamiltonian—shown in Table 5.1—as faithfully as possible. Only the first four waveguides are numbered but the indexing continues in the obvious manner.

which defines the relationship between the B850 evolution time T which is simulated and the distance Z propagated in the waveguide array: $bZ = T$. Note that the simulation time must here be measured in cm as all the relevant couplings are in cm^{-1} , and also that Z is the optical distance *i.e.* $Z = n_{\text{eff}}L$ where L is the physical circuit length.

If the coupling between the pairs of identical waveguides depends only on their separation r , and the 16 waveguides are arranged in two concentric octagons of respective radius R_1 and R_2 with a relative angle θ as shown in Fig. 5.4(d), then the optimal simulation parameters which determine the waveguide positions can be found by optimally matching the four largest C_{jk} values to the corresponding V_{jks} . This requires solving the following system of equations for the four unknowns b , R_1 , R_2 , and θ :

$$\begin{aligned} C_{jk}[r(R_1, R_2, \theta)] &= b|V_{jk}|, \\ \{(j, k)\} &= \{(1, 2), (1, 3), (2, 3), (2, 4)\}. \end{aligned} \quad (5.4)$$

As a first approximation, the coupling between waveguide pairs can be modeled as decreasing exponentially with separation r :

$$C(r) = C_0 e^{-r/r_0}, \quad (5.5)$$

for some constants C_0 and r_0 . Using data in Ref. [34], these were estimated at $C_0 = 10.1 \text{ cm}^{-1}$ and $r_0 = 9.0 \text{ }\mu\text{m}$ for some plausible laser-written waveguides. The four equations (5.5) can then be given explicitly [38]:

$$|V_{12}| = 806 \text{ cm}^{-1} = \frac{C_0}{b} \exp\left(-\frac{1}{r_0} \sqrt{R_1^2 + R_2^2 - 2R_1R_2 \cos \theta}\right) \quad (5.6)$$

$$|V_{13}| = 152 \text{ cm}^{-1} = \frac{C_0}{b} \exp\left(-\frac{2R_1}{r_0} \sin \frac{\pi}{8}\right) \quad (5.7)$$

$$|V_{23}| = 377 \text{ cm}^{-1} = \frac{C_0}{b} \exp\left(-\frac{1}{r_0} \sqrt{R_1^2 + R_2^2 - 2R_1R_2 \cos\left(\frac{\pi}{4} - \theta\right)}\right) \quad (5.8)$$

$$|V_{24}| = 102 \text{ cm}^{-1} = \frac{C_0}{b} \exp\left(-\frac{2R_2}{r_0} \sin \frac{\pi}{8}\right), \quad (5.9)$$

yielding a solution for the simulation parameters of

$$\begin{aligned} R_1 &= 35.3 \text{ }\mu\text{m} & R_2 &= 40.0 \text{ }\mu\text{m} \\ \theta &= 0.295 & b &= 3.32 \times 10^{-3}. \end{aligned} \quad (5.10)$$

This solution resulted in waveguide separations ranging from $r_{12} = 12.0 \text{ }\mu\text{m}$ to $r_{24} = 36.0 \text{ }\mu\text{m}$

for the four targeted coupling constants, and a total expected simulation error, including all the longer-distance couplings, of

$$\frac{\|\mathcal{H}_{\text{mod}} - \mathcal{H}_{\text{B850}}\|_2}{\|\mathcal{H}_{\text{B850}}\|_2} = 0.02. \quad (5.11)$$

Here $\mathcal{H}_{\text{B850}}$ is the target Hamiltonian given in Table 5.1, \mathcal{H}_{mod} is the modeled Hamiltonian of the waveguide array, and the norm is the L_2 -norm [38]. Given a 10 cm interaction length—on the long end of what is achievable in laser written waveguides due to writing stage translation limits as well as sample availability—and an effective waveguide index of $n_{\text{eff}} = 1.45$, this should result in an effective simulation length of about 255 fs, more than long enough to observe coherent delocalization dynamics which occur in the B850 subunit on a 10 fs timescale [38].

In the following sections we consider more physically realistic waveguide array models and how they can be used to simulate $\mathcal{H}_{\text{B850}}$.

5.3.2 Practical considerations: realistic coupling curves and determining dynamics

In considering more realistic models to use in designing a B850 simulation waveguide array for fabrication, detailed knowledge of the inter-waveguide coupling behavior is crucial. The fundamental premise of the simulation is to use knowledge of the functional dependence of waveguide coupling C on separation r to precisely place the 16 waveguides in order to approximate the target Hamiltonian; $C(r)$ will be referred to as the coupling curve.

Several approximations were used in the initial theory for this simulation concerning issues which would need to be considered further in order to model and design a realistic simulator circuit. Such considerations include:

1. **The functional shape of the coupling curve:** The assumption of an exponential dependence of coupling on inter-waveguide distance as in Eq. (5.5) is highly unphysical except for very large separations. The coupling between two waveguides is proportional to the overlap integral between the guided modes (see Sec. 5.2.2), and in order to have an exponentially-decaying mode shape outside the core, a waveguide would need an infinitesimally-narrow index profile $n(r)$ which would, of course, not support a guided mode. A somewhat more plausible—although still ultimately unphysical (see

Sec. 5.2.2)—model would be a coupling curve which was a two-dimensional Gaussian *i.e.* $C(r) = C_0 e^{-(r^2/\sigma^2)}$ for some constants C_0 and σ ; a Gaussian coupling curve would result from Gaussian mode-shapes as the overlap integral of two Gaussians is, itself, Gaussian. An example of a modelable, physical index profile is a circular ‘top-hat’ step function. This yields modes which are modified Bessel functions outside the core; the overlap integral will then be a complicated function best analyzed numerically. In fact the coupling curve can be evaluated numerically in any case but this requires knowledge of $V(r)$ for the waveguides.

2. **Coupling anisotropy:** In practice the transverse index profiles $n(x, y)$ of laser-written waveguides are imperfectly symmetrical, and therefore the coupling between two waveguides will depend not on the the transverse scalar distance r but rather the vector displacement \mathbf{r} : $C_{jk} = C(\mathbf{r}_{jk})$. In designing a B850 simulation circuit for fabrication it may be possible to compensate for some degree of anisotropy by modifying the waveguide formation. For instance, in the plausible case that the coupling curve can reasonably be modeled as two-dimensional Gaussian with different width parameters in the x and y directions, at least at a separation which is significantly longer than the core width parameters, then the simulation could be achieved by modifying the concentric rings in the simulator to be elliptical instead of circular. In a more general case, depending on the degree and kind of coupling anisotropy, one could plausibly numerically optimize over the semi-major axis orientations and ellipticities of the concentric waveguide rings in order to find a waveguide arrangement with a sufficiently low simulation error; this would be a further generalization of the kind of optimization discussed in further detail in Sec. 5.3.4.
3. **The polarization-dependence of the coupling curve:** As discussed in Sec. 5.2.3 above, the coupling between laser-written waveguides can exhibit polarization-dependence and birefringence for several reasons. For this simulation, it is only necessary to know the coupling for one polarization state, as long as that state is a polarization eigenstate of each waveguide—*e.g.* if the fast and slow axes of each individual waveguide correspond respectively to x and y polarization, then it is sufficient to know $C(\mathbf{r})$ for x -polarized light in order to design the simulator. However, the differing ‘neighborhoods’ of each waveguide in terms of the spatial arrangement of its neighbors is likely to cause slightly different rotations in the effective birefringent axes of each waveguide, in essentially a much lower-amplitude case of the effect exploited in Ref. [32] for creating laser-written waveplates with rotated axes. For this reason it would be best to minimize the polarization-dependence of the interwaveguide coupling in the simulation circuit as well; the obvious first step towards achieving this is to obtain an index potential with

circular symmetry to the best extent possible.

4. **Other waveguides:** The theory as explained thus far assumes that the coupling between two waveguides is dependent only on the overlap between the guided modes of those two waveguides in a uniform cladding. Of course, in an array of many waveguides the cladding is not uniform, but is rather populated with other waveguides, which will perturb the coupling between non-neighboring waveguide pairs. In particular in this simulation, with reference to Fig. 5.4(d), waveguide 3 might significantly perturb C_{14} and waveguide 2 might similarly perturb C_{13} , for example.
5. **Applicability of the tight-binding approximation:** As developed so far, the theory behind this simulation assumes that the waveguides are weakly-coupled in order to employ the tight-binding Hamiltonian in Eq. (5.3). However this approximation breaks down for waveguides which are closely-separated compared to the widths of their guided modes. We will return to this issue in Sec. 5.3.4.

In order to approximately quantify the effects of these considerations on the simulation viability and to explore possibilities for their mitigation it was necessary to investigate more accurate models of waveguide arrays.

A further important consideration left unaddressed in the initial proposal for this experiment concerns the need to determine the simulator dynamics in order to find the simulated Hamiltonian. Measuring output distributions after a single simulation time will be insufficient to determine the internal simulator dynamics. Even full quantum process tomography would only yield a measurement of the system superoperator or process matrix, but not of the Hamiltonian which generated it. (see Sec. 2.1.5 and 2.1.5.1). However, recently efficient techniques have been developed for characterizing N -mode, approximately unitary optical circuits using only single- and two-mode input states and output intensity measurements [44]; see Sec. 8.3.1. By performing such measurements for several propagation lengths in otherwise-identical \mathcal{H}_{B850} simulation arrays, it should be possible to deduce the underlying Hamiltonian. Furthermore it is plausible that the simulated Hamiltonian could be bounded with even fewer measurements, supplemented by bounds on the waveguide characteristics.

5.3.3 Modeling waveguide arrays

Two general strategies exist to model arrays of coupled waveguides. The first is an analytical approach called coupled-mode theory (CMT) in which the eigenmodes of a two-waveguide

system are approximated as linear combinations of the individual waveguide eigenmodes. Coupling rates can then be found by treating each waveguide as a perturbation of the other. An introduction to this approach can be found in Ch. 29 of Ref. [21], while a thorough treatment is contained in Ref. [45]. In its conventional formulation, this approach is accurate only for well-separated, weakly-guiding waveguides which are weakly coupled [21]; in this case it is equivalent to the tight-binding approximation and will thus yield a Hamiltonian of the form (5.3) for an array of N weakly-coupled waveguides.

The other strategy, which has become much more practical in recent decades due to increasing computer processor speeds, is to use finite-element methods to numerically solve the paraxial Helmholtz equation (essentially Eq. (5.1)) on a grid. These are referred to as finite-difference beam propagation methods (FD-BPM) methods, and commercial software packages exist to employ them. For work in this thesis we have used *RSoft* [46], a software package that includes a computer-aided design (CAD) suite for designing integrated optical circuits and several modules for numerically simulating the behavior of light in the CAD circuits, including *BeamPROP* which implements FD-BPM on waveguide arrays.

Of these two strategies, FD-BPM has the advantage of many fewer required approximations. In particular neither weak guidance nor weak coupling need be assumed, and there even exist techniques such as wide-angle FD-BPM to deal with some degree of non-paraxiality. Furthermore the dynamics calculated using FD-BPM do not rely on a known coupling curve and will automatically account for the presence of all waveguides without the need to explicitly consider each waveguide $j \in N$ to be perturbing the couplings C_{kl} , $\{k, l\} \neq j$. On the other hand, simply calculating the dynamics of an array of waveguides using FD-BPM yields only approximate results for the amplitude and phase in each waveguide at each distance z , but not an explicit expression for the Hamiltonian describing the evolution. CMT does yield such an explicit expression, which may have a functional dependence on simulation parameters such as waveguide separation. CMT is also generally less computationally intensive than FD-BPM, at least for situations including strong coupling and weak binding where accurate FD-BPM requires a large grid size and finely-grained spatial and temporal steps. For these reasons I found CMT to be more amenable to multivariate nonlinear optimization—addressed further in Sec. 5.3.4—of the approximate Hamiltonian implemented in the waveguide array, where the optimization is over variations in simulation parameters such as waveguide index profile and geometric quantities *e.g.* R_1 , R_2 , and θ .

Of course, both of these modeling methods depends on microscopic knowledge of the waveguide properties, most importantly the index profile $n(x, y)$ and any material birefringence. Unfortunately, microscopic knowledge of laser-written waveguide index profiles is

difficult to obtain and to model due to several factors: the complicated spatial dependence of the index profile $n(x, y)$, especially for non-annealed waveguides written in regimes with a moderate amount of cumulative heating, as evidenced in Fig. 5.3(a); the generally significant error margins associated with index measurement tools such as index profilometers⁴; and the day-to-day variability of waveguides written with the same ‘recipe’ due to factors such as fluctuations in laser power and alignment, substrate properties, and even humidity.

For these reasons the following general strategy was adopted to optimize simulation parameters:

1. Conduct parameter studies using recipes which should, based on previous knowledge on the part of the fabricators, yield single-mode waveguides in at least part of the optical spectrum and which, ideally, are expected to produce a dependence of C on \mathbf{r} similar to that used for the initial B850 theory in [38].
2. In these parameter studies, determine $C(\mathbf{r})$ for the various recipes by measuring the output intensities in two coupled waveguides after a known propagation distance as a function of separation. This method is detailed further in Sec. 7.3.1 and even further in Ref. [34].
3. Find simple index profiles $n(x, y)$, such as Gaussian or ‘top-hat’ profiles, which yield coupling curves as similar as possible to those determined in the parameter studies, at least for long- and intermediate-distance couplings. We will refer to these as the model index profiles corresponding to the recipe.
4. Apply CMT to the model index profiles determined in the previous step in order to find optimal array geometry parameters R_1 , R_2 , and θ .
5. Model the resulting array, with the model index profiles, using FD-BPM in *RSoft* to check for significant deviations from the dynamics expected according to CMT.
6. Iterate the previous steps as needed.

5.3.4 Preliminary results and accounting for strong coupling

Our first iteration of the strategy enumerated above yielded important results. We conducted initial parameter studies to determine the coupling curve for some achievable waveguide recipes. Note that in this initial instance we were not investigating coupling anisotropy

⁴As stressed in private communication with M. Withford, M. Ams, and T. Meany.

but merely the dependence of coupling on separation for waveguide pairs spaced parallel to the sample surface.

Using the measured coupling curve, we determined parameters $\{R_1, R_2, \theta, b\}$ for a waveguide array \mathcal{H}_{B850} simulator using the four-equation method (5.5) employed in Sec. 5.3.1. We then modeled the dynamics in this waveguide array using both conventional CMT and FD-BPM. Our initial results are shown in Fig. 5.5(b) and (c). The ideal dynamics of \mathcal{H}_{B850} are shown in Fig. 5.5(a) for comparison.

The results of modeling using FD-BPM were vastly different from those obtained using conventional CMT and from the target dynamics, as seen in Fig. 5.5(b) and (c). The primary reason for this quickly became apparent: the determined positions of the waveguides were far too close compared to the widths of their guided modes, thus invalidating the use of the weak coupling approximation—on which the use of a tight-binding Hamiltonian of the form (5.3) relies. When the separation between a pair of coupled waveguides is small compared to the widths of the guided modes, the system eigenmodes can no longer reasonably be treated as superpositions of the individual waveguide eigenmodes. In particular, when the entirety of the input light is in the mode—considered in isolation—of one waveguide, there may be significant occupancy of the neighboring mode, as can be seen in Fig. 5.5(c). This is because the modes of the two waveguides no longer exchange power only through a vanishing overlap between their evanescent tails, but rather the mode of each waveguide has significant overlap with the *core* of its neighbor. Furthermore, in this case the coupling between the modes cannot be accurately derived simply by considering each waveguide as a first-order perturbation to the other and using conventional CMT. Techniques to derive coupling constants in such cases exist under the name non-orthogonal coupled mode theory, and are detailed in [45].

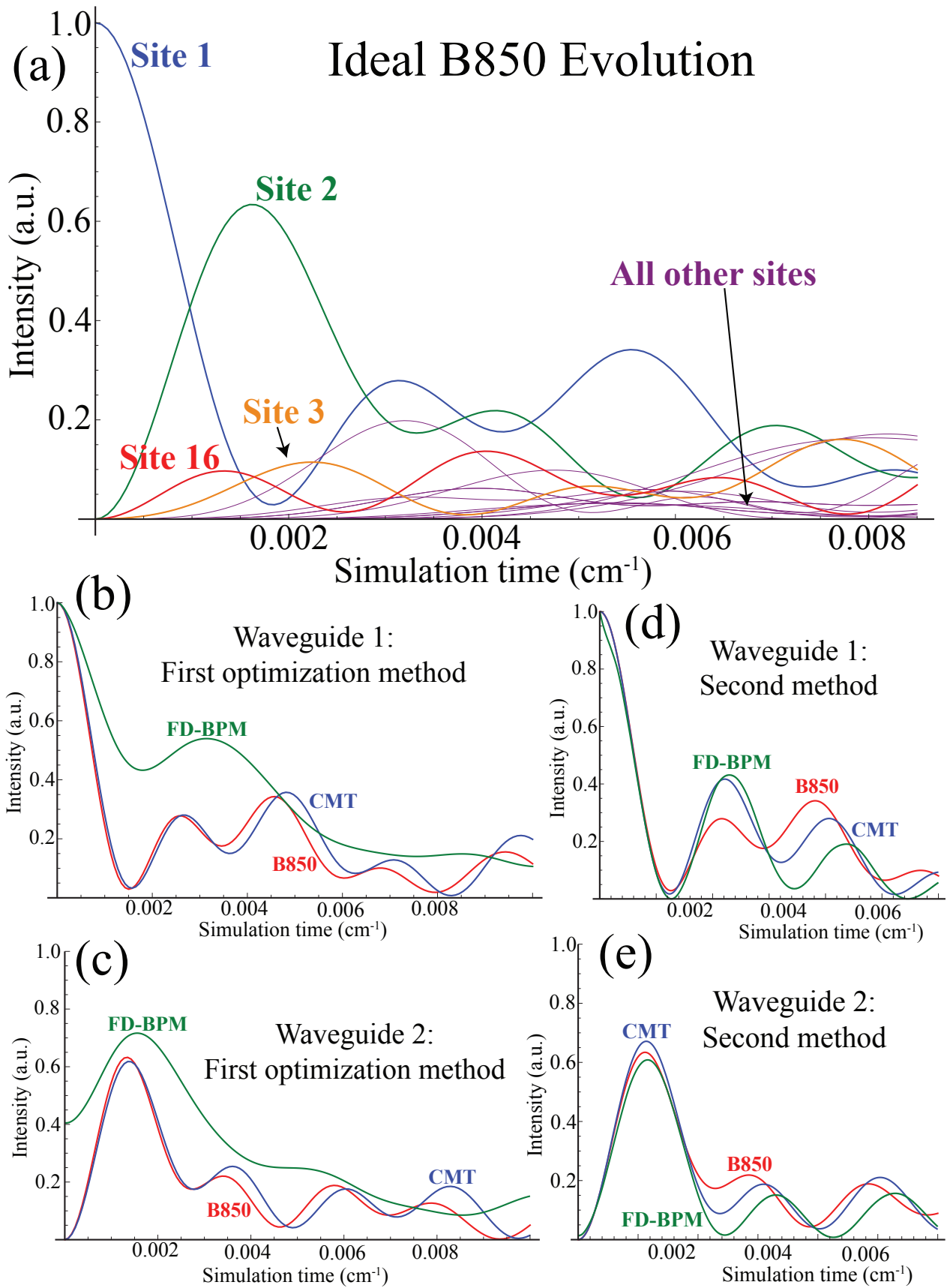
Based on these results we modified our approach to finding the optimal waveguide simulator parameters $\{R_1, R_2, \theta, b\}$. The four-equation method employed in Sec. 5.3.1 yields such small values for the radii R_1 and R_2 , and thus small separations between neighboring waveguides, because the value determined for b is large. By limiting the maximum value of b , thereby slowing the simulation rate—*i.e.* simulating less evolution time of \mathcal{H}_{B850} with each cm of waveguide array—we could ensure that the optimal spacing of the waveguides was larger, at the expense of some overall simulation error. We therefore employed the following new method: using sets of symmetric model index profiles $n(r)$ deemed potentially achievable in laser-written waveguides based on our initial parameter studies and consultation with our fabrication colleagues, we numerically determined the coupling between such waveguides as a function of separation using non-orthogonal CMT. We then found the optimal geometric parameters $\{R_1, R_2, \theta\}$ for a waveguide \mathcal{H}_{B850} simulator for these model index profiles by

numerically minimizing the simulation error:

$$E[n(r), \lambda, b_{\max}] = \min_{(R_1, R_2, \theta, b)} \left(\frac{\|\mathcal{H}_{\text{B850}} - \mathcal{H}_{\text{CMT}}(R_1, R_2, \theta)\|_F}{\|\mathcal{H}_{\text{B850}}\|_F} \right), \quad (5.12)$$

where $\|M\|_F = \sqrt{MM^\dagger}$ denotes the Frobenius norm of matrix M , \mathcal{H}_{CMT} is the Hamiltonian

Figure 5.5 (*facing page*): Target dynamics of the B850 Hamiltonian, and dynamics of models for waveguide simulators of that Hamiltonian with parameters found via two different methods. In each subfigure, site or waveguide 1 is initially excited. (a): The dynamics of the population of each of the 16 sites in the LH-II B850 subunit under the action of the Hamiltonian $\mathcal{H}_{\text{B850}}$, given in Table 5.1. Site 1 and its three closest neighbors are highlighted in blue, green, red, and orange respectively, and all the other sites are shown in purple. (b) and (c): The modeled dynamics of the population of the first two waveguides, respectively, in a waveguide simulator of $\mathcal{H}_{\text{B850}}$. Here the parameters $\{R_1, R_2, \theta, b\}$ were found using the four-equation method of Eq. (5.5), and the waveguides are modeled using the model index profiles (see Item 3 on p. 78) resulting from our first waveguide parameter studies. In each subfigure the blue line shows the results of tight-binding coupled-mode theory (CMT) based on the measured coupling curve, while the green line shows the results of finite-difference beam propagation methods (FD-BPM) using the model index profiles. The red line shows the dynamics of the corresponding site in the B850 subunit under $\mathcal{H}_{\text{B850}}$. Note the large deviations of the waveguide dynamics modeled using FD-BPM from the target dynamics, and particularly the large overlap between the guided modes of waveguide 1 (the excited one) and waveguide 2, as evidenced by the large initial population in waveguide 2. This is evidence of the invalidity of the weak coupling and/or tight binding approximations for this waveguide arrangement. (d) and (e): The modeled dynamics of the population of the first two waveguides, respectively, in a waveguide simulator of $\mathcal{H}_{\text{B850}}$. In this case the parameters $\{R_1, R_2, \theta, b\}$ were found using the improved optimization method of Eq. (5.12), using waveguide index profiles which are different from those in (b) and (c), but appeared to be plausibly achievable model index profiles based on the results of our first parameter studies and the advice of our fabrication collaborators. Again the blue line shows the results of tight-binding CMT, this time based on a simulated coupling curve determined for our model index profiles but still assuming tight binding, while the green line shows the results of FD-BPM using the same model index profiles. The red line again shows the dynamics of the corresponding site in the B850 subunit under $\mathcal{H}_{\text{B850}}$. Here the deviations of the FD-BPM results from the other dynamics are much less significant, and in particular the mode overlap of adjacent waveguides has decreased by over an order of magnitude.



(Caption on facing page.)

of the waveguide array of the form (5.3) but using couplings found for the model index profile $n(r)$ using non-orthogonal CMT, and the minimization is subject to the constraint $b \leq b_{\max}$. Note that we also optimized over possible variations in the excitation wavelength λ within the visible and near-infrared spectrum. Ultimately we determined to focus on simulations with 820 nm light as that is the wavelength of our single-photon sources using spontaneous parametric downconversion (SPDC).

Using this method we were able find various sets of parameters $\{n(r), R_1, R_2, \theta, b\}$ for which the expected simulation error E is less than 10% and the maximum overlap between nearest neighbor waveguides would be less than 1.5%. The dynamics of one such solution are shown in Fig. 5.5(c) and (d). However, these parameter sets depended on model index profiles $n(r)$ which are plausible based on previous parameter studies and the advice of fabrication collaborators but which have not yet been demonstrated with laser-written waveguides. Further parameter studies focused on achieving such waveguides would ultimately be necessary to optimally employ this approach.

5.3.5 Prototype measurement and results

Based on values for R_1 , R_2 , and b obtained using the optimization method described in the preceding section, and using waveguide recipes expected by our fabrication collaborators to produce desirable index profiles, 80 prototype B850 simulation circuits were produced. The geometric parameters and index profile were varied around the expected optima between the 80 circuits. These circuits were not expected to yield an accurate simulation of $\mathcal{H}_{\text{B850}}$ due to our large uncertainty as to the index profiles and birefringent characteristics of the waveguides. Nonetheless we decided to characterize the output intensity patterns for single-mode inputs for several of these arrays as function of the input mode.

The measurement procedure was as follows: light from an 820 nm diode laser was coupled into single-mode fiber, and fiber polarization controllers were used to ensure horizontal polarization. This fiber was then butt-coupled to the input waveguide using precision six-axis translation stages. The circuit output was imaged onto a charge-coupled device (CCD) camera using a microscope objective. Custom-written software was employed to ensure optimal coupling into the circuit and focusing onto the CCD sensor, as well as to adjust the laser intensity such that the camera was sufficiently illuminated without being saturated, and the illuminated pixels would display a nearly linear response. By coupling into different input waveguides without adjusting the circuit or camera positions, this software enabled several output images for different waveguides to be aggregated in order to determine a calibration

map of the pixel areas on the CCD sensor corresponding to the image of each output waveguide. The output intensity for each waveguide, for a given input, could then be determined by summing the pixel values within the predetermined CCD area. An example calibration image as well as the output distribution from a particular input waveguide for one prototype circuit are shown in Fig. 5.6.

The primary result of these measurements was to demonstrate that the extent of the coupling anisotropy using these waveguides was unfortunately severe, as shown in Fig. 5.7. This became evident by examining the output intensity distribution for different input waveguides, relative to that input waveguide. If the waveguide coupling were isotropic, then for any odd-indexed input waveguide $n \in \{1, \dots, 16\}$, the output distribution should be identical after re-indexing the output waveguides $\{m\} \in \{1, \dots, 16\}$ to $\{(m-n+1 \bmod 16)\}$ (and similarly for the even-indexed input waveguides). Fig. 5.7 shows these distributions for all 16 input waveguides for one of our prototype simulation circuits; unfortunately the distributions are highly unequal. Further measurements also demonstrated a significant degree of circuit polarization-dependence, as the output distributions for vertically-polarized input light were found to be significantly different from those for horizontal input illumination.

5.3.6 Conclusions and prospects for further investigations

Following these results, a critical examination was undertaken of the demanding requirements for this simulation project *vis-a-vis* the currently-demonstrated technological capabilities of laser-written waveguides. Due to the simultaneous needs for particular mode shapes and coupling curves, minimal birefringence and coupling anisotropy, and in particular meticulous characterization of coupling curve over a large range of waveguide displacements encompassing both distance and direction, it was ultimately decided to put this simulation on hiatus until such time as laser-written waveguide technology had further matured.

However, the design, modeling, and measurement techniques developed during the course of this project and delineated in this chapter significantly inform the remaining chapters of the thesis. This is particularly true for Ch. 7 where a smaller Hamiltonian of a particular structure, along with decoherence and targeted absorption, are simulated in a laser-written waveguide array in order to investigate an important quantum transport phenomenon.

The prospects for a laser-written waveguide \mathcal{H}_{B850} simulator have significantly improved since the bulk of this research was undertaken in 2010-2012. In particular, the recently-demonstrated increases in control over the polarization behavior of laser-written waveguides

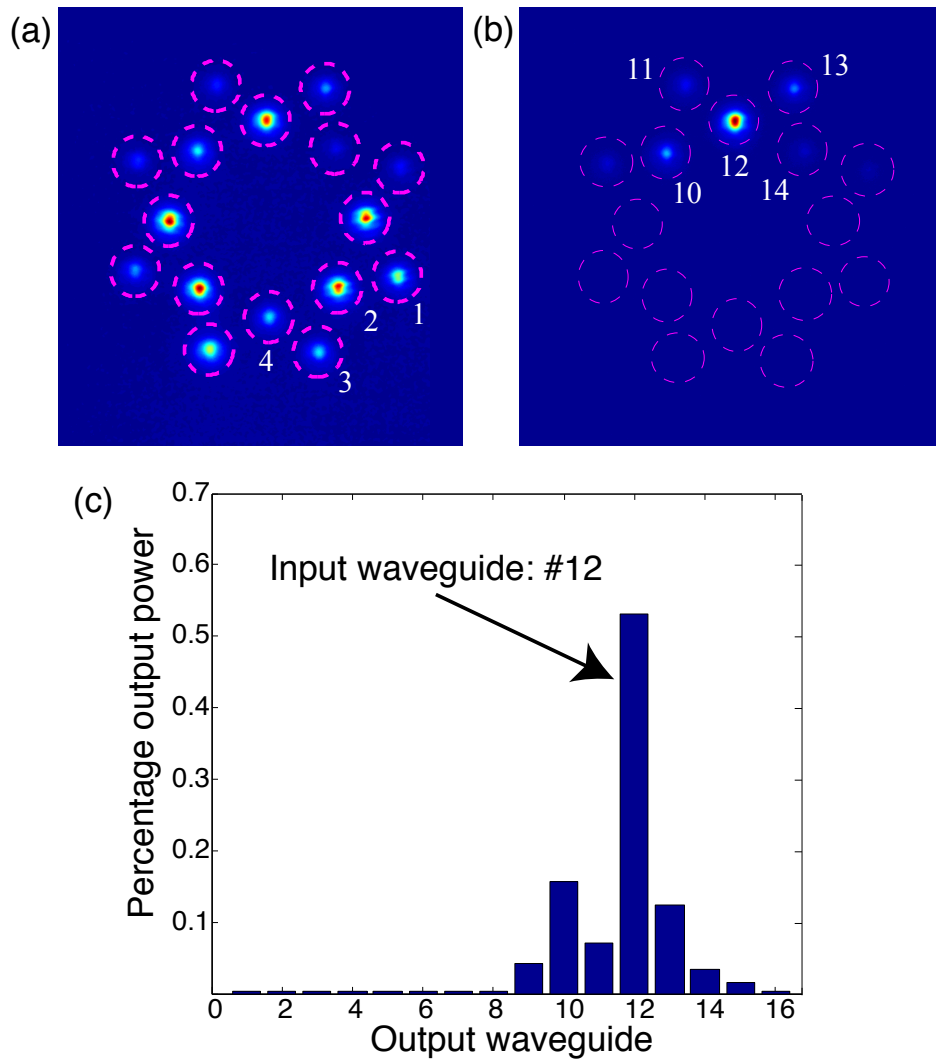


Figure 5.6: (a) An example false-color calibration image produced for a B850 simulation prototype waveguide circuit. This image is an aggregate of the images resulting from several different input waveguides, and used to find the positions of the waveguide outputs on the CCD. The dotted pink circles show the pixel areas assigned to each output waveguide on the CCD camera and correspond to three standard deviations on a two-dimensional Gaussian profile fitted to the local pixel values. Waveguides 1 to 4 are labeled; the labels continue in similar fashion around the ring. Note that the waveguide index used here is different than in Fig. 5.4(d), and in particular the even-indexed waveguides now form the inner ring and vice-versa. (b) A measurement of the circuit output when waveguide 12 is the input mode, using the determined calibration map. (c) The percentage of the output power in each waveguide when waveguide 12 is illuminated. These values were determined by summing all the pixel values within the corresponding pixel area (pink ring) for each waveguide after background subtraction.

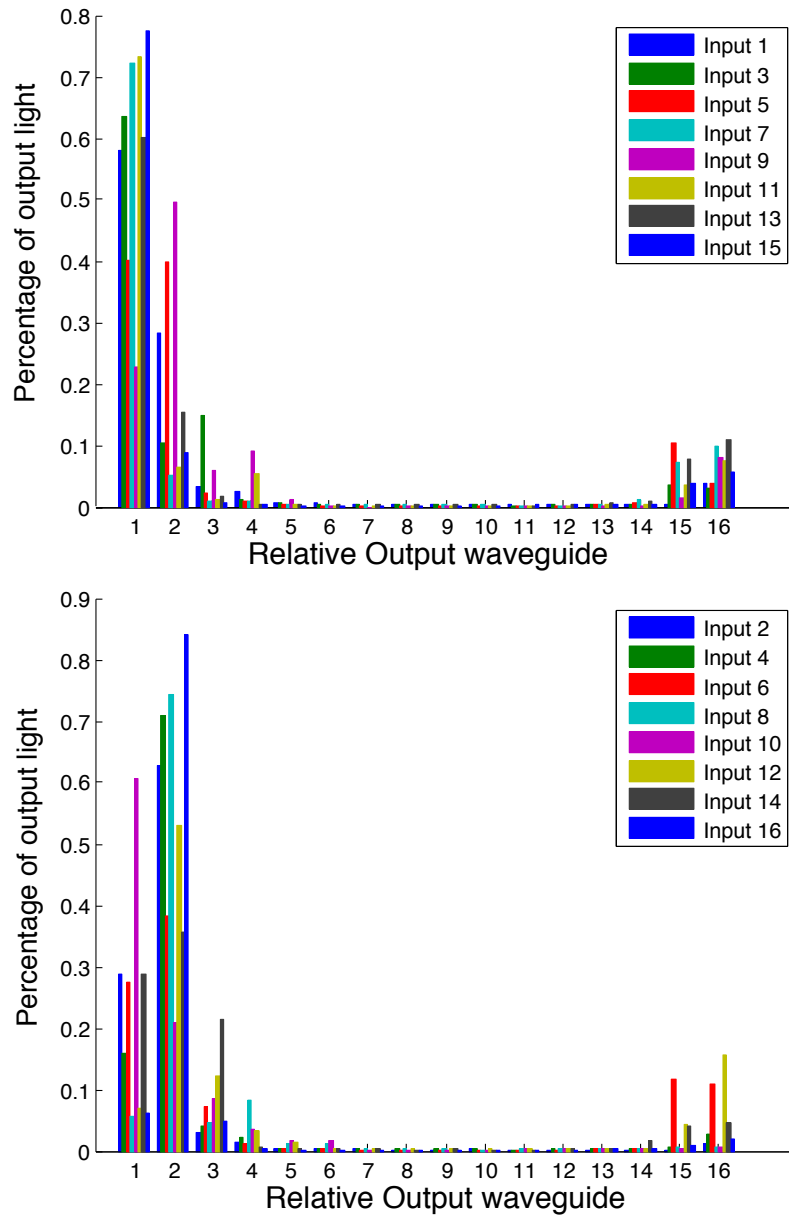


Figure 5.7: The output light distribution for all 16 input waveguides in a prototype B850 Hamiltonian simulation waveguide circuit. Each individual output distribution is measured in a similar manner to Fig. 5.6(b) and (c). The top figure shows the distribution for the odd-indexed input waveguides, *i.e.* the outer octagon. See Fig. 5.6(a) for a visualization of the circuit geometry. The bottom figure shows the distribution for even-indexed inputs. In both graphs the output indices are relative to the input waveguide, *i.e.* for the odd-indexed input waveguide n , the output waveguides $\{m\}$ are relabeled to $\{(m-n+1 \bmod 16)\}$, and similarly for the even inputs. This is done so that the distributions should be identical if the circuit geometry and coupling are entirely symmetrical and isotropic, *i.e.* all eight bars corresponding to each output index would be the same height. The significant differences between the demonstrated output distributions are evidence of significant coupling anisotropy.

(see Sec. 5.2.3), along with the refinement of the annealing technique demonstrated in Fig. 5.3, suggest an increased viability of achieving isotropic coupling for at least one polarization eigenstate in a many-mode circular waveguide array. Furthermore there have been continued improvements in waveguide array characterization techniques, some of which are employed in subsequent chapters; in theoretical understanding of laser-induced material modification mechanisms in different writing regimes; and in operational knowledge of different waveguide fabrication recipes. Finally, the aforementioned simulation of a particular Hamiltonian structure in Ch. 7 sets the stage for further advances in the field of waveguide array simulations of non-trivial Hamiltonians.

References

- [1] Politi, A., Cryan, M. J., Rarity, J. G., Yu, S. & O’Brien, J. L. Silica-on-silicon waveguide quantum circuits. *Science* **320**, 646–649 (2008). 58, 59
- [2] Politi, A., Matthews, J. C. F. & O’Brien, J. L. Shor’s quantum factoring algorithm on a photonic chip. *Science* **325**, 1221 (2009). 58, 59
- [3] Smith, B. J., Kundys, D., Thomas-Peter, N., Smith, P. G. R. & Walmsley, I. A. Phase-controlled integrated photonic quantum circuits. *Opt. Express* **17**, 13516–13525 (2009). 58, 64
- [4] Li, H. W. *et al.* Reconfigurable controlled two-qubit operation on a quantum photonic chip. *New J. Phys.* **13**, 115009 (2011). 58, 59
- [5] Shadbolt, P. J. *et al.* Generating, manipulating and measuring entanglement and mixture with a reconfigurable photonic circuit. *Nature Photon.* **6**, 45–49 (2012). 58, 59
- [6] Sprengers, J. P. *et al.* Waveguide superconducting single-photon detectors for integrated quantum photonic circuits. *Appl. Phys. Lett.* **99**, 181110 (2011). 58, 60
- [7] Peruzzo, A. *et al.* Quantum walks of correlated photons. *Science* **329**, 1500 (2010). 59
- [8] Silverstone, J. W. *et al.* On-chip quantum interference between silicon photon-pair sources. *Nature Photon.* **8**, 104–108 (2013). 59
- [9] Alibart, O., Ostrowsky, D. B., Baldi, P. & Tanzilli, S. High-performance guided-wave asynchronous heralded single-photon source. *Opt. Lett.* **30**, 1539 (2005). 60
- [10] Bonneau, D. *et al.* Fast path and polarization manipulation of telecom wavelength single photons in lithium niobate waveguide devices. *Phys. Rev. Lett.* **108**, 053601 (2012). 60
- [11] Jin, H. *et al.* Reconfigurable on-chip entangled sources based on lithium-niobate waveguide circuits. *arXiv:1404.0274* (2014). 60
- [12] Lobino, M. *et al.* Correlated photon-pair generation in a periodically poled MgO doped stoichiometric lithium tantalate reverse proton exchanged waveguide. *Appl. Phys. Lett.* **99**, 081110 (2011). 60
- [13] Sahin, D. *et al.* Waveguide photon-number-resolving detectors for quantum photonic integrated circuits. *Appl. Phys. Lett.* **103**, 111116 (2013). 60

- [14] Pernice, W. H. P. *et al.* High-speed and high-efficiency travelling wave single-photon detectors embedded in nanophotonic circuits. *Nature Communications* **3**, 1325+ (2012). [60](#)
- [15] Ams, M. *Fabrication of Optical Waveguide Devices in Bulk Materials Using Femtosecond Laser Pulses*. Ph.D. thesis, Macquarie University (2008). [60](#), [63](#), [67](#)
- [16] Itoh, K., Watanabe, W., Nolte, S. & Schaffer, C. B. Ultrafast processes for bulk modification of transparent materials. *MRS Bulletin* **31**, 620–625 (2006). [60](#), [61](#), [62](#)
- [17] Meany, T. *Laser Written Integrated Photonics for Quantum Information Science*. Ph.D. thesis, Macquarie University (2014). Preliminary examiner’s draft. [60](#), [61](#), [67](#)
- [18] Streltsov, A. M. & Borrelli, N. F. Study of femtosecond-laser-written waveguides in glasses. *J. Opt. Soc. Am. B* **19**, 2496 (2002). [61](#)
- [19] Bricchi, E., Klappauf, B. G. & Kazansky, P. G. Form birefringence and negative index change created by femtosecond direct writing in transparent materials. *Opt. Lett.* **29**, 119–121 (2004). [62](#)
- [20] Longhi, S. Quantum-optical analogies using photonic structures. *Laser Photon. Rev.* **3**, 243–261 (2009). [63](#), [68](#)
- [21] Snyder, A. W. & Love, J. *Optical Waveguide Theory* (Chapman and Hall, 1983). [63](#), [77](#)
- [22] Gloge, D. Weakly guiding fibers. *Appl. Opt.* **10**, 2252–2258 (1971). [63](#)
- [23] Marshall, G. D. *et al.* Laser written waveguide photonic quantum circuits. *Opt. Express* **17**, 12546–12554 (2009). [64](#)
- [24] Sansoni, L. *et al.* Polarization entangled state measurement on a chip. *Phys. Rev. Lett.* **105**, 200503 (2010). [65](#), [66](#)
- [25] Crespi, A. *et al.* Integrated multimode interferometers with arbitrary designs for photonic boson sampling. *Nature Photon.* **7**, 545–549 (2013). [64](#)
- [26] Heilmann, R., Keil, R., Grfe, M., Nolte, S. & Szameit, A. Ultraprecise phase manipulation in integrated photonic quantum circuits with generalized directional couplers. *Applied Physics Letters* **105**, – (2014). [65](#)
- [27] Reck, M., Zeilinger, A., Bernstein, H. & Bertani, P. Experimental realization of any discrete unitary operator. *Phys. Rev. Lett.* **73**, 58–61 (1994). [65](#)

- [28] Snyder, A. W. & Zheng, X.-H. Optical fibers of arbitrary cross sections. *J. Opt. Soc. Am. A* **3**, 600–609 (1986). [66](#)
- [29] Bhardwaj, V. R. *et al.* Stress in femtosecond-laser-written waveguides in fused silica. *Opt. Lett.* **29**, 1312–1314 (2004). [66](#), [67](#)
- [30] Crespi, A. *et al.* Integrated photonic quantum gates for polarization qubits. *Nat. Commun.* **2** (2011). [66](#)
- [31] Humphreys, P. C. *et al.* Strain-optic active control for quantum integrated photonics. *arXiv:quant-ph/1405.2694v1* (2014). [66](#)
- [32] Heilmann, R., Grafe, M., Nolte, S. & Szameit, A. Arbitrary photonic wave plate operations on chip: Realizing hadamard, pauli-x, and rotation gates for polarization qubits. *Sci. Rep.* **4** (2014). [66](#), [75](#)
- [33] Corrielli, G. *et al.* Rotated waveplates in integrated waveguide optics. *Nature Commun.* **5** (2014). [66](#)
- [34] Szameit, A., Dreisow, F., Pertsch, T., Nolte, S. & Tünnermann, A. Control of directional evanescent coupling in fs laser written waveguides. *Opt. Express* **15**, 1579–1587 (2007). [67](#), [70](#), [73](#), [78](#)
- [35] Arriola, A. *et al.* Low bend loss waveguides enable compact, efficient 3D photonic chips. *Opt. Express* **21**, 2978–2986 (2013). [67](#)
- [36] Meany, T. *et al.* Towards low-loss lightwave circuits for non-classical optics at 800 and 1,550 nm. *Appl. Phys. A* **114**, 113–118 (2013). [67](#), [68](#)
- [37] Tsai, T. & Thomas, G. Analog between optical waveguide system and quantummechanical tunneling. *American Journal of Physics* **44**, 636–638 (1976). [68](#)
- [38] Kassal, I. *Quantum Computation for Chemical Problems*. Ph.D. thesis, Harvard University (2010). [68](#), [69](#), [70](#), [72](#), [73](#), [74](#), [78](#)
- [39] Joint Genome Institute. Rhodobacter sphaeroides 2.4.1. The Regents of the U. of California (2014). URL genome.jgi-psf.org/rhosp/rhosp.home.html. [71](#)
- [40] Theoretical and Computational Biophysics Group. Molecular biophysics images (2014). URL www.ks.uiuc.edu/Gallery/Science/light_interacting_proteins/. This image was made by Melih Sener using VMD and is owned by the Theoretical and Computational Biophysics Group, NIH Center for Macromolecular Modeling and Bioinformatics, at the Beckman Institute, University of Illinois at Urbana-Champaign. [71](#)

- [41] User Aegon. Structure of LH2 complex of *Rsp. acidophila*. Wikimedia Commons (2006). URL commons.wikimedia.org/wiki/File:LH2-Structur.jpg. Reproduced under GFDL and CC-BY-SA licence. 71
- [42] Koepke, J., Hu, X., Muenke, C., Schulten, K. & Michel, H. The crystal structure of the light-harvesting complex II (B800–850) from *Rhodospirillum rubrum*. *Structure* **4**, 581–597 (1996). 70
- [43] Hu, X., Ritz, T., Damjanović, A. & Schulten, K. Pigment organization and transfer of electronic excitation in the photosynthetic unit of purple bacteria. *J. Phys. Chem. B* **101**, 3854–3871 (1997). 70, 72
- [44] Rahimi-Keshari, S. *et al.* Direct characterization of linear-optical networks. *Opt. Express* **21**, 13450–13458 (2013). 76
- [45] Huang, W.-P. Coupled-mode theory for optical waveguides: an overview. *J. Opt. Soc. Am. A* **11**, 963–983 (1994). 77, 79
- [46] URL <http://www.rsoftdesign.com/>. 77

Chapter 6

Two-photon quantum walks in an elliptical direct-write waveguide array

Published: *New Journal of Physics* **13**,(2011)

J. O. Owens¹, M. A. Broome¹, D. N. Biggerstaff¹, M. E. Goggin^{1,2}, A. Fedrizzi¹,
T. Linjordet³, M. Ams⁴, G. D. Marshall⁴, J. Twamley³, M. J. Withford⁴, A. G. White¹

¹*ARC Centre for Engineered Quantum Systems, ARC Centre for Quantum Computer and Communication Technology, School of Mathematics and Physics, University of Queensland, 4072 Brisbane, QLD, Australia*

²*Department of Physics, Truman State University, Kirksville, Missouri 63501, USA*

³*ARC Centre for Engineered Quantum Systems, Department of Physics and Astronomy, Macquarie University, North Ryde NSW 2109, Australia*

⁴*ARC Centre for Ultrahigh bandwidth Devices for Optical Systems, Centre for Quantum Science and Technology, MQ Photonics Research Centre, Department of Physics and Astronomy, Macquarie University, North Ryde NSW 2109, Australia*

Abstract

Integrated optics provides an ideal testbed for the emulation of quantum systems via continuous-time quantum walks. Here we study the evolution of two-photon states in an elliptic array of waveguides. We characterise the photonic chip via coherent-light tomography and use the

results to predict distinct differences between temporally indistinguishable and distinguishable two-photon inputs which we then compare with experimental observations. Our work highlights the feasibility for emulation of coherent quantum phenomena in three-dimensional waveguide structures.

6.1 Introduction

Computer modeling of complex systems has had spectacular success in modern science due to sophisticated approximation methods and steadily increasing computational power. However, classical simulation methods are ultimately impractical for modeling even moderately-sized quantum systems due to an exponentially-increasing parameter space. As first proposed by Feynman[1], a possible solution is for the model itself to operate via quantum instead of classical dynamics, either through *simulation*, in which a digital model on a quantum computer yields physical quantities as in e.g. [2, 3], or through *emulation*, in which a quantum system is modeled by a better-controllable system with a sufficiently similar Hamiltonian [4].

Quantum walks [5, 6]—an extension of the classical random walk into the quantum world—provide an ideal framework for emulation due to their rich dynamics [7–9]. There are two limiting cases, discrete and continuous. In discrete-time quantum walks, one or more (interacting) quantum particles (the so-called quantum coin) evolve on a graph, with their evolution governed by their internal quantum (coin) states. The discrete-time quantum walk on a line is the best studied example of such a walk and it has been demonstrated in a number of physical systems [10–14].

In continuous-time quantum walks, in contrast, there are no coin operations and the evolution is defined entirely in position space [15]. These walks require a well-controlled, continuous coupling between vertices, or lattice sites. Integrated optics is perfectly suited for this task and lithographically written, evanescently coupled surface waveguides were the first system used to demonstrate a quantum walk on a line with coherent light [16]. Unfortunately, surface waveguides can only realise simple, one-dimensional graphs with limited interconnectivity.

Physically more interesting three-dimensional structures can be engineered in laser written optical waveguide arrays in dielectric materials such as fused silica [17, 18], a platform that has been shown to have suitable fidelity for photonic quantum information processing [19]. The two-dimensional graphs that can be realised with this technique allow the study of new quantum walk phenomena, such as wave communication [20], cooperative quantum games

[21] and the creation of topological phases in two dimensions [22]. Examples of direct-write waveguide array structures relevant for these problems include rings, hexagonal lattices, X-shapes and triangular shapes [23–25]. To date, however, these have only been explored with classical light inputs, and specifically in the context of 2D quantum walks in [25]. True quantum effects, and genuine efficiency improvements in emulating quantum systems, will only emerge for non-classical input states as pointed out (for discrete-time walks) in [26]. The first such walk in the continuous regime was recently demonstrated in a linear waveguide array with two-photon inputs in [27].

Here, we study multi-walker continuous-time 2D quantum walks in an optical chip containing an elliptical arrangement of coupled direct-write waveguides. We characterise the optical chip via coherent light tomography, effectively realising single particle walks, and use the results to predict correlations for non-classical two-photon walks which we compare with experimental observations. Our work is an important step towards the emulation of quantum systems in three-dimensional integrated photonic architectures.

6.2 Device Description

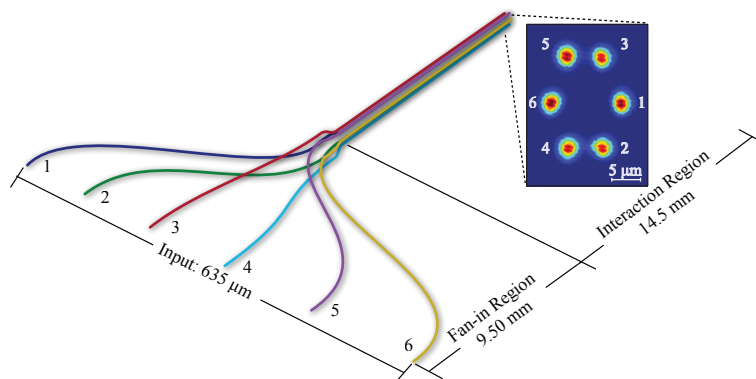


Figure 6.1: Schematic of the integrated waveguide circuit (drawing not-to-scale) and associated output. At the input the waveguides are equally spaced by $127 \mu\text{m}$. They then converge via a two-stage fan-in to their eventual elliptical configuration. The inset is a CCD image of the output: the waveguides are arranged with equal angular spacing around an ellipse with semi-major and semi-minor radii of 10.2 and $7.0 \mu\text{m}$ respectively.

The circuit for the quantum walk, shown in figure 6.1, consists of six waveguides written into a chip of high-purity fused silica using an ultrafast direct-write technique, described in detail in [19]. In this technique, femtosecond Ti:Sapphire laser pulses tightly focused

inside the sample yield localized refractive index modifications. The sample is translated in all dimensions to create true three dimensional curved waveguides, a process that cannot be replicated by conventional lithographic techniques. Our chip was written with a 1 kHz repetition rate, 800 nm, 120 fs laser, passed through a 520 μm slit and focused with a 40x0.6 NA microscope objective. The maximum refractive index difference between the waveguides and the substrate is approximately $\Delta n \sim 0.0062$.

At the input, the six waveguides are arranged in a line with equal spacing of 127 μm , allowing each waveguide to be addressed individually and simultaneously. The waveguides converge via a two-stage fan-in to their final configuration as shown in figure 6.1. In the primary fan-in stage, which occupies the first ~ 8.5 mm of the chip, the waveguides follow S-bend curves from a linear input arrangement to an elliptical configuration twice as large in radius as their final configuration. In the second fan-in stage, during the next 1 mm, further S-bends shrink this ellipse to have a semi-major axis of 10.2 μm and semi-minor axis of 7.0 μm . Studying an elliptical array provides additional insights into the coupling between waveguides as this shape breaks the degeneracy of the inter-waveguide distance. All the S-bends are of the ‘raised-sine’ form which has been shown to minimise bend loss [28], while the two-stage fan-in configuration was designed to minimise coupling (in particular, *asymmetrical* coupling) between waveguides before they attain their final interaction configuration.

The light evolution in this array is governed by the evanescent inter-waveguide coupling which drops off exponentially as a function of the waveguide distance. As an approximation, it can be described by a coupled-oscillator Hamiltonian. The corresponding theory and estimates for the inter-waveguide coupling constants are given in the appendix; notably some of the next-nearest-neighbour and even next-next-nearest-neighbour couplings are non-negligible over the interaction length in the chip.

6.3 Optical chip characterisation

The experimental setup is shown in figure 6.2. Light was coupled into the chip via a V-groove array, which houses six single-mode optical fibres on a line, matching the input spacing of the circuit waveguides. We first illuminated individual waveguides in the chip using coherent light from an 820 nm laser diode, see figure 6.2a). The output intensity profiles were processed in Matlab and converted into probability distributions. When compared to the numerical simulation obtained with the software suite, used to design the chip, the predicted and observed distributions at the circuit output differed significantly, see figure 6.3. This

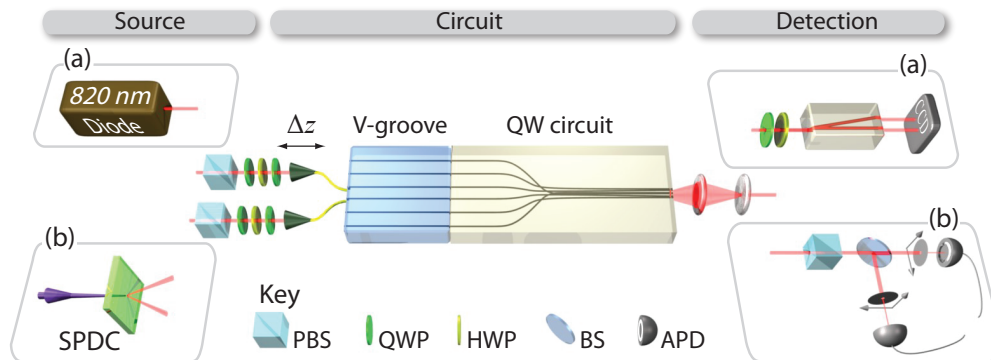


Figure 6.2: Experimental setup. The chip can be addressed with 6 individual single mode fibres. The input light polarisation is set by a combination of half- and quarter-wave plates (HWP, QWP) and polarising beamsplitters (PBS). The chip output is magnified and then collimated with two spherical lenses. (a) The chip was characterised with an 820 nm laser diode, imaged onto a CCD camera via a polarising prism. (b) Quantum walks were performed with two-photon inputs created via spontaneous parametric downconversion (SPDC). The relative delay Δz between the two input photons was adjusted using a translation stage. We used a 50/50 beamsplitter (BS) and two $\sim 500 \mu\text{m}$ apertures to select a combination of output ports and measure the two-photon correlations in coincidence using single-photon avalanche diodes.

behaviour prompted us to empirically determine the full optical response of the circuit using, polarisation-sensitive, coherent light tomography.

For this tomography the input polarisation was set using a bare reference fibre on top of the chip.¹ Into each waveguide we input the following set of polarisation states: $\{|H\rangle, |V\rangle, |D\rangle, |A\rangle, |L\rangle, |R\rangle\}$, where $|H\rangle$ and $|V\rangle$ represent horizontal and vertical polarisation and $|D/A\rangle = (|H\rangle \pm |V\rangle)/\sqrt{2}$, $|L/R\rangle = (|H\rangle \pm i|V\rangle)/\sqrt{2}$. For each output we measured the same six polarisation components, obtaining a total of 216 CCD images.

Using output intensity distributions taken from these images, we subsequently reconstructed an array of 36 Mueller matrices \mathcal{M} [29]. This array completely characterises the optical response of the circuit, quantifying the effects of three distinct processes: notably

¹The use of this reference fibre may have been insufficiently clear in the original publication; this footnote has been added to the thesis to clarify. The reference fibre was a piece of bare single-mode fiber precisely as long as the chip which was secured in place on top of the glass circuit. Its purpose was to allow the polarisation of the input light to be set precisely using fibre polarisation adjusters ('bat-ears') despite the birefringence of the waveguides. To accomplish this, the sample would be translated downwards slightly and the input light coupled into the bare fiber; the output from this fibre would then have a nearly identical spatial beam profile to the circuit output before the translation. The fibre polarisation controllers could then be used along with the polarising prism at the output in order to optimise the input polarisation, before translating the glass circuit back into place.

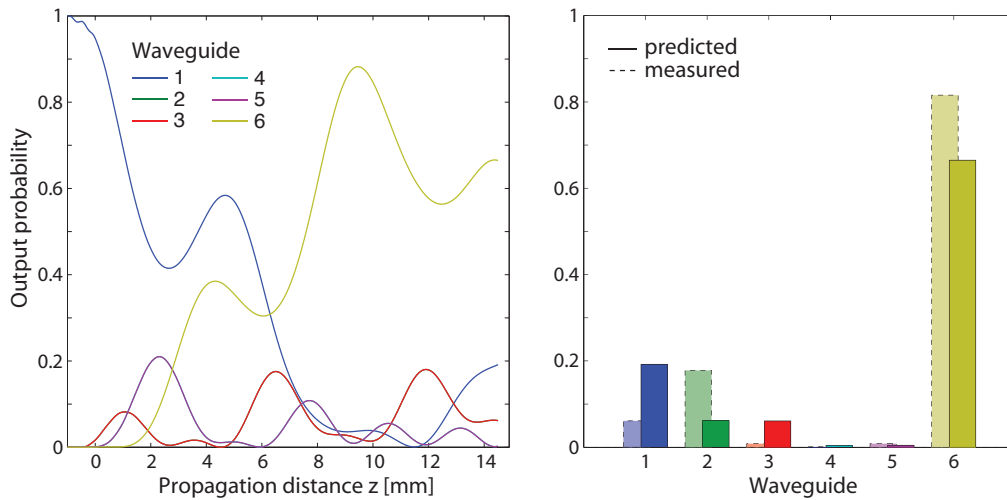


Figure 6.3: Comparison of numerical simulations and observed probability distributions for the optical chip in figure 6.1. (a) The propagation dynamics predicted using optical waveguide simulation software (see Appendix) with light input into waveguide 1, as a function of z . The simulation includes modelling of inter-waveguide coupling during the 1 mm second fan-in stage at $z \leq 0$. The curves for waveguides 2 and 3, and 4 and 5 overlap due to symmetry. (b) The predicted distribution at the output of the circuit, and the corresponding observed probabilities. The asymmetry in the measured distribution indicates that the optical response of the chip is not scalar, instead suggesting some vectorial behaviour. This was confirmed by further tomographic analysis.

polarisation-dependent inter-waveguide coupling, birefringence, and polarisation-dependent loss [29].

The results indicate strong birefringence in each of the six waveguides. Most notably, when the state $|H\rangle$ is input into waveguide 5, 30% of the overall output state across the six channels is rotated to $|V\rangle$. For the input channels 1, 2 and 4, the overall polarisation rotation was small, with more than 96% of $|H\rangle$ being retained at the output. Furthermore, there was significant polarisation-dependent coupling between the waveguides for all input channels. For instance, for input $|H\rangle$ into waveguide 1, 75% of the total output intensity was observed in channel 6, however when the input state was $|V\rangle$, only 10% of the total output intensity was contained in this channel. An exemplary selection of Mueller matrices, illustrated on Poincaré spheres and quantifying these effects is shown in figure 6.4. The full matrix array \mathcal{M} can be found in the Appendix.

In addition, the whole chip exhibited significant polarisation dependent loss; integrating over all output channels, we observed an excess 17% loss of $|V\rangle$ compared to $|H\rangle$ for waveguide 6. This may be due to a combination of absorption into the bulk of the circuit, or polarisation

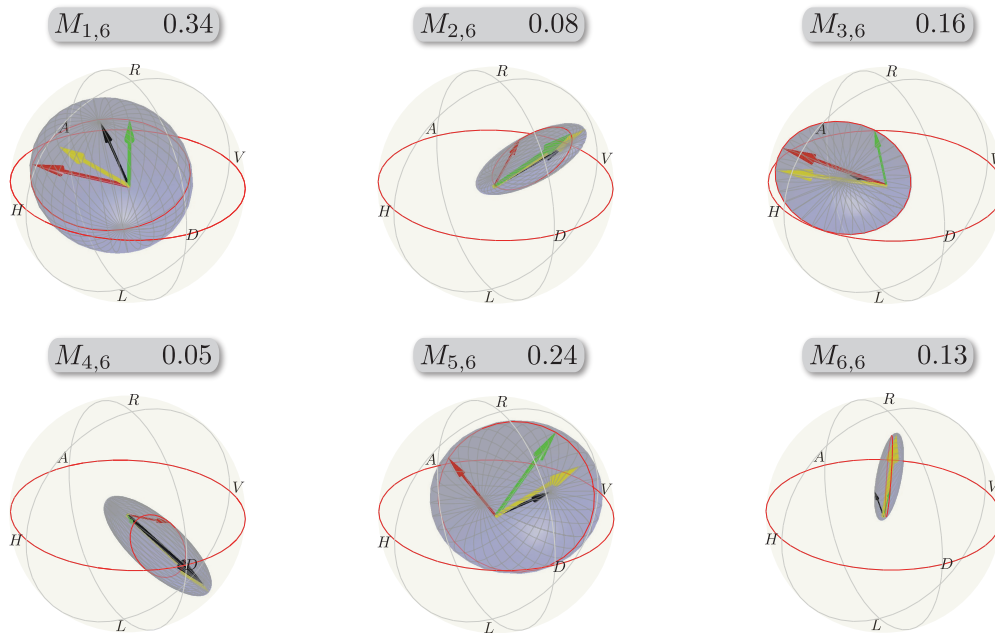


Figure 6.4: Poincaré sphere representation of the corresponding Mueller matrices, $M_{out,in}$ (see Appendix) describing the transformation from input waveguide 6 to outputs 1 – 6. Input states shown on the outer Poincaré spheres are mapped to different locations on the blue ellipsoids, simultaneously showing polarisation-dependent coupling and birefringent effects in the respective channel. The relative orientation of the ellipsoids is indicated by the set of orthogonal states $|H\rangle$ (red arrow), $|D\rangle$ (green arrow) and $|R\rangle$ (black arrow), and the point of contact between sphere and ellipsoid is indicated by the yellow arrow. Note that the arrow lengths are proportional to output power, *not* degree of polarisation. The numbers above each sphere give the normalised average power coupled into the respective channel.

dependence of the input coupling efficiency from the V-groove array to the chip, or both.

6.4 Two-photon walks

The coherent-light tomography encompasses all possible single-photon walks in this chip, since a single photon shares the coherence properties of a coherent light beam. However, these walks can be efficiently simulated classically and it is not until we input multi-photon states that we observe quantum effects [26].

A schematic of the setup for the two-photon walk experiment is shown in figure 6.2b). Pairs of single photons are created via spontaneous parametric down-conversion: a mode-locked 76 MHz laser centred at 820 nm is frequency doubled to 410 nm and focused into a

2 mm long β -barium borate (BBO) crystal, phase-matched for type-I downconversion. After passing through interference filters at 820 ± 2.5 nm, the degenerate photon pairs are coupled into single-mode fibres equipped with manual polarisation controllers. Photons are coupled into the chip via the V-groove fibre array.

We created photon pairs at a rate of 180 kHz, of which we detected a total of 6.5 kHz at the circuit output. The single-photon loss is thus $\sim 73\%$, factoring out the 50/50 beamsplitter, which reduces the number of coincidences by 50%. The main loss contributions stemmed from the poor input coupling efficiency between the V-groove array and the chip ($\sim 31\%$). The imperfect coupling is mostly due to a slight mismatch between the spacing of the fibres in the V-groove array and the locations of the input ports of the circuit. Intrinsic waveguide loss was negligible in comparison. The observed loss could be significantly reduced by using a more sophisticated imaging system.

We carried out two-photon quantum walks in two separate scenarios: with temporally distinguishable and indistinguishable photons. When the photons entering the chip are temporally distinguishable, i.e. with a time delay larger than their respective coherence times, they perform independent quantum walks with local evolution. When they enter the chip simultaneously, $\Delta z = 0$, they experience non-classical two-photon interference [30], yielding quantum dynamics, including the generation of two-photon entanglement. The theoretic qualitative difference between these two cases is described in the Appendix. Figure 6.5 shows an exemplary calibration scan of coincidence counts as a function of temporal delay. The signature of indistinguishable quantum walkers manifests as a dip in the rate of coincident detection events, C , at zero delay, with an interference visibility of $\mathcal{V} = (C_{\max} - C_{\min})/C_{\max}$ of $38 \pm 2\%$.

The results for two-photon quantum walks for distinguishable and indistinguishable photons input into the *nearest*-neighbour channels 1 and 2 are shown in figure 6.6a), as the normalised coincidence probability distributions, Γ^d and Γ^i respectively. Distinct differences are observed between the two cases, as suggested by the strong two-photon interference signature in figure 6.5.

The measured distributions are compared with predictions, figure 6.6b), which are based on determining the components of the waveguide array unitary U , for a particular input polarisation, see Appendix for details. The generalised overlap fidelities S , defined in the Appendix, between our measurements and predictions are $S^d = 93.4 \pm 0.3\%$ for the distinguishable walkers, and $S^i = 91.6 \pm 0.4\%$ for the indistinguishable walkers.

Figure 6.7a) shows correlation matrices for inputs 2 and 4 as an example of two-photon

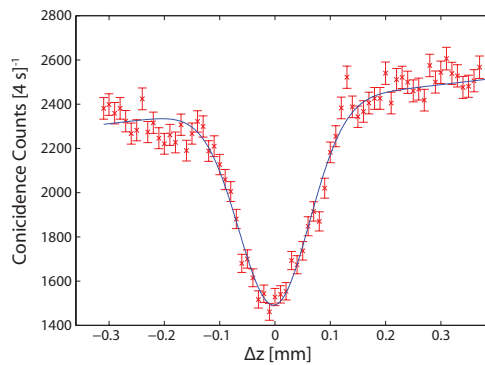


Figure 6.5: Example of observed two-photon interference between output waveguides 2 and 6 as a function of relative path difference between photon pairs input into neighbouring waveguides 1 and 2. The visibility of the dip is $\mathcal{V}_{2,6} = 38 \pm 2\%$, calculated from a Gaussian fit (blue line).

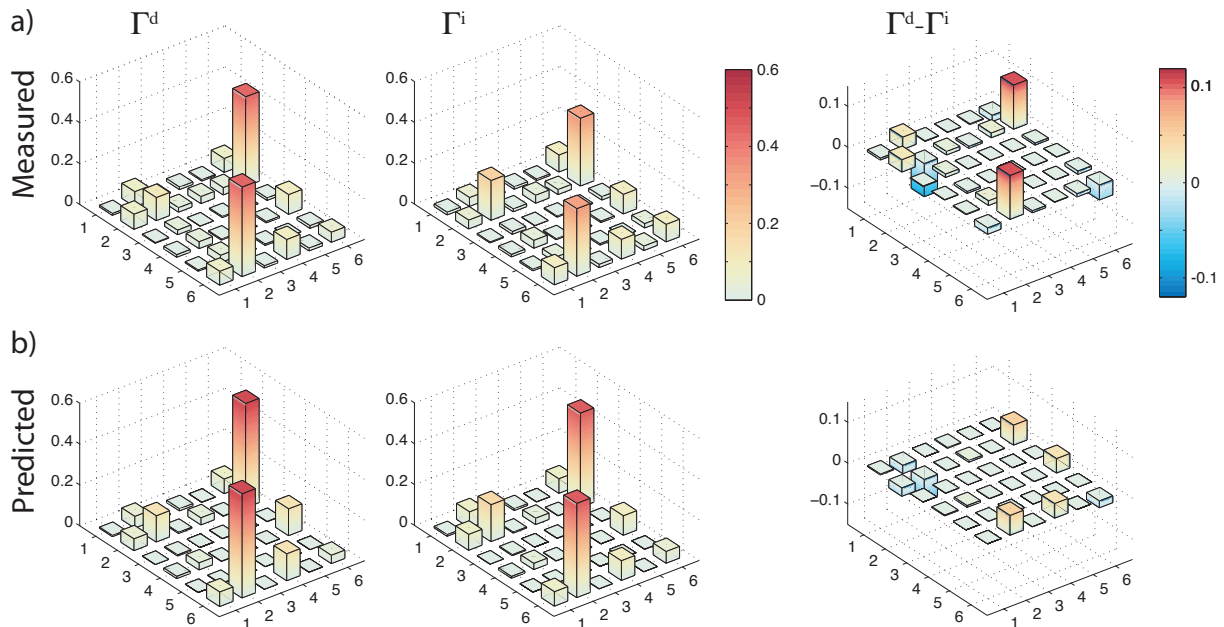


Figure 6.6: Correlation matrices for nearest-neighbour input channels 1 and 2. We recorded the photon-coincidence counts at each of the 36 pairs of output channels in a 20 second time-window. (a) The measured and (b) predicted correlation matrices for (left) temporally distinguishable photon pairs Γ^d , (center) temporally indistinguishable simultaneous walkers Γ^i , and (right) the difference $\Gamma^d - \Gamma^i$. The coincidence probability at the outputs 2 and 6 between the two plots reflects the two-photon interference dip shown in figure 6.5. The measured uncertainties are not plotted, as they are too small to be seen on the plots.

walks with *next*-nearest neighbour input ports. We again observe non-classical interference signatures, with visibilities up to $\mathcal{V}_{2,4} = 28 \pm 3\%$. The fidelities between the measured two-

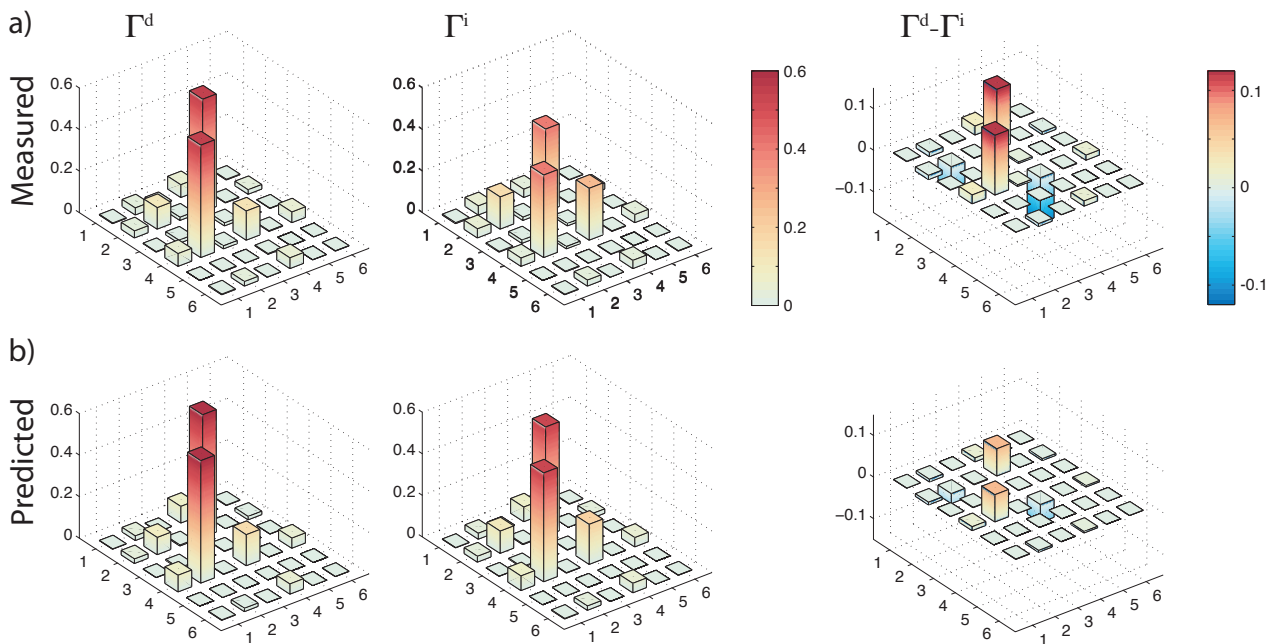


Figure 6.7: Correlation matrices for next-nearest neighbour input channels 2 and 4. The plots follow the same convention as those in figure 6.6, for both (a) the measured and (b) predicted correlation matrices. Uncertainties are again too small to be seen on the graphs.

photon matrices and their corresponding predictions, figure 6.7b), are $S^d = 97.9 \pm 1\%$, and $S^i = 96.2 \pm 0.8\%$.

6.5 Discussion

In conclusion, we have performed the first quantum walk in a three-dimensional waveguide structure with genuine non-classical inputs. This is a significant step towards emulating Hamiltonians which can be approximated by evanescently coupled waveguides. However, we have also identified a number of obstacles which must be addressed before such an approach can be fully realised.

First, despite the apparent good agreement between our predictions and the observed two-photon probability distributions, the two-photon visibilities—which quantify the measured non-classical effects—matched the predictions poorly. This is because the Mueller-matrix array derived from the coherent beam intensities only yields the squared absolute values of the elements of the system’s unitary U ; it does not determine the (generally complex) phase relations of the waveguide array. These phase factors could in principle be obtained by phase-sensitive coherent light tomography, as proposed in [25, 31]. An alternative technique [32]

requires a single N -photon input state (in this case $N = 6$) and photon-number resolved detection at each output. However, generating Fock states is hard and both techniques suffer from the large number of measurements required to fully characterise the six-port system. This is a perennial problem in quantum science: the exponential power granted by multi-photon walks on big lattices makes it hard to experimentally characterise system dynamics. A potential solution might be to use compressive sensing techniques, which have recently been exploited for exponentially efficient quantum process tomography [33].

Second, while we observed significant two-photon interference visibilities, the resulting probability distributions did not exhibit a conclusively quantum signature, as quantified by the witness defined in [16]. This was most likely due to the significant polarisation-dependent coupling and loss in the circuit, leading to non-unitary evolution which failed to preserve the coherence of the input quantum state. With a better understanding of the origins and mechanisms of these effects, they could be exploited to engineer devices such as polarisation-dependent couplers. It should be noted that these effects are certainly not inherent to the direct-write technique, as for example demonstrated by [34].

Future research should also focus on realising decoherence in continuous-time walks. Many physical, biological or chemical systems are strongly coupled to their environment and decoherence has been suggested to be the driving factor behind phenomena such as environmentally-assisted quantum transport [9]. While decoherence has been studied in discrete-time experiments [14], techniques for controllably introducing it to inherently robust waveguide lattices have yet to be demonstrated.

The emulation of classically intractable physics requires the scaling up to larger, more elaborate waveguide structures, which is certainly feasible, as demonstrated by [23–25]. However, it will be tricky to address the individual modes in these systems as the fan-in we demonstrate in our paper has its limitations. The theory will also have to catch up; unlike for quantum computation, there are no known fault-tolerance or error-correction techniques for quantum emulation in quantum walks.

Acknowledgments

We thank I. Kassal, B. P. Lanyon, G. G. Gillett, J. C. F. Matthews and J. L. O’Brien for valuable assistance. We acknowledge financial support by Australian Research Council Centres of Excellence, Discovery and Federation Fellow programs and an IARPA-funded US Army Research Office contract.

6.6 Appendix

In the Heisenberg picture, a light field input into a waveguide in this chip is subject to the coupled-oscillator Hamiltonian [16]

$$H = \sum_{i=1}^6 \beta_i a_i^\dagger a_i + \sum_{i,j=1}^6 C_{i,j} a_i^\dagger a_j, \quad (6.1)$$

where β_i is the propagation constant in waveguide i and $C_{i,j}$ is the coupling constant between waveguides i and j . The system then evolves in time according to the unitary operator $U(t) = e^{-iHt/\hbar}$ and the creation operators a_i^\dagger are subject to the Heisenberg equation of motion

$$\frac{\partial a_i^\dagger}{\partial z} = \frac{n}{c} \frac{\partial a_i^\dagger}{\partial t} = i [H, a_i^\dagger] = i\beta_i a_i^\dagger + i \sum_{j=1}^6 C_{i,j} a_j^\dagger, \quad (6.2)$$

which has the solution

$$a_i^\dagger(z) = \sum_j (e^{izC})_{i,j} a_j^\dagger(0) = \sum_j U_{i,j}(z) a_j^\dagger(0), \quad (6.3)$$

where $C = \{C_{i,j}\}$ is the 6×6 matrix of coupling constants with diagonal entries $C_{i,i} = \beta$, and z is the propagation distance along the waveguide array. Note that this evolution is equivalent to the continuous-time quantum walk formalism [15].

The interaction length z of the waveguides is chosen to match the desired run time t for the emulation of the Hamiltonian. The overall response of the circuit as a 12-port beam-splitting device is then contained in the unitary matrix $U = e^{izC}$, and we can define a set of six output creation operators b_i^\dagger , with $b_i^\dagger = a_i^\dagger(z) = \sum_j U_{i,j} a_j^\dagger$ for the input operators $a_j = a_j(0)$.

The coupling $C_{i,j}$ between two waveguides falls off exponentially with waveguide separation $r_{i,j}$ [23], so to design an array of the type discussed in this paper, the number of waveguides, their geometry, and their separations $r_{i,j}$ are chosen to reflect the properties of the Hamiltonian under investigation. This determines the parameters β_i and $C_{i,j}$. An interaction length z is chosen according to the desired emulation time t .

To translate the theoretical design into a real experimental system, the geometry of the circuit is analysed in a numerical electromagnetic design suite, in our case *RSoft* [35]. This program uses finite-difference algorithms to find solutions to Maxwell's equations in dielectrics and can be used to optimise a set of physical parameters (core diameter and refractive index

contrast) which will approximate the desired evolution. This provides the link between the Hamiltonian evolution of the quantum system under study, and the physical properties of the experimental system. For our chip, simulation predicts two leading nearest-neighbour coupling strengths of $C_{24} = 0.963 \text{ mm}^{-1}$ and $C_{12} = 0.312 \text{ mm}^{-1}$, reflecting the elliptical geometry. The next-nearest neighbour and further coupling values are $C_{14} = 0.050 \text{ mm}^{-1}$, $C_{16} = 0.044 \text{ mm}^{-1}$, $C_{23} = 0.009 \text{ mm}^{-1}$, $C_{25} = 0.005 \text{ mm}^{-1}$. The latter two are negligible: our model predicts that, in the absence of the other waveguides, less than 2% of light input into one waveguide of either of these pairs would couple to the other waveguide over the interaction length of the chip. However, the next-nearest neighbour coupling C_{14} and even the next-next-nearest neighbour coupling C_{16} are notably *non-negligible*, respectively leading to modeled values of 40% and 33% coupling between these waveguide pairs, in the absence of all other waveguides, over the interaction length of the chip.

We now describe the two-photon evolution in the optical system. Two temporally-indistinguishable input photons $|\Psi\rangle = a_i^\dagger a_j^\dagger |0\rangle$, for $i \neq j$, give the joint detection probability $\Gamma_{k,l}^i$ of finding the state $b_k^\dagger b_l^\dagger |0\rangle$ in output modes k and l [16]:

$$\Gamma_{k,l}^i = \langle b_l^\dagger b_k^\dagger b_k b_l \rangle_\Psi = \frac{1}{1 + \delta_{k,l}} |U_{i,k} U_{j,l} + U_{j,k} U_{i,l}|^2. \quad (6.4)$$

The matrix $\Gamma^i = \{\Gamma_{k,l}^i\}$ then describes the two-photon probability distributions in all combinations of output modes. In contrast, two distinguishable photons will evolve independently and obey the statistics of Bernoulli trials. The corresponding output probability distribution $\Gamma_{k,l}^d$ takes the form,

$$\Gamma_{k,l}^d = \frac{1}{1 + \delta_{k,l}} (|U_{i,k} U_{j,l}|^2 + |U_{i,l} U_{j,k}|^2). \quad (6.5)$$

In the case of photons and electro-magnetic fields, $\Gamma_{k,l}^d$ represents an intensity correlation matrix $\Gamma_{k,l}^d = \langle I_k I_l \rangle$. The components $\Gamma_{k,l}^i$ and $\Gamma_{k,l}^d$ will differ by the factor $2 \text{Re} [(U_{i,k} U_{j,l})^* (U_{i,l} U_{j,k})]$, which encompasses the quantum nature of indistinguishable walkers.

To quantify the overlap fidelity between two probability distributions, we use [27]:

$$S = \left(\sum_{k,l} \sqrt{\Gamma_{k,l} \Gamma_{k,l}^p} \right)^2 / \sum_{k,l} \Gamma_{k,l} \sum_{k,l} \Gamma_{k,l}^p. \quad (6.6)$$

Mueller matrix

The Mueller-matrix array \mathcal{M} describes the transfer properties of the circuit in terms of the Stokes parameters \mathcal{S} , which describe the polarisation state of an electromagnetic field [29].

The component $M_{i,j}$ is the 4×4 Mueller matrix describing the coupling from input waveguide j to output waveguide i . From the corresponding output Stokes parameter $\mathcal{S}_{i,j}$ for the input state $|H\rangle_j$, the real-valued parameter $|U_{i,j}|^2$ was calculated as the output transmission component in the $|H\rangle_i$ subspace.

Table 1 shows the calculated Mueller-matrix array \mathcal{M} of the quantum walk circuit. The matrix not only allows us to determine the evolution matrix U in the $|H\rangle$ subspace, but also quantifies the polarisation-dependent coupling and birefringence observed in the circuit, as seen in figure 6.4.

$$\{\mathcal{M}\} = \begin{pmatrix} M_{1,1} & \cdots & M_{1,6} \\ \vdots & \ddots & \vdots \\ M_{6,1} & \cdots & M_{6,6} \end{pmatrix} = 10^{-2} \times$$

24.51	-18.83	-4.89	-2.32	8.39	1.52	2.15	0.92	19.34	-1.06	3.41	-4.45	3.03	-1.47	4.15	2.16	8.89	2.42	-2.92	-1.04	33.34	9.02	1.30	-1.14
-20.16	26.22	2.81	-2.77	1.66	6.64	3.11	5.72	0.27	5.64	-16.31	-15.85	3.07	-1.64	4.31	1.80	3.27	0.32	-8.98	0.25	10.62	36.67	-3.52	-13.98
2.42	-3.57	8.18	-19.65	-0.35	3.54	-7.40	0.01	3.63	-18.81	4.39	-11.81	1.49	-0.49	2.46	1.69	-1.63	-8.39	0.23	-3.15	-0.45	-12.27	10.14	-33.96
-7.69	5.84	21.04	9.23	0.89	5.15	2.64	-6.68	5.19	11.15	16.31	-14.00	-0.70	0.86	-0.42	-0.72	2.83	3.86	-1.24	-8.62	6.28	8.66	34.62	9.51
16.20	4.05	3.97	2.57	43.89	21.91	-11.33	3.46	2.69	2.63	1.37	-0.38	23.82	-11.27	2.26	1.56	7.13	-5.66	3.46	-2.27	7.89	0.03	7.76	4.62
1.88	15.38	-5.17	-4.88	26.78	42.58	-19.28	9.28	-1.81	-1.79	-1.57	-0.91	-13.09	24.40	-12.65	-0.47	-6.69	7.22	-4.32	1.69	-4.97	-0.03	-4.85	-6.14
3.64	4.86	-2.57	16.12	4.13	-13.57	-38.63	1.57	-1.40	-1.46	1.15	-0.54	-5.41	12.05	17.15	-6.03	1.57	-1.14	-0.03	-6.36	3.84	-3.29	4.81	1.30
-5.42	-7.03	-16.81	-2.59	3.99	9.54	-3.60	-40.51	2.44	2.47	1.25	-1.82	0.02	4.93	3.60	21.42	-1.27	2.74	4.66	-0.22	5.71	2.44	6.35	2.06
7.77	-6.72	-1.85	-5.82	0.37	-0.32	0.10	-0.11	43.51	1.17	-13.56	19.12	5.48	-4.18	2.03	-4.22	27.90	3.29	11.18	-14.72	16.01	8.96	-4.68	-3.37
-0.55	1.04	-3.43	0.26	-0.07	0.05	-0.14	-0.24	5.88	40.78	13.23	19.07	-4.83	4.86	-3.51	3.38	-1.40	-19.32	-6.63	-3.16	11.26	13.02	-9.70	-8.71
-6.18	5.17	1.57	6.45	0.26	-0.29	0.14	-0.25	5.52	21.04	-38.14	-18.28	2.91	-2.95	-2.07	-3.76	10.11	-5.61	21.89	-2.05	-4.27	-11.34	-0.86	-11.26
5.58	-5.97	-1.68	-2.97	-0.24	0.28	0.12	-0.00	-24.37	7.09	31.72	-44.65	-0.16	1.61	2.32	-3.66	21.39	6.04	6.75	-27.47	2.42	6.42	12.54	-6.51
9.13	-9.07	1.64	0.46	35.91	-17.89	6.16	0.90	0.66	-0.46	0.22	0.26	52.33	27.32	-14.62	11.70	1.05	-0.75	0.21	0.11	4.50	-0.58	-2.19	5.25
-9.79	9.85	-2.04	-0.60	-20.32	37.74	-3.79	-7.64	-0.33	0.33	-0.71	-0.21	35.12	48.38	-10.62	27.49	-0.72	0.88	-0.62	-0.33	-1.46	-1.52	2.65	-2.40
-1.75	1.73	-0.06	0.37	-1.21	9.61	9.90	30.06	0.36	-0.62	-0.04	-0.38	6.50	-19.53	-33.03	24.30	-0.02	-0.00	0.40	-1.08	3.91	-0.23	-0.60	4.86
2.23	-2.25	0.35	0.38	-5.57	2.85	-32.32	8.80	-0.27	0.29	0.21	-0.60	11.26	16.57	-30.93	-30.44	-0.51	0.80	0.68	0.30	-1.99	2.33	2.64	-2.59
0.81	0.17	1.37	1.28	0.02	-0.00	-0.00	-0.00	27.88	-1.34	12.54	-12.09	2.38	-2.36	-1.46	-0.14	45.71	-0.87	-2.85	18.66	23.42	-3.77	6.29	-0.21
-0.55	0.15	-1.22	-1.06	-0.01	0.00	0.01	0.00	-1.19	-10.62	13.42	19.06	2.05	-2.07	-0.05	-0.55	11.35	37.49	0.79	29.00	-5.40	12.39	-13.28	-20.14
-0.58	-0.43	-1.09	-1.11	-0.02	0.00	-0.00	-0.00	6.81	21.63	15.27	0.45	-1.33	1.32	1.62	0.62	-1.24	9.25	-45.50	-11.73	4.17	-22.51	1.89	-12.93
0.09	0.11	0.40	-0.27	-0.01	0.00	-0.00	0.00	21.23	-8.06	20.64	-24.46	-1.40	1.39	0.95	-1.49	-19.88	25.77	18.00	-42.56	6.30	7.07	21.99	-9.18
41.59	30.40	-0.25	3.82	11.42	-5.21	2.92	-5.18	5.93	-0.95	-3.98	-2.46	12.96	-8.03	7.64	-11.06	9.32	1.58	-9.08	-0.74	14.85	-13.66	-8.48	-5.15
31.67	42.04	-11.93	-4.82	-6.88	11.51	-2.00	4.74	-0.29	5.78	-1.68	0.67	-10.87	8.56	-5.01	10.10	1.39	4.01	-1.05	6.22	-9.80	8.68	5.70	6.84
15.52	18.13	18.27	29.85	0.92	1.55	-7.65	-8.68	3.44	-0.41	-4.24	-5.92	9.70	-4.73	7.89	-9.01	-7.07	-3.77	9.20	3.09	-14.07	13.53	8.84	3.71
-1.09	-7.70	-31.63	21.38	2.74	1.48	9.46	-7.52	-1.65	1.94	5.68	-1.64	2.65	-3.25	3.25	0.66	4.06	-3.80	-6.50	1.95	2.32	-3.04	2.93	-1.34

Table 6.1: Array \mathcal{M} of 36 Mueller matrices, obtained from polarisation-sensitive, coherent-light tomography.

This array fully describes the classical optical response of the waveguide array.

References

- [1] Feynman, R. Simulating physics with computers. *Int. J. Theor. Phys.* **21**, 467–488 (1982). 92
- [2] Lanyon, B. P. *et al.* Towards quantum chemistry on a quantum computer. *Nature Chem.* **2**, 106–111 (2010). 92
- [3] Du, J. *et al.* NMR implementation of a molecular hydrogen quantum simulation with adiabatic state preparation. *Phys. Rev. Lett.* **104**, 030502 (2010). 92
- [4] Lloyd, S. Universal quantum simulators. *Science* **273**, 1073–1078 (1996). 92
- [5] Aharonov, Y., Davidovich, L. & Zagury, N. Quantum random walks. *Phys. Rev. A* **48**, 1687 (1993). 92
- [6] Kempe, J. Quantum random walks: an introductory overview. *Contemp. Phys.* **44**, 307–327 (2003). 92
- [7] Mülken, O. & Blumen, A. Continuous-time quantum walks: Models for coherent transport on complex networks. *Phys. Rep.* **502**, 37–87 (2011). 92
- [8] Plenio, M. B. & Huelga, S. F. Dephasing-assisted transport: quantum networks and biomolecules. *New J. Phys* **10**, 113019 (2008). 92
- [9] Mohseni, M., Rebentrost, P., Lloyd, S. & Aspuru-Guzik, A. Environment-assisted quantum walks in photosynthetic energy transfer. *J. Chem. Phys.* **129**, 174106 (2008). 92, 101
- [10] Karski, M. *et al.* Quantum walk in position space with single optically trapped atoms. *Science* **325**, 174–177 (2009). 92
- [11] Zähringer, F. *et al.* Realization of a quantum walk with one and two trapped ions. *Phys. Rev. Lett.* **104**, 100503 (2010). 92
- [12] Schmitz, H. *et al.* Quantum walk of a trapped ion in phase space. *Phys. Rev. Lett.* **103**, 090504 (2009). 92
- [13] Schreiber, A. *et al.* Photons walking the line: A quantum walk with adjustable coin operations. *Phys. Rev. Lett.* **104**, 50502 (2010). 92

- [14] Broome, M. A. *et al.* Discrete single-photon quantum walks with tunable decoherence. *Phys. Rev. Lett.* **104**, 153602 (2010). [92](#), [101](#)
- [15] Farhi, E. & Gutmann, S. Quantum computation and decision trees. *Phys. Rev. A* **58**, 915–928 (1998). [92](#), [102](#)
- [16] Bromberg, Y., Lahini, Y., Morandotti, R. & Silberberg, Y. Quantum and classical correlations in waveguide lattices. *Phys. Rev. Lett.* **102**, 253904 (2009). [92](#), [101](#), [102](#), [103](#)
- [17] Davis, K. M., Miura, K., Sugimoto, N. & Hirao, K. Writing waveguides in glass with a femtosecond laser. *Opt. Lett.* **21**, 1729–1731 (1996). [92](#)
- [18] Nolte, S., Will, M., Burghoff, J. & a. Tünnemann. Femtosecond waveguide writing: a new avenue to three-dimensional integrated optics. *Appl. Phys. A* **77**, 109–111 (2003). [92](#)
- [19] Marshall, G. D. *et al.* Laser written waveguide photonic quantum circuits. *Opt. Express* **17**, 12546–12554 (2009). [92](#), [93](#)
- [20] Hein, B. & Tanner, G. Wave communication across regular lattices. *Phys. Rev. Lett.* **103**, 260501 (2009). [92](#)
- [21] Bulger, D., Freckleton, J. & Twamley, J. Position-dependent and cooperative quantum Parrondo walks. *New J. Phys* **10**, 093014 (2008). [93](#)
- [22] Kitagawa, T., Rudner, M., Berg, E. & Demler, E. Exploring topological phases with quantum walks. *Phys. Rev. A* **82**, 33429 (2010). [93](#)
- [23] Szameit, A., Dreisow, F., Pertsch, T., Nolte, S. & Tünnemann, A. Control of directional evanescent coupling in fs laser written waveguides. *Opt. Express* **15**, 1579–1587 (2007). [93](#), [101](#), [102](#)
- [24] Szameit, A. *et al.* Hexagonal waveguide arrays written with fs-laser pulses. *Appl. Phys. B* **82**, 507–512 (2006). [93](#), [101](#)
- [25] Keil, R. *et al.* Photon correlations in two-dimensional waveguide arrays and their classical estimate. *Phys. Rev. A* **81**, 23834 (2010). [93](#), [100](#), [101](#)
- [26] Rohde, P. P., Schreiber, A., Stefanak, M., Jex, I. & Silberhorn, C. Multi-walker discrete time quantum walks on arbitrary graphs, their properties and their photonic implementation. *New J. Phys* **13**, 013001 (2011). [93](#), [97](#)

- [27] Peruzzo, A. *et al.* Quantum walks of correlated photons. *Science* **329**, 1500 (2010). [93](#), [103](#)
- [28] Minford, W. J., Korotky, S. K. & Alferness, R. C. Low-loss ti:linbo₃ waveguide bends at $\lambda = 1.3 \mu\text{m}$. *IEEE Journal of Quantum Electronics* **QE-18**, 1802–1806 (1982). [94](#)
- [29] Hecht, E. & Zajac, A. Optics. *Addison-Wesley series in physics* (1974). [95](#), [96](#), [103](#)
- [30] Hong, C. K., Ou, Z. Y. & Mandel, L. Measurement of subpicosecond time intervals between two photons by interference. *Phys. Rev. Lett.* **59**, 2044–2046 (1987). [98](#)
- [31] Keil, R. *et al.* Classical characterization of biphoton correlation in waveguide lattices. *Phys. Rev. A* **83**, 013808 (2011). [100](#)
- [32] Pryde, G. J. & White, A. G. Creation of maximally entangled photon-number states using optical fiber multiports. *Phys. Rev. A* **68**, 052315 (2003). [100](#)
- [33] Shabani, A. *et al.* Efficient measurement of quantum dynamics via compressive sensing. *Phys. Rev. Lett.* **106**, 100401 (2011). [101](#)
- [34] Sansoni, L. *et al.* Polarization entangled state measurement on a chip. *Phys. Rev. Lett.* **105**, 200503 (2010). [101](#)
- [35] URL <http://www.rsoftdesign.com/>. [102](#)

Chapter 7

Simulating environmentally assisted quantum transport in integrated optics

7.1 Introduction

Energy harvesting and transport efficiency in studied photosynthetic systems is amazingly efficient. Experimental studies of photosynthetic light-harvesting complexes [1–4] have shown both near-unit energy transport efficiency and the presence of coherence in such systems. In combination with with theoretical modelling of nanoscale transport processes [5], this has inspired recent research into energy transport in quantum networks, in particular the effects of noise on transport efficiency. Surprisingly, environment-induced decohering noise sometimes enhances transport efficiency in certain quantum systems through suppression of coherent localizing effects.

Noise is generally thought to inhibit transport in classical systems. Furthermore quantum noise causes wavefunction collapse, and can lead to spatial localization through effective repeated measurement—the quantum Zeno effect—thus inhibiting transport. Static disorder in a quantum network can also lead to localization [6], potentially preventing energy from reaching spatially-separated regions. However, intermediate noise levels can—perhaps counterintuitively—enhance quantum transport efficiency by partially mitigating localizing coherent effects [7–13]. This phenomenon, known as decoherence-assisted transport [14, 15] or environmentally-assisted quantum transport (ENAQT) [16], has been the subject of many

theoretical studies but until now has never been directly observed. In addition to providing insight into photosynthetic processes, ENAQT has potential applications in engineering synthetic quantum transport systems *e.g.* for artificial light-harvesting, as well as in understanding dynamics in other quantum networks such as disordered spin chains.

Instead of studying the transport of molecular excitations in photosynthetic light-harvesting complexes consisting of networks of coupled chromophores in a noisy environment, here we use integrated photonics to implement the first laboratory simulations of ENAQT in a synthetic network of coupled waveguides. Our simulation is engineered to achieve a specific Hamiltonian, as well as measurable loss from a specific mode and dephasing simulated through bandwidth broadening. This is the first custom engineering of a non-trivial interaction Hamiltonian with controllable open-systems dynamics and thus represents a milestone for coherent and quantum photonic simulation.

Our simulators were fabricated using femtosecond laser direct writing, whereby waveguides are drawn directly into a glass sample using a focused pulsed laser. This allows for the creation of three-dimensional waveguide arrays, as well as precision and repeatability in engineering interactions [17].

This chapter presents an overview of the theory of ENAQT and details a method to simulate it using waveguide arrays, as well as results from two generations of photonic simulators. Our initial simulation demonstrates a transport enhancement of $7.2 \pm 2.4\%$ in the noisy case, with broadband illumination, over the narrowband case. However, this simulation was not completely satisfactory, as the waveguide fabrication procedure was insufficiently characterized for satisfactory modeling of our experiment to compare with our measured results. Additionally, even without complete circuit characterization we were able to note significant dissimilarities between the output distribution of this circuit in the noiseless case and the ideal distribution. Furthermore we concluded that our results would be improved by comparing the transport enhancement for different propagation lengths in the waveguide circuit in order to illuminate the time-dependence of ENAQT. For these reasons we created several iterations of second-generation simulation circuits, with better-characterized waveguides and multiple interaction lengths. Our study of these hopefully-improved circuits is ongoing, but encouraging preliminary results are presented here.

7.2 General theory of ENAQT

Consider a single excitation on a network of N lattice sites coupled via Coulomb interactions. Such a system is governed by a tight-binding Hamiltonian of the form

$$H = \sum_{m=1}^N \epsilon_m |m\rangle\langle m| + \sum_{n<m}^N V_{mn} (|m\rangle\langle n| + |n\rangle\langle m|), \quad (7.1)$$

where $|m\rangle$ denotes the excitation being localized at site m , ϵ_m the excitation energy for that site, and V_{mn} the coupling rate between sites m and n . Although ENAQT can occur on an ordered lattice where the energies ϵ_m are all the same [18], transport enhancement was first explained in the context of disordered systems, and we consider such a case here.

Typically an excitation is assumed to occur at a specific input site¹ and we are interested in the efficiency with which this excitation is transported to a target site $k \in \{1, \dots, N\}$ where it is trapped. In the case of a photosynthetic transport complex, as represented in figure 7.1a), the source would be an antenna complex which absorbs solar energy, yielding quantized molecular excitations (excitons), and the trap the input to a reaction center where such excitons start a chemical reaction. Trapping at the target site k can be modelled by irreversible coupling to a sink mode $s \notin \{1, \dots, N\}$ at a rate κ . Such a network is represented in figure 7.1b).

We are interested in the efficiency η of energy transport in such a network, defined as the probability $P_s(T) = \kappa \int_0^T \rho_{kk}(t) dt$ that the exciton is found in the sink mode s at a time $t = T$ after the initial excitation, where ρ is the system density operator in the site basis. ENAQT occurs when the trapping probability is increased over the noiseless case by some finite level of noise.

Inter-site coupling would typically be suppressed by energy mismatches between neighboring sites, ultimately diminishing the total energy trapped at the sink s in time T . Noise can mitigate such localising effects and enhance the transport efficiency η between the input and target sites. One explanation is illustrated schematically in figure 7.1c): local noise modulates individual site energies on a timescale faster than the transport process, sometimes bringing neighboring sites briefly into resonance and thus allowing improved coupling between them. In a different but ultimately equivalent formulation, the system eigenmodes which overlap with the input state may have no overlap with the trapping site k as a result of Anderson

¹Or possibly a superposition of nearby sites, but this is not the case simulated here.

localization [6], or of interference between different paths through the network from the input to the trap. Decohering noise then counteracts these coherent localization phenomena, allowing population transfer to system eigenmodes which better overlap with the trap site, thus yielding more efficient transport.

The first theoretical explorations of ENAQT focused on the case where the noise takes the form of site-independent, Markovian, pure dephasing [14, 16]; in this case the system master equation can be cast in Lindblad form using non-unitary Lindblad operators \mathcal{L} :

$$\dot{\rho} = -\frac{i}{\hbar} [H, \rho(t)] + \mathcal{L}_{\text{trap}}(\rho(t)) + \mathcal{L}_{\phi}(\rho(t)). \quad (7.2)$$

The trapping from site k into the sink is given by $\mathcal{L}_{\text{trap}}$:

$$\mathcal{L}_{\text{trap}} = 2\kappa \left(|s\rangle\langle k| \rho(t) |k\rangle\langle s| - \frac{1}{2} |k\rangle\langle k| \rho(t) - \frac{1}{2} \rho(t) |k\rangle\langle k| \right) \quad (7.3)$$

\mathcal{L}_{ϕ} describes pure dephasing which attenuates coherences between sites at rates γ_m :

$$\mathcal{L}_{\phi}(\rho(t)) = \sum_m \gamma_m \left(|m\rangle\langle m| \rho(t) |m\rangle\langle m| - \frac{1}{2} |m\rangle\langle m| \rho(t) - \frac{1}{2} \rho(t) |m\rangle\langle m| \right). \quad (7.4)$$

Under this noise model, in the absence of coupling the coherences in the density operator will decay exponentially, each at a site-dependent rate γ_m .

However, this exact noise model is not required for moderate decoherence to yield increased trapping efficiency; ENAQT under non-Markovian conditions has been studied in Refs. [20, 21]. Transport efficiency can be enhanced as long as the noise allows coupling between otherwise-orthogonal system eigenmodes to counteract coherent localization. Our target ENAQT simulation constitutes a special case chosen to maximise the measurable enhancement.

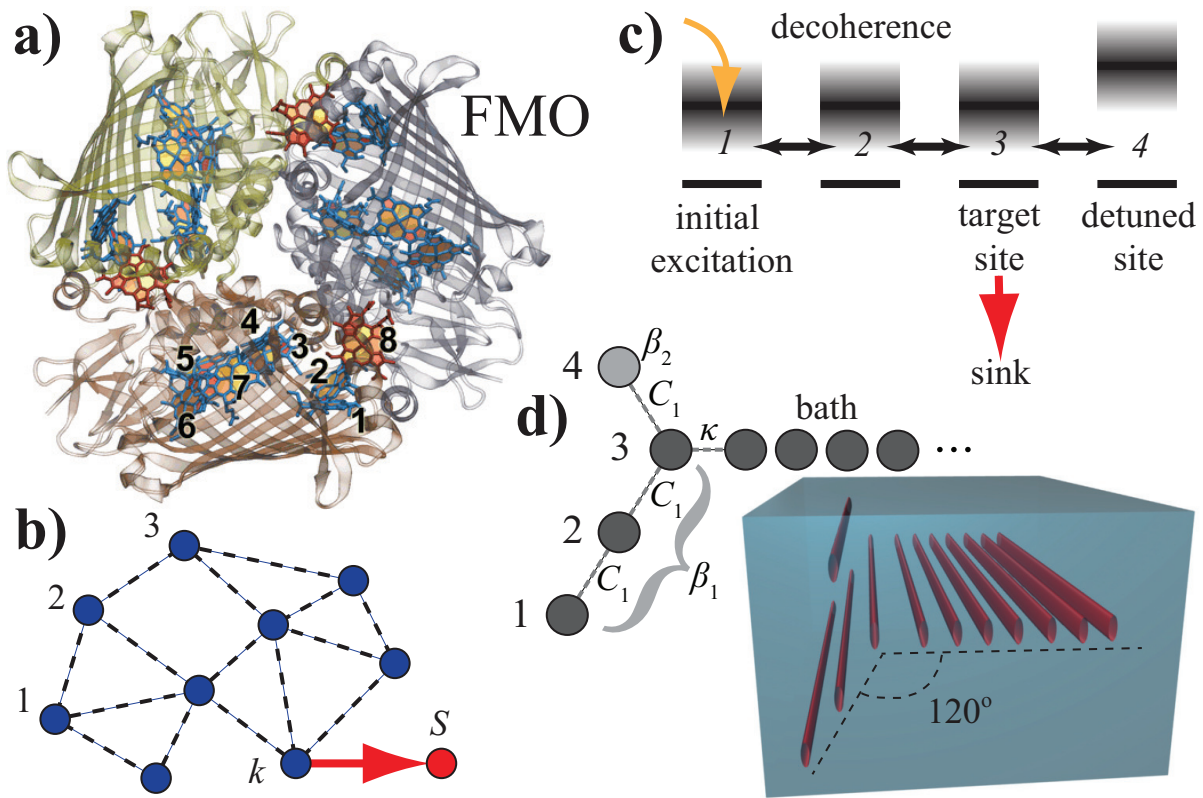


Figure 7.1: Describing and simulating environmentally-assisted quantum transport. a) Coherent 2D spectroscopy experiments suggest that coherence significantly affects exciton transport between coupled chromophores in the Fenna-Matthews-Olson (FMO) photosynthetic complex [1], represented schematically here with 8 labeled chromophores embedded in a protein matrix. Simulations suggest this transport is enhanced by dephasing noise at a rate consistent with room temperature thermal fluctuations [14, 16]. This figure is reproduced from [19]. b) A generalized framework for ENAQT consists of a lattice of N sites with some pair-wise couplings. The long-term efficiency of transport within the network to a target site $k \in \{1, \dots, N\}$ can sometimes be enhanced by noise; any excitation at this site is absorbed, modeled as coupling to a sink s . c) We simulate a specific instance of ENAQT which occurs on a lattice of size $N = 4$, initially excited at site 1 and with target site 3. Site 4 is energetically detuned so that one system eigenmode has no occupancy at the target site; decoherence improves coupling between sites 3 and 4, allowing all eigenmodes to couple to the bath and thus increasing transport efficiency. d) Our simulator consists of four coupled waveguides arranged as shown (end view). Each waveguide is coupled to its nearest neighbors with coupling constant C_1 ; waveguide 3 is additionally coupled at rate κ to a large bath of closely-coupled waveguides that effect transport away from the simulator, thus functioning as a sink. Waveguide 4 has propagation constant β_2 at the design wavelength while the others have propagation constant $\beta_1 = \beta_2 - C_1$. The inset represents the waveguide array realized in a glass substrate, and illustrates the ellipticity of the waveguides in our implementation, as well as the relative angles between them.

7.3 Waveguide implementation

To demonstrate ENAQT, we employ arrays of optical waveguides designed to simulate a tight-binding Hamiltonian and equation of motion for a single excitation in a coupled noisy network, as described in Eqs. (7.1, 7.2) above. The evolution of a photon in an array of N weakly-coupled single-mode waveguides is well-approximated by the equation

$$i \frac{\partial}{\partial z} a_m^\dagger(z) = \beta_m a_m^\dagger(z) + \sum_{n \neq m}^N C_{mn} a_n^\dagger(z), \quad (7.5)$$

where the light is propagating in the z -direction, $a_m^\dagger(z)$ is a creation operator for a photon in waveguide m at position z , and β_m and C_{mn} are respectively the propagation constants of the waveguides and the coupling constants between them. The former are determined by the waveguide refractive index spatial profiles, while the latter also depend on the separation of the two waveguides. The spatial evolution of light in the z -direction governed by this Schrödinger-like equation directly simulates the evolution of the Hamiltonian Eq. (7.1), with the inter-waveguide coupling constants C_{mn} taking the part of the inter-site couplings V_{mn} , and the propagation constants β_m acting as the site energies ϵ_m . Thus we can simulate different Hamiltonians by controlling the number, position, and refractive indices of waveguides in the arrays.

Our ENAQT simulation circuits each consist of four waveguide ‘sites’ which constitute the system, arranged as shown in figure 7.1d). Waveguide 1 is the input, and waveguide 3 the target. Loss from waveguide 3 is effected by coupling to a long ‘bath’ of tightly-coupled waveguides as shown in the figure and described in Refs. [22, 23]. The simulators have been designed to have waveguide propagation constants $\{\beta_m\}$ and separations among the system waveguides such that, at our central wavelength λ_0 , we approximate the Hamiltonian

$$\mathcal{H}(\lambda_0) = \begin{bmatrix} \beta_1 & C_1 & 0 & 0 \\ C_1 & \beta_1 & C_1 & 0 \\ 0 & C_1 & \beta_1 & C_1 \\ 0 & 0 & C_1 & \beta_1 + \Delta\beta \end{bmatrix}, \quad (7.6)$$

where C_{mn} is the coupling constant between waveguides m and $n \in \{1, \dots, 4\}$ and implicitly depends on their separation, while both β and C are implicitly dependent on wavelength λ . Direct coupling between non-neighboring sites is small due to their large separation with respect to the guided mode width. It is at most 5% of the coupling between neighboring system waveguides, and thus we neglect it in our analysis.

Our simulations are designed so that, at our central simulation wavelength λ_0 ,

$$\Delta\beta(\lambda_0) = C_1(\lambda_0). \quad (7.7)$$

In this case, one of the eigenstates of the Hamiltonian (7.6), with eigenvalue $(\beta_1 + \Delta\beta)$, has no support on waveguide 3:

$$|\psi_1\rangle = \frac{1}{\sqrt{3}}[-1, -1, 0, 1]. \quad (7.8)$$

The other eigenvectors are independent of the particular values chosen for β_1 and c_1 :

$$\begin{aligned} |\psi_2\rangle &= [0.2280, 0.4285, 0.5773, 0.6565] \\ |\psi_3\rangle &= [-0.4285, 0.6565, -0.5773, 0.2280] \\ |\psi_4\rangle &= [0.6565, -0.2280, -0.5773, 0.4285]. \end{aligned} \quad (7.9)$$

Ideally, the eigenstate $|\psi_1\rangle$ would therefore be unable to couple to the sink—at least for $\lambda = \lambda_0$ —and the maximum trapping efficiency given infinite time is thus $\eta = 2/3$, since as per Eq. (7.8) the input state has a $1/3$ overlap with $|\psi_1\rangle$.

We implement noise by broadening the illumination bandwidth. This will only yield measurable ENAQT if the condition in Eq. (7.7)—which ensures the existence of an eigenvector $|\psi_1\rangle$ with no support on the trapping waveguide—fails sufficiently fast with increasing spectral separation from the central illumination wavelength λ_0 . The propagation constant is just the effective wavenumber in the waveguide: $\beta(\lambda) = 2\pi n_{\text{eff}}(\lambda)/\lambda$, where the effective index n_{eff} depends on the waveguide shape but is primarily a function of the refractive index. Meanwhile the wavelength-dependence of the coupling constant $C_{ab}(\lambda)$ between two weakly-coupled single-mode waveguides a and b will be a complicated function of their separations and refractive index profiles, as illustrated in Fig. 7.7. However, modeling based on refractive index profiles achievable in laser-written waveguides suggests that the deviation $\Delta_{\mathcal{H}}(\lambda)$ from the condition for the Hamiltonian in Eq. (7.7) should decrease approximately linearly as a function of wavelength across our intended simulation bandwidth, with sufficient slope for measurable ENAQT, where

$$\Delta_{\mathcal{H}}(\lambda) = \Delta\beta(\lambda) - C_1(\lambda). \quad (7.10)$$

Further details concerning such modeling will be presented in Sec. 7.5.1. For increasing absolute values of $\Delta_{\mathcal{H}}$, eigenstate $|\psi_1\rangle$ will have increasing support on waveguide 3 and thus be better able to couple to the sink; the result of integrating this behavior over a sufficiently-

broad bandwidth will be ENAQT.

For a more intuitive picture of the effects of bandwidth increases on transport, one can think of broadband illumination as causing dephasing on a lengthscale comparable to the propagation distance over which waveguide 4 has an optical path length difference equal to the illumination coherence length. As an illustrative example, consider two uncoupled waveguides a and b which, at $\lambda = \lambda_0$ have a difference in their propagation constants of $\Delta\beta(\lambda_0) = C_1(\lambda_0)$. If both waveguides are coherently illuminated with broadband light centered at λ_0 , the optical path difference grows as the light propagates, eventually becoming comparable to the illumination coherence length. After some propagation distance z the coherence ρ_{ab} between the two waveguides will decay:

$$\rho_{ab}(z) = \rho_{ab}(0)g^{(1)}\left(\frac{z}{c} \frac{\lambda_0}{2\pi} \Delta\beta_{ab}\right), \quad (7.11)$$

where $g^{(1)}(t)$ is the first-order temporal correlation function, which is proportional to the Fourier transform of the excitation spectrum. If that spectrum is Lorentzian then $g^{(1)}(t) = \text{Exp}(-i\omega t - t/\tau_c)$ where τ_c is the coherence time; in this case coherence is lost at a rate $\gamma = 1/\tau_c$ and the noise acts as Markovian dephasing.

In our experiment, due to our non-Lorentzian spectra (see figure 7.3b), the shape of the decay of the coherence terms will be non-exponential—a signal of non-Markovian behavior. In either case the dephasing noise may counteract other coherent localization phenomena. Furthermore, in real waveguides both the propagation constants and inter-waveguide couplings are wavelength-dependent, and therefore bandwidth noise changes population transfer rates in addition to decreasing coherence terms in $\rho(t)$. Nonetheless, the preceding discussion suffices to estimate the relevant length scales in our simulations. In our second-generation simulators, our target value for $\Delta\beta = C_1(\lambda_0)$ is 1 cm^{-1} , with a target central simulation wavelength of $\lambda_0=820 \text{ nm}$, while those for κ and C_{bath} were 1.5 and 1.75 cm^{-1} , respectively, where C_{bath} is the rate of coupling between bath waveguides.² Meanwhile our maximum bandwidth, while not Lorentzian, has a full width at half-maximum (FWHM) of about 70 nm (see Fig. 7.3b)). Eq. (7.11) thus yields an estimated propagation length of 23 cm for the coherences to decay by a factor of $1/e$. This suggests, as a first estimate, that propagation lengths on the order of 10 cm should be sufficient to observe significant decoherence and thus ENAQT. This could be confirmed via a more microscopically-detailed simulation of the system, which would require accounting for the finite values of κ and C_{bath} as well the precise non-Lorentzian spectral

²Similarly precise values for the first generation simulator are not known, which is one of the motivations for the second-generation simulations, but the values should be of the same order of magnitude.

shapes and the functional dependence of all the coupling and propagation constants on wavelength. Such a simulation would allow a prediction of the ENAQT achievable with a specific spectrum and propagation length, and confirmation that this level of enhancement would be measurable in the laboratory.

Fig. 7.2 shows a theoretical simulation of this waveguide Hamiltonian, with the target values for all propagation and coupling constants, as well as false-color images of the output distribution from our first-generation simulation circuit for comparison.

7.3.1 Fabrication of ENAQT simulation circuits

Our simulation circuits were fabricated in high-purity fused silica (Corning 7980) using a laser direct-write technique whereby Titanium:Sapphire laser pulses are tightly focused into the sample, which is then translated in three dimensions to yield continuous regions of positive refractive index change which act as waveguides. Note that the quantitative details presented here are for the second generation of simulation circuits, which were more carefully characterized during fabrication. However the fabrication of the first generation circuit was qualitatively similar.

In order to obtain single-mode waveguides with the desired propagation and coupling characteristics, laser pulses of duration 150 fs, energy 400 μJ , central wavelength 800 nm, and repetition rate 100 kHz were focused 400 μm below the surface. Index changes result in a volume approximately congruent with the focal region, yielding nearly-elliptical waveguides of approximately $4 \times 16 \mu\text{m}$ in size, where the semi-major axis is perpendicular to the sample surface. With such waveguides, the coupling constants between pairs of waveguides are strongly dependent on angular orientation as well as separation distance [17]. The sink (waveguide 3) and the bath waveguides are all in a plane parallel to the surface, while an angle of 120° between this plane and the other system waveguides was found to minimize next-nearest-neighbor coupling; this geometry is illustrated in the inset of Fig. 7.1d). For these orientation angles, the coupling constants were determined as a function of separation by creating pairs of waveguides with different separations and measuring the output intensities after a propagation length L when one is optically excited. Calling the excited waveguide a and the other b , the coupling constant C_{ab} can be calculated from the output intensities I_a and I_b as $C_{ab} = (1/L) \arctan \sqrt{I_b/I_a}$; see Ref. [17] for further details.

Based on these results the final waveguide separations for the simulation were chosen so as to best achieve several goals: (i) Have a value for C_1 which could be matched, with

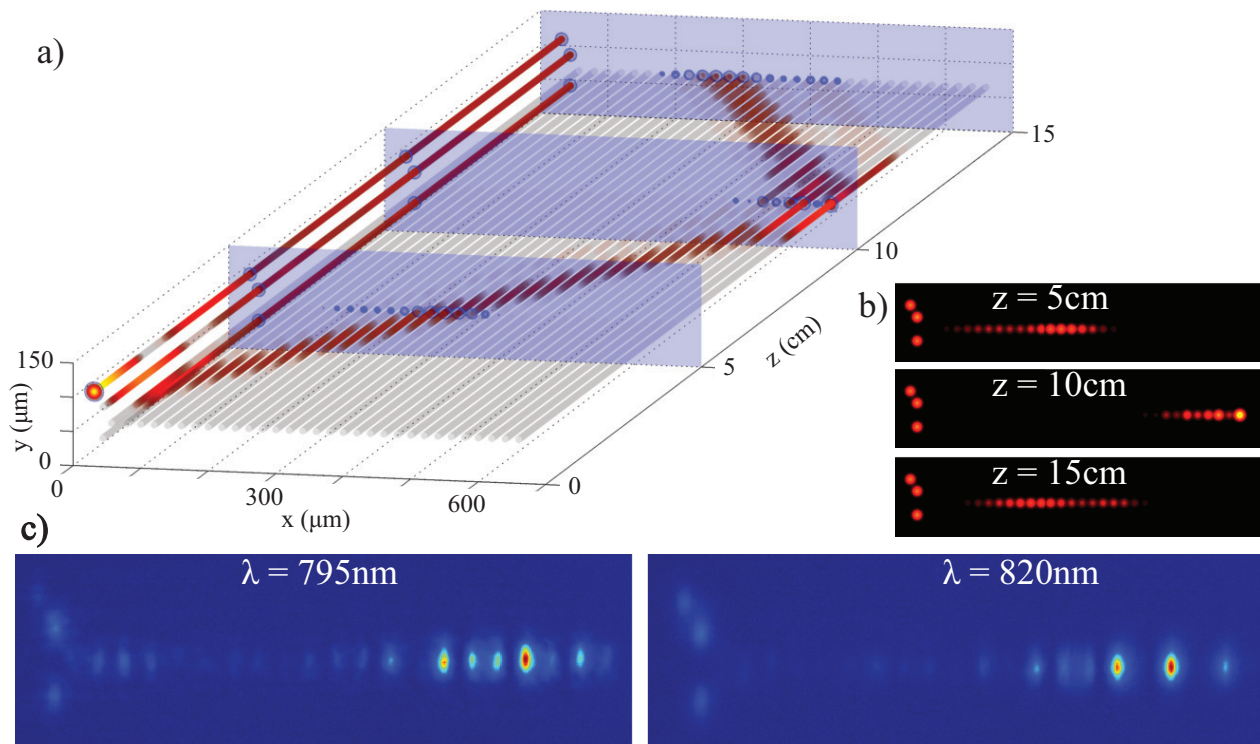


Figure 7.2: Simulated and actual propagation of light in the ENAQT simulation circuit. a) Theoretical tight-binding simulation of light propagation through an ENAQT simulator with our target values for coupling and propagation constants. In this case $\Delta\beta = C_1 = 1 \text{ cm}^{-1}$ at $\lambda_0 = 820 \text{ nm}$. Nearly two thirds of the input power quickly couples into the bath, as expected from Eq. (7.8). Transverse profiles of the light after propagation lengths of 5, 10, and 15 cm are highlighted; compare to the approximate $1/e$ decay length for coherence of 23 cm for a FWHM bandwidth of 70 nm, calculated using the simplified model of Eq. (7.11). The second generation chip includes simulators with those three propagation lengths, achieved by having all waveguides except for number 1 begin 5, 10, or 15 cm before the end of the chip, respectively, while the first generation has only 10 cm. Note that the bath is sufficiently long that light reflecting from the far boundary fails to couple back into the system waveguides during the simulation. This figure was created by R. Heilmann. b) The expected output of this ideal circuit when illuminated with 820 nm monochromatic light after propagation distances of 5, 10, and 15 cm. c) Images of actual output distributions from the first-generation simulator. These measurements were taken with narrowband ($< 1 \text{ nm}$) diode laser input light at $\lambda = 820 \text{ nm}$, our target value for λ_0 , and at $\lambda = 795 \text{ nm}$ which should not satisfy Eq. (7.7) and should thus show higher coupling to the bath. After the propagation distance of 10 cm, the population of waveguide 3 is even less at $\lambda_0=820 \text{ nm}$ than at 795 nm, as expected (2.13% of the total output light at 820 nm vs. 2.58% at 795 nm.) The portion of the total output in the bath waveguides is 76.0% at 820nm whereas at 795 nm it has increased to 81.3%.

small relative error, by $\Delta\beta$. (ii) Have $C_{\text{bath}} > \kappa > C_1$, where C_{bath} is the coupling between bath waveguides, with a sufficient ratio between these coupling constants in order to obtain quasi-Markovian loss from waveguide 3. Note that the loss will be less Markovian as the ratio κ/C_{bath} increases towards unity [22]; however transport enhancement should still be achievable as long as $\kappa/C_{\text{bath}} < 1$. (iii) Remain in a sufficiently weak-coupling regime such that inter-waveguide couplings could be well approximated by a tight-binding model.

For waveguide 4, the writing translation speed was decreased in order to increase the propagation constant. While absolute values of β are difficult to establish, a propagation constant mismatch between a pair of coupled waveguides a and b prevents full power transfer between them; measuring the maximum power transfer allows determination of the ratio $\Delta\beta/C_{ab}$. This technique was used to set $\Delta\beta$ equal to C_1 , with an uncertainty of approximately 8%.

7.4 First-generation ENAQT experiment

The setup employed to measure ENAQT in our first-generation simulator is illustrated schematically in Fig. 7.3a). The illumination consisted of triggered single photons from SPDC [24] in a short periodically-poled crystal; this allowed us to generate significant bandwidth of approximately 70 nm as seen in figure 7.3b). The photon pairs were produced through type-I SPDC of a 410 nm diode pump laser in a 2 mm long ppKTP crystal; while one photon served as trigger, the other could be filtered with 5 nm or 24 nm bandpass filters centered at 820 nm in order to reduce bandwidth, or left unfiltered. These photons were then spatially filtered by single-mode fiber, horizontally polarized by fiber polarization controllers and a polarizing beamsplitter, and then coupled into system waveguide 1 in the circuit. The circuit output was imaged with a telescope and each waveguide output mode could be isolated with an aperture and coupled into a multimode fiber; coincidences were counted between this fiber and the trigger photons. Annotated photographs of the coupling and measurement apparatuses are shown in Fig. 7.4. The isolation and coupling of individual output modes was found to be quite repeatable, with variations of less than 5 μm in the optimal fiber coupler x - and y -translation positions found for a given output mode in separate trials. Coincidences were counted for 60 s for each output mode, including each individual bath waveguide. Coincidence count rates ranged from $< 1 \text{ s}^{-1}$ for the darkest output waveguides with 5 nm filtering up to $> 2000 \text{ s}^{-1}$ for the brightest output waveguide with no spectral filtering.

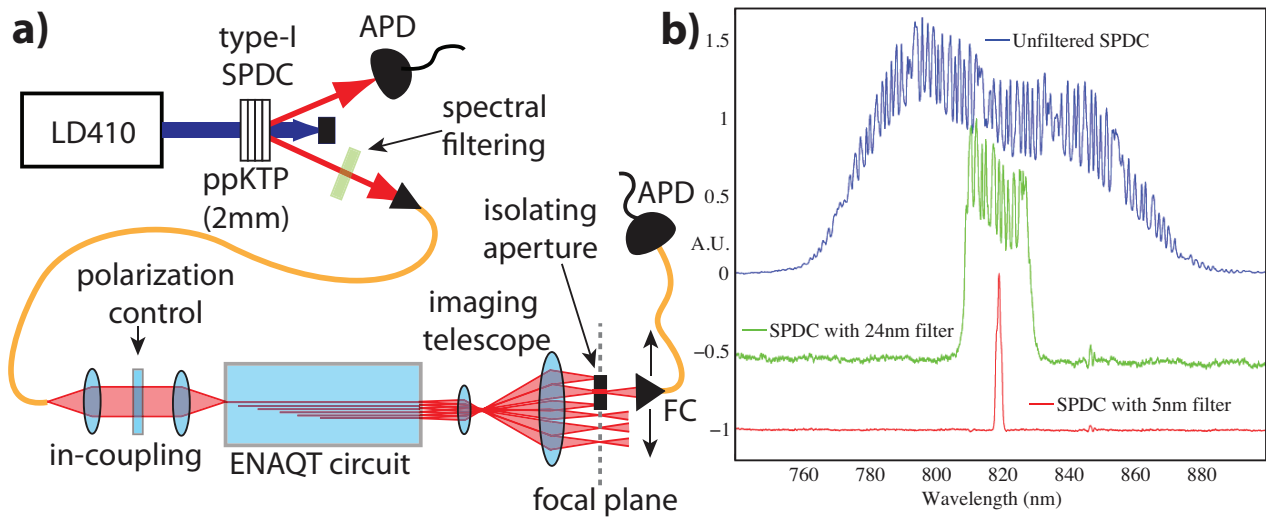


Figure 7.3: Measurement setup and photon spectra. a) Broadband photon pairs are created through spontaneous parametric downconversion (SPDC) in a 2 mm long nonlinear periodically-poled potassium titanyl phosphate (ppKTP) crystal pumped by a 410 nm diode laser. One photon serves as a trigger; the other may be spectrally filtered before being spatially filtered through single-mode fiber, polarized, and coupled into the ENAQT simulation circuit. The circuit output is magnified and imaged to a focal plane with a telescope; the imaging system shown is not to scale and the number of output waveguide modes is much larger than depicted. Each waveguide output mode can be isolated using an adjustable aperture and coupled with an objective lens held in a translatable fiber coupling mount (FC) into a multimode fiber. Photons are detected in coincidence using avalanche photodiodes (APDs.) A removable mirror (not shown) can also be placed in the telescope image plane in order to focus the output via another lens onto a CCD camera for alignment. In measuring the second generation of ENAQT circuits, it was determined that the aperture in the focal plane could be replaced by a large adjustable-width slit formed from two razorblades, and up to ten waveguides could be coupled into the multimode fiber at once with no significant reduction in measurement accuracy. This enables faster and easier determination of the total bath occupation. b) The spectra of our broadband photons in the unfiltered case (blue, top), with a bandwidth of approximately 70 nm full width at half maximum (FWHM), and after filtering with 24 nm (green, middle) and 5 nm (red, bottom) filters, as measured with an Acton SpectraPro 300i spectrometer imaged onto a cooled Princeton Instruments MicroMax CCD camera. The spectra are displaced vertically for ease of viewing; visible noisy oscillations are suspected artifacts of the spectrometer CCD and the low signal levels.

7.4.1 First-generation results

The results of our first-generation ENAQT simulation are shown in figure 7.5. This ENAQT-simulation waveguide array is 10 cm in length. Only the results for the high-dephasing broadband case and the low-dephasing case using the 5 nm spectral filter are shown; the results for the case with 24 nm filtering did not differ significantly from the 5 nm case. In the narrowband case, $71.1 \pm 1.6\%$ of the output signal was found to be in the bath modes, whereas in the broadband case that figure rises to $76.1 \pm 0.5\%$. This absolute increase of 5.0 percentage points corresponds to a measured percentage enhancement in trapping efficiency, or ENAQT, of $7.0 \pm 2.4\%$. The quoted uncertainties stem from Poissonian counting errors in the measured coincident photodetection counts. Accidental coincidence counts have been calculated and subtracted; these tend to artificially increase the low count rates, especially in the tightly-filtered case due to the relatively high detection rate in the trigger detector compared to the high loss in the filtering and simulation; neglecting their subtraction yields a bath output in the narrowband case of 71.6%, a bath output in the broadband case of 76.2%, and a measurable but not quite statistically significant reduction in ENAQT to $6.3 \pm 2.3\%$.

Notably, this first-generation simulation chip was designed for a central operation wavelength of 805 nm rather than 820 nm. Furthermore, the precise inter-waveguide couplings are not known, and finally we suspect that the combination of waveguide spacing and writing conditions led the simulation to be out of the tight-binding regime, with significant non-orthogonality between waveguide modes. In order to better approach tight-binding, to have better-characterized fabrication conditions to enable modeling, and to allow multiple interaction lengths, we fabricated and measured a second generation of ENAQT simulation circuits.

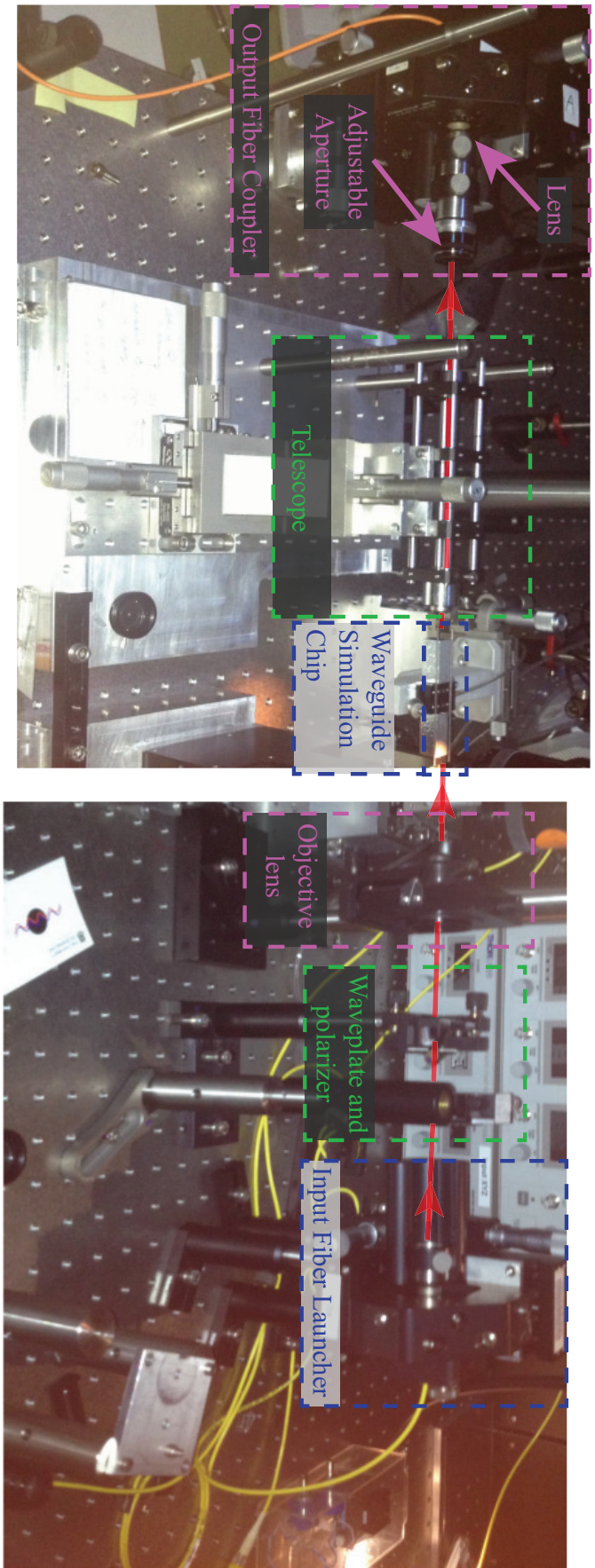


Figure 7.4: The experimental setup for coupling photons into the ENAQT simulation chip and collecting the output signal. Note that the single photon beam, shown in red, travels from right to left. Photons coming via fiber from the broadband SPDC source are collimated at the input fiber launcher before being properly polarized with a waveplate and Glan-Taylor polarizer. They are then focused into the waveguide simulation chip using a carefully-adjusted objective lens mounted with six translational and rotational degrees of freedom. The waveguide simulation chip is difficult to see as it looks like an unmarked piece of glass but it is being held by vacuum onto the indicated small black mount, which is held on a three-axis translation stage. A telescope, also mounted with three translational degrees of freedom, magnifies the output and images onto the plane of an adjustable aperture which is used to isolate individual output waveguides. The aperture is mounted on the end of fiber coupler, the position of which can be adjusted to isolate any output waveguide, and the signal passing through the aperture is coupled into multimode fiber and transmitted to the avalanche photodiode single photon detector (APD).

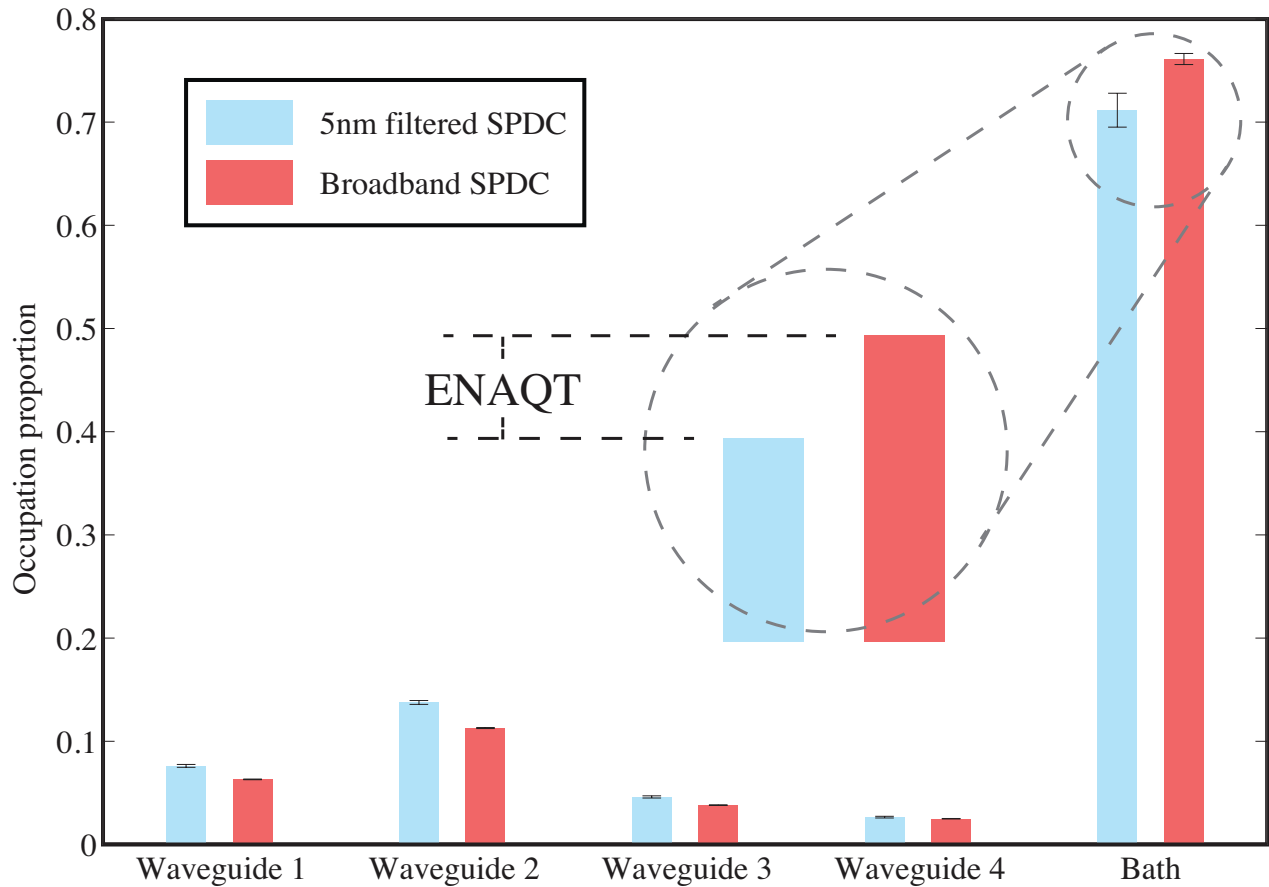


Figure 7.5: Occupation proportion of each of the four ENAQT site waveguides as well as the sum of all the bath waveguides after 10 cm propagation in our first-generation ENAQT simulation chip. Blue bars (left) show results from the simulation of the low-noise case, where the excitation photons are spectrally filtered to a bandwidth of 5 nm. Pink bars (right) result from the simulation of the high-noise case, done with unfiltered broadband downconversion photons having a bandwidth of approximately 70 nm FWHM. This bandwidth leads to an enhancement of transport efficiency into the bath (ENAQT) of $7 \pm 2\%$. This uncertainty as well as the error bars shown are due to Poissonian noise in the photon pair coincidence counts; all quoted uncertainties correspond to one standard deviation. The error bars may be too small to see clearly for the four main waveguides.

7.5 Second-generation ENAQT circuits and results

For the second-generation ENAQT simulations, 15 circuits were fabricated in five cycles of three circuits each. The parameter that varies between the five cycles is the fabrication writing speed for waveguide 4, which differs from that in the other waveguides by 8%, 9%, 10%, 11%, and 12% respectively for cycles 1 to 5. This should in turn yield varying values of $\Delta\beta$; thereby mitigating uncertainty in our determinations of the coupling and propagation constants by testing circuits with this range of parameters. Within each cycle, simulation circuits were written with propagation lengths of 5, 10, and 15 cm; this was accomplished by having all waveguides except for the input (system waveguide 1) start 5, 10, or 15 cm before the end of the chip respectively.

For each of these 15 circuits, the system waveguides are separated by $21.1 \mu\text{m}$, the bath waveguides are separated by $15.5 \mu\text{m}$, and waveguide 3 is separated from the first bath waveguide by $16.3 \mu\text{m}$. These distances were chosen to yield coupling constants $C_1 = 1.0 \text{ cm}^{-1}$, $\kappa = 1.5 \text{ cm}^{-1}$, and $C_{\text{bath}} = 1.75 \text{ cm}^{-1}$ at $\lambda = 820 \text{ nm}$.

Because there were 15 circuits to measure, each with between 14 and 34 individual waveguides (depending on the propagation length, which dictates the number of bath waveguides needed), the previous measurement method of individually isolating each output mode in the telescope focal plane and then counting coincidences was found to be too slow. A new method was devised where an adjustable-width slit formed by a pair of precisely-translatable razorblades replaced the aperture (see Fig. 7.3a)). Up to ten waveguides at a time could be isolated with this slit and coupled into the multimode fiber, and this measurement method was found to be repeatable and to generate results which do not differ significantly from the previous measurement method.

Preliminary ENAQT results from the 15 cm circuits from each of the five cycles are presented in Fig. 7.6. The measured ENAQT depended strongly on the percentage laser writing speed difference for waveguide 4, as expected, and as can be seen in the figure is in general positively correlated with that difference. However, in all cases the total ENAQT found was negative: increasing the illumination bandwidth actually decreased transport efficiency, at least for the measured spectra.

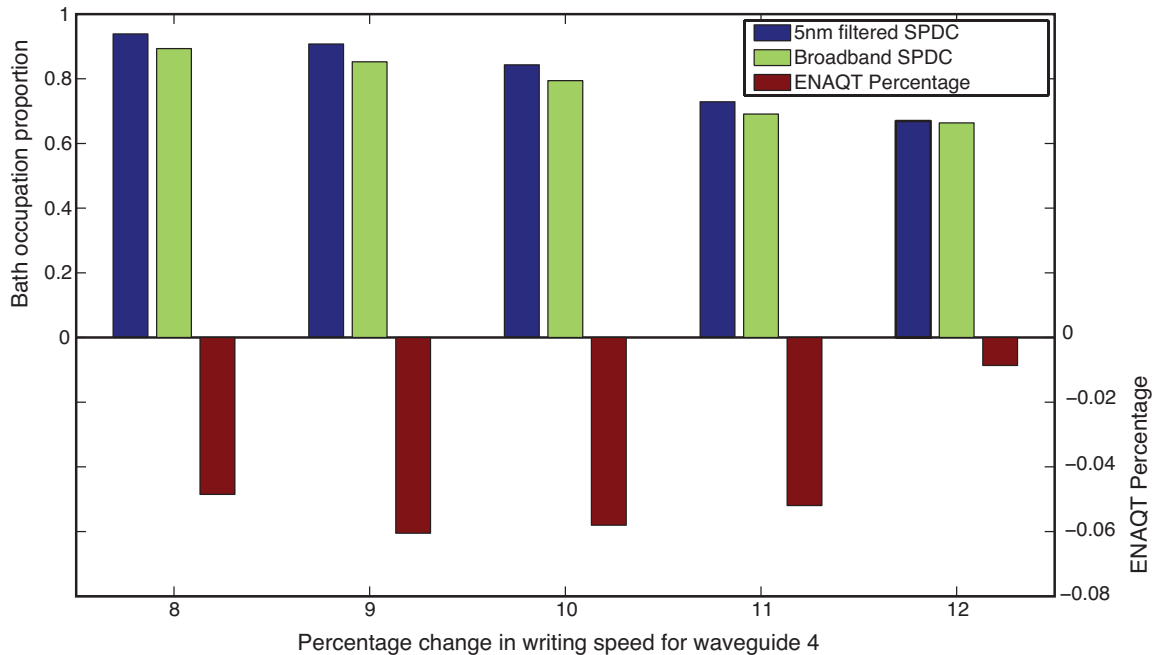


Figure 7.6: Preliminary second-generation ENAQT results: bath occupation proportion after 15 cm propagation for unfiltered (green bars) and 5 nm bandpass filtered (blue bars) SPDC broadband photons, and corresponding percentage ENAQT (dark red bars), as a function of the five tested percentage differences in laser-writing speed for waveguide 4. Note the differing vertical scales above and below zero. The measured ENAQT is negative in all five cases, meaning that bandwidth broadening decreases transport efficiency; however for the highest writing speed difference, the negative enhancement is near zero.

7.5.1 Modeling the effects of fabrication parameter variance

A possible explanation for the results in Fig. 7.6, and in particular for the positive correlation between measured ENAQT and the percentage change in writing speed for waveguide 4, is that the induced $\Delta\beta$ is insufficiently large to match C_1 and thus satisfy condition (7.7) at 820 nm in all instances of second-generation simulators. However, we suspected that condition (7.7) might be satisfied for a different value of λ_0 . In order to investigate the plausibility of this explanation we numerically modeled the effects on $\Delta_{\mathcal{H}}(\lambda)$ of deviations from intended fabrication parameter values, specifically the waveguide diameter ρ and δ . Here $\delta = (\Delta n_4 - \Delta n_{\text{system}})/(\Delta n_{\text{system}})$ is the percentage increase in the index contrast Δn of waveguide 4 compared to the other system waveguides, and $\Delta_{\mathcal{H}}(\lambda)$ parametrizes the deviation from the ideal circuit Hamiltonian (see Sec. 7.3, specifically Eq. (7.7)). The results of this modeling are shown in Fig. 7.7, and the method is described below.

For simplicity, we first determined the radius of a circular, top-hat index-profile waveguide which would yield the same coupling at a separation of $21.1 \mu\text{m}$ (the separation between system waveguides) as our best estimate for C_1 of 1.0 cm^{-1} . Using the coupled waveguide theory developed in Ch. 3, including a correction for incompletely-orthogonal waveguide modes, and an estimate for the maximum refractive index change in each waveguide of $\Delta n = 5 \times 10^{-4}$, we found that a circular waveguide in pure fused silica of effective radius $\rho = 4.9 \mu\text{m}$ would yield a coupling of 1.0 cm^{-1} at a separation of $21.1 \mu\text{m}$ for light of wavelength $\lambda = 820 \text{ nm}$. This approximation is reasonable because the shape of the guided mode at a sufficient distance from the waveguide core—and thus the overlap between the two guided modes which determines evanescent coupling strength—is largely independent of the microscopic geometric details of the waveguide core shape.

A $\delta = 5\%$ increase in refractive index contrast Δn_4 for waveguide 4 over the other system waveguides yielded our best estimate for $\Delta\beta$ of 1 cm^{-1} at 820 nm . While changing the writing speed may affect both the index contrast and the size of waveguide 4, as a first approximation it is reasonable to assume that $\Delta\beta$ in our simulation is caused entirely by change in the index, because the effects of index change are proportionally much greater than those of radius change on β [25, Sec. 29-6]. Using these values as baselines, we calculated $\Delta\beta(\lambda)$, $C_1(\lambda)$, and their difference $\Delta_{\mathcal{H}}(\lambda)$ for a wide range of variations in δ and ρ . The results of this modeling are shown in Fig. 7.7. An important result is that for most reasonable variations in δ and ρ , the shape of $\Delta_{\mathcal{H}}(\lambda)$ does not change significantly, and in particular neither flattens out nor develops an extremum over the intended wavelength range. Instead it mostly shifts, and will therefore cross $\Delta_{\mathcal{H}}(\lambda) = 0$ for a wavelength value $\lambda = \lambda_0$ which is different from the intended $\lambda_0 = 820 \text{ nm}$. In particular, so long as $\frac{d\Delta_{\mathcal{H}}}{d\lambda}$ does not change sign and maintains a sufficient absolute value over a significant but achievable wavelength range, ENAQT should be observable by centering our spectra closer to the optimal value for λ_0 .

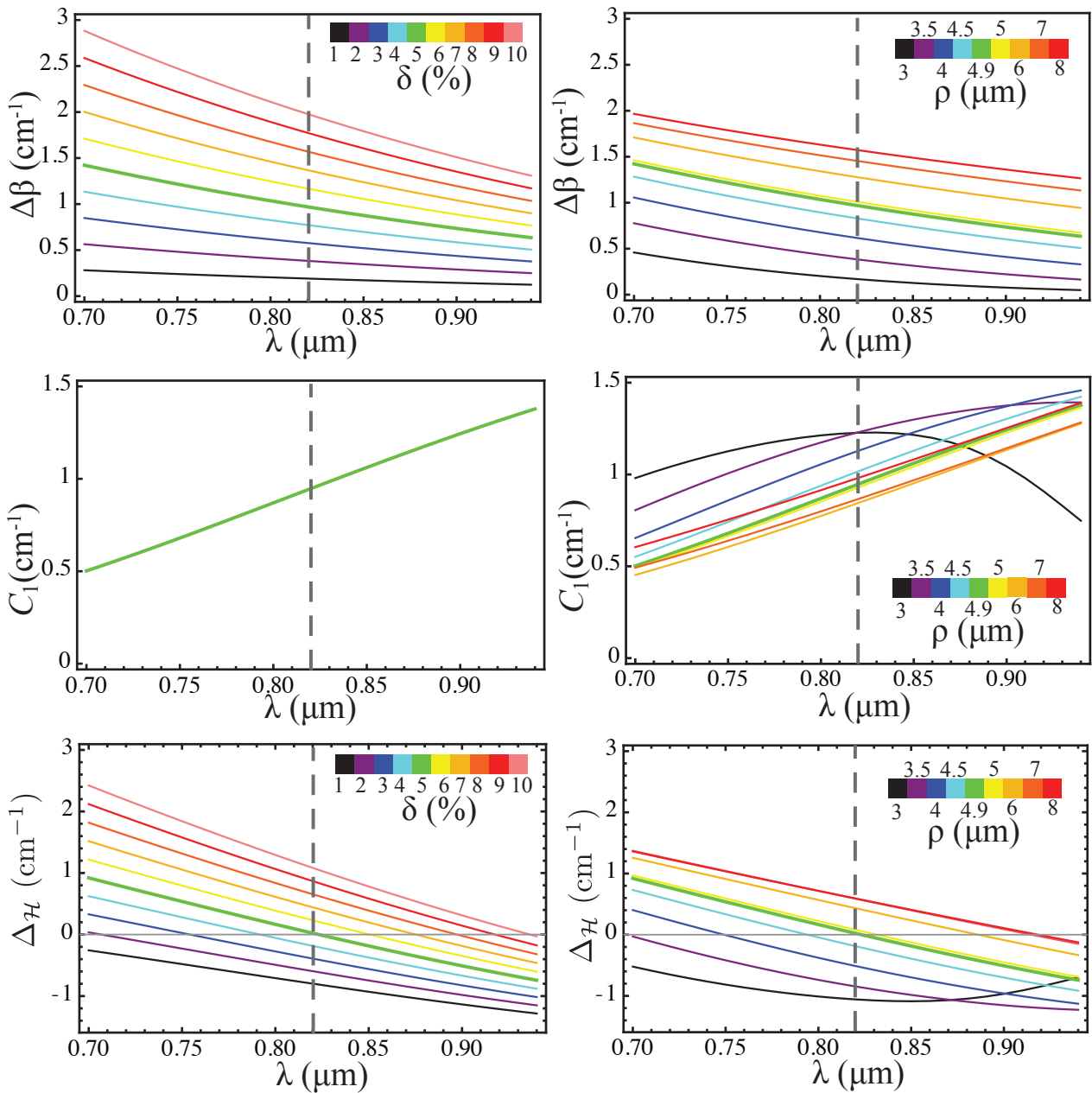
7.5.2 Monochromatic characterization results

Based on such considerations, we measured the output proportion in the bath for 19 different narrowband wavelengths ranging from 770 to 870 nm for the 15 cm ENAQT circuit from the cycle with a writing speed increase of 12% , which had been the most promising second-generation simulation circuit at $\lambda_0 = 820 \text{ nm}$ as shown in Fig. 7.6. The measured wavelengths were generated using a tunable Titanium:Sapphire laser (Spectra-Physics Tsunami) in quasi-continuous-wave mode. The results are presented in Fig. 7.8.

However, the measurements show a notable minimum in the bath occupation proportion

around 790 nm, with a minimum value of 69%. This is quite close to the optimal value at λ_0 of $2/3$ found in Sec. 7.3. This suggests that perhaps the optimal value of λ_0 for simulating ENAQT in this circuit is close to 790 nm, which is plausible: as can be seen in Fig. 7.7, such a difference in λ_0 would only require a reduction in δ from 5% to approximately 4% (cyan line, lower left panel,) or ρ from 4.9 μm to about 4.5 μm (cyan line, lower right panel,) or some combination of the two. This evidence strongly suggests that we may be able to both model and measure ENAQT in this cycle of simulation circuits with a broadband illumination source centered near 790 nm, instead of at 820 nm.

Figure 7.7 (*facing page*): Modeling the effects of waveguide parameter variations on the $\Delta_{\mathcal{H}}(\lambda)$, a parameter which quantifies the deviation from the condition (7.7) for the ideal ENAQT Hamiltonian. The top row shows the variation of $\Delta\beta(\lambda)$, the middle row the variation of $C_1(\lambda)$, and the bottom row the variation of $\Delta_{\mathcal{H}}(\lambda) = \Delta\beta(\lambda) - C_1(\lambda)$. In the left column these functions are plotted for various values of δ , the percentage difference in index contrast for waveguide 4, ranging from 1% to 10%. For the right column they are plotted as a function of effective waveguide radius ρ when treating the waveguides as circular waveguides with a top-hat index profile and an index contrast of $\Delta n = 5 \times 10^{-4}$, as described in the text. For the left column, my best estimate of $\rho = 4.9 \mu\text{m}$ is assumed, whereas for the right column my best estimate of $\delta = 5\%$ is assumed. In every panel the green line represents the function with those two best-estimate parameters; note that this line shows values for $\Delta\beta$ and C_1 of 1 cm^{-1} and $\Delta_{\mathcal{H}} = 0$ at 820 nm (dotted grey line), as expected. For the middle left panel, only one line is shown because changes in δ for waveguide 4 obviously do not affect the coupling C_1 between two other system waveguides. The much higher curvatures for $C_1(\lambda)$ for low values of ρ , especially at higher wavelengths, are due to the increasing non-orthogonality of the individual waveguide modes and the corresponding high deviation from tight-binding conditions for these loosely-confined guided modes. For all parameter variations shown, with the exception of the smallest ρ values, the main effect on $\Delta_{\mathcal{H}}(\lambda)$ is simply to shift the curve without significantly altering its shape over this wavelength range. This suggests that circuits with reasonable deviations from intended fabrication parameters may still be useful for simulating ENAQT but with a different central wavelength λ_0 . The desired value of λ_0 would simply be that for which $\Delta_{\mathcal{H}}(\lambda) = 0$.



(Caption on facing page.)

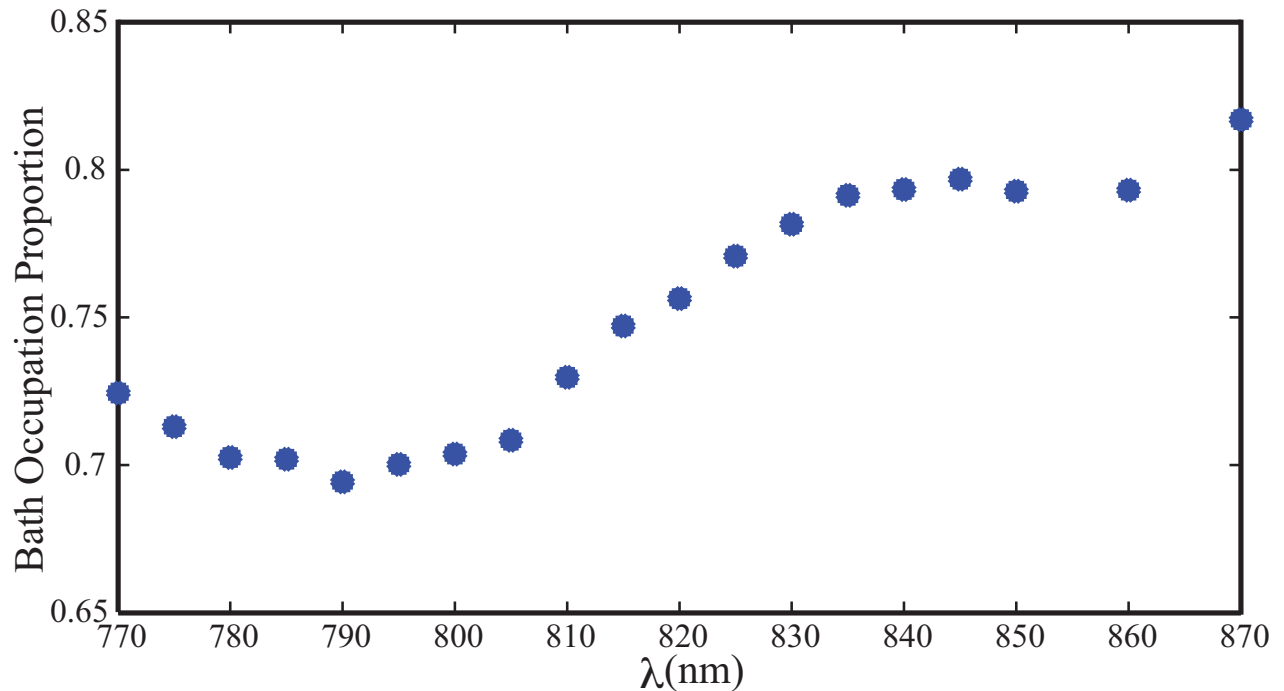


Figure 7.8: The occupancy of the bath as a function of wavelength λ for narrow-band (few nm) illumination for the most promising second-generation 15 cm ENAQT circuit. Note the clear minimum when λ is approximately 790 nm. These results suggest that this circuit may allow better ENAQT simulation with a central wavelength of $\lambda_0=790$ nm as opposed to the design wavelength of $\lambda_0 = 820$ nm.

7.6 Conclusions and future work

Our simulation of ENAQT in an experimental toy model consisting of variable-bandwidth photons in an array of coupled waveguides is not only the first laboratory simulation of this interesting transport phenomenon, but also one of the first demonstrations of an analog photonic simulation of a specific, non-trivial Hamiltonian with open-systems dynamics including controlled loss and dephasing. In our first-generation ENAQT simulator we have demonstrated a statistically-significant transport enhancement of $7.2 \pm 2.4\%$; however we were not able to measure temporal dynamics or to adequately model our simulator.

Our second generation simulators should in principle yield greater transport enhancement and allow measurements after three different propagation distances in order to illuminate the transport dynamics. However, measurements of these simulation circuits to date suggest that the optimal central simulation wavelength may differ from its intended value, by about 30 nm in the specific case of the most promising set of circuits. We are currently confirming

these preliminary results for the second-generation simulators and planning for construction of a new source of broadband illumination using either SPDC or white light, with adjustable filtering using prisms or gratings as diffractive elements. Once this is achieved, careful work will be necessary to develop a phenomenologically adequate model in order to compare with our resulting data, which we expect will show even greater transport enhancement than in our first-generation simulator.

Acknowledgments

This chapter reports on an ongoing research project and is based in part on a preliminary draft of a paper about that research. The author list on that paper will be Devon N. Biggerstaff, René Heilmann, Ivan Kassal, Aidan A. Zecevik, Alessandro Fedrizzi, Alexander Szameit, and Andrew G. White.

References

- [1] Engel, G. S. *et al.* Evidence for wavelike energy transfer through quantum coherence in photosynthetic systems. *Nature* **446**, 782–6 (2007). 109, 113
- [2] Panitchayangkoon, G. *et al.* Long-lived quantum coherence in photosynthetic complexes at physiological temperature. *Proc. Natl. Acad. Sci. U.S.A.* **107**, 12766–12770 (2010). 109
- [3] Collini, E. *et al.* Coherently wired light-harvesting in photosynthetic marine algae at ambient temperature. *Nature* **463**, 644–648 (2010). 109
- [4] Wong, C. Y. *et al.* Electronic coherence lineshapes reveal hidden excitonic correlations in photosynthetic light harvesting. *Nature Chem.* **4**, 396–404 (2012). 109
- [5] Mülken, O. & Blumen, A. Continuous-time quantum walks: Models for coherent transport on complex networks. *Phys. Rep.* **502**, 37–87 (2011). 109
- [6] Anderson, P. W. Absence of diffusion in certain random lattices. *Phys. Rev.* **109**, 1492–1505 (1958). 109, 112
- [7] Ishizaki, A. & Fleming, G. R. Unified treatment of quantum coherent and incoherent hopping dynamics in electronic energy transfer: reduced hierarchy equation approach. *J. Chem. Phys.* **130**, 234111 (2009). 109
- [8] Ishizaki, A. & Fleming, G. R. Theoretical examination of quantum coherence in a photosynthetic system at physiological temperature. *Proc. Natl. Acad. Sci. U.S.A.* **106**, 17255–17260 (2009). 109
- [9] Hoyer, S., Sarovar, M. & Whaley, K. B. Limits of quantum speedup in photosynthetic light harvesting. *New J. Phys.* **12**, 065041 (2010). 109
- [10] Fassioli, F. & Olaya-Castro, A. Distribution of entanglement in light-harvesting complexes and their quantum efficiency. *New J. Phys.* **12**, 085006 (2010). 109
- [11] Strümpfer, J., Şener, M. & Schulten, K. How quantum coherence assists photosynthetic light-harvesting. *J. Phys. Chem. Lett.* **3**, 536–543 (2012). 109
- [12] Fujita, T., Brookes, J. C., Saikin, S. K. & Aspuru-Guzik, A. Memory-assisted exciton diffusion in the chlorosome light-harvesting antenna of green sulfur bacteria. *J. Phys. Chem. Lett.* **3**, 2357–2362 (2012). 109

- [13] Kassal, I., Yuen-Zhou, J. & Rahimi-Keshari, S. Does coherence enhance transport in photosynthesis? *J. Phys. Chem. Lett.* **4**, 362–367 (2013). 109
- [14] Plenio, M. B. & Huelga, S. F. Dephasing-assisted transport: quantum networks and biomolecules. *New J. Phys* **10**, 113019 (2008). 109, 112, 113
- [15] Chin, A., Datta, A., Caruso, F., Huelga, S. & Plenio, M. Noise-assisted energy transfer in quantum networks and light-harvesting complexes. *New J. Phys.* **12**, 065002 (2010). 109
- [16] Rebentrost, P., Mohseni, M., Kassal, I., Lloyd, S. & Aspuru-Guzik, A. Environment-assisted quantum transport. *New J. Phys* **11**, 033003 (2009). 109, 112, 113
- [17] Szameit, A., Dreisow, F., Pertsch, T., Nolte, S. & Tünnermann, A. Control of directional evanescent coupling in fs laser written waveguides. *Opt. Express* **15**, 1579–1587 (2007). 110, 117
- [18] Kassal, I. & Aspuru-Guzik, A. Environment-assisted quantum transport in ordered systems. *New J. Phys* **14**, 053041 (2012). 111
- [19] Olbrich, C. *et al.* From atomistic modeling to excitation transfer and two-dimensional spectra of the FMO light-harvesting complex. *J. Phys. Chem. B* **115**, 8609–8621 (2011). 113
- [20] Mohseni, M., Shabani, A., Lloyd, S. & Rabitz, H. Energy-scales convergence for optimal and robust quantum transport in photosynthetic complexes. *J. Chem. Phys.* **140** (2014). 112
- [21] Chen, X. & Silbey, R. J. Excitation energy transfer in a non-markovian dynamical disordered environment: Localization, narrowing, and transfer efficiency. *J. Phys. Chem. B* **115**, 5499–5509 (2011). 112
- [22] Longhi, S. Nonexponential decay via tunneling in tight-binding lattices and the optical Zeno effect. *Phys. Rev. Lett.* **97**, 110402 (2006). 114, 119
- [23] Biagioni, P. *et al.* Experimental demonstration of the optical Zeno effect by scanning tunneling optical microscopy. *Opt. Express* **16**, 3762–3767 (2008). 114
- [24] Ghosh, R., Hong, C. K., Ou, Z. Y. & Mandel, L. Interference of two photons in parametric down conversion. *Phys. Rev. A* **34**, 3962–3968 (1986). 119
- [25] Snyder, A. W. & Love, J. *Optical Waveguide Theory* (Chapman and Hall, 1983). 126

Chapter 8

Engineering integrated photonics for heralded quantum gates

Submitted: *Light: Science and Applications*, August 2014

T. Meany^{1,†}, D. N. Biggerstaff^{2,3,†}, M. A. Broome^{2,3}, A. Fedrizzi^{2,3}, M. Delanty¹,
M. J. Steel¹, A. Gilchrist⁴, G. D. Marshall⁵, A. G. White^{2,3} & M. J. Withford¹

¹ *Centre for Ultrahigh bandwidth Devices for Optical Systems, ⁴Centre for Engineered Quantum Systems, Department of Physics and Astronomy, Macquarie University, NSW 2109, Australia*

² *Centre for Engineered Quantum Systems, ³Centre for Quantum Computer and Communication Technology, School of Mathematics and Physics, University of Queensland, Brisbane QLD 4072, Australia*

⁵ *HH Wills Physics Laboratory, Tyndall Avenue, Bristol BS8 1TL, UK*

[†]These authors contributed equally to this work.

Abstract

Scaling up linear-optics quantum computing will require multi-photon gates which are compact, phase-stable, exhibit excellent quantum interference, and have success heralded by the detection of ancillary photons. We investigate implementation of the optimal known gate design which meets these requirements: the Knill controlled- Z gate, implemented in integrated laser-written waveguide arrays. We study device action in the presence of deviations from optimal fabrication parameters both theoretically and using 12 integrated circuits characterised

using coherent and quantum interference techniques. Our best device achieves a fidelity of 0.931 ± 0.001 with the ideal 4×4 unitary circuit and a process fidelity of 0.680 ± 0.005 with the ideal computational-basis process.

8.1 Introduction

Effective optical nonlinearities realised probabilistically through measurement [1], combined with significant recent progress in on-chip integration of efficient photon sources [2–5] and detectors [6–8], form a promising architecture for quantum information processing and simulation. However, to scale efficiently, linear optics quantum computing (LOQC) will require entangling gates which are logically scalable—*i.e.* where successful operation is heralded by the detection of non-computational ‘ancilla’ photons—as well as physically scalable, *i.e.* implemented in a compact and phase-stable architecture. Integrated, non-heralded entangling gates have been demonstrated [9, 10] as have heralded gates in bulk optics [11, 12], but to date combining both forms of scalability has proven elusive.

The simplest heralded entangling two-qubit photonic gate design, with the highest known success probability, was found by Knill [13] and implements a controlled- Z operation with probability $2/27$. This heralded CZ design, henceforth called the h CZ, relies on pairwise non-classical interference of four indistinguishable photons in a circuit with four particular beam-splitters (BSs), as shown in Fig.8.1(a), as well as a stable phase shift of precisely π between the first and second BS pairs. Integrated arrays of coupled waveguides could enable compact, phase-stable circuits with the requisite splittings and phase for Knill’s design. However, integrated h CZ circuits require a waveguide crossover which is difficult to achieve lithographically. The femtosecond laser direct-write (FLDW) technique allows 3D waveguide arrays, simplifying such crossovers, along with demonstrated high mode indistinguishability. This technique has recently been used to demonstrate a wide variety of quantum photonics circuitry [14, 15], including multiport and arbitrary-phase directional couplers [16–18], all-optical routers [19], circuits for small-scale quantum simulations [20–22], quantum walks [23], and non-heralded quantum gates [10].

Here we investigate heralded quantum photonics both theoretically and experimentally, specifically the implementation of the h CZ gate using the direct-write technique, with a particular focus on its action in the presence of deviations from optimal fabrication phase and reflectivity parameters. We derive the variation of two metrics—the optical-circuit mode-fidelity and the computational-basis process-fidelity—with respect to such deviations. We

further detail the fabrication of 12 prototype circuits including a novel and simple method for achieving the requisite internal phase, and their full characterisation using coherent techniques as well as quantum interference which confirms their excellent mode indistinguishability and suitability for the single-photon regime.

8.2 Materials and Methods

The optical circuit for the $h\text{CZ}$ gate is shown in Fig. 8.1(a). The *control* and *target* qubits are each encoded as single photons across a pair of modes. In the diagram, the modes representing the logical $|0\rangle$ component are not shown as these modes undergo no transformation. Modulo local phases on the input and output modes, this circuit implements a heralded CZ operation: conditioned on the detection of one photon in each ancilla mode it flips the sign of the $|11\rangle$ -term of an arbitrary two-qubit input state $\alpha_{00}|00\rangle + \alpha_{10}|10\rangle + \alpha_{01}|01\rangle + \alpha_{11}|11\rangle$.

8.2.1 Circuit modelling and design.

In order to investigate gate performance in the presence of imperfections, we first model device operation as follows. We assume four single-mode waveguides coupled by BSs as in Fig. 8.1(b). The quantum state of the light is described by four bosonic creation operators a_C^\dagger , a_T^\dagger , a_A^\dagger , and a_B^\dagger which create a photon in the control, target, and two ancillary modes respectively. We employ the symmetric BS convention so that two modes a_1 and a_2 transform as

$$\text{BS}(\theta): \quad a_1^\dagger \rightarrow a_1^\dagger \cos \theta + ia_2^\dagger \sin \theta, \quad a_2^\dagger \rightarrow a_2^\dagger \cos \theta + ia_1^\dagger \sin \theta. \quad (8.1)$$

We first consider a photon or coherent state in a superposition of the modes $\{C, T, A, B\}$, input into a circuit of the form in Fig. 8.1. The circuit then maps the input creation operators a^\dagger to the outputs b^\dagger via the transformation $b_k^\dagger = \sum_j U_{jk}^{\text{circ}} a_j^\dagger$, where U^{circ} is a unitary matrix. We allow for arbitrary splitting parameter angles θ_n , $n = \{1, \dots, 4\}$. The requisite internal phase shift is implemented by an additional phase of π on BS3, equivalent to $\theta_3 \rightarrow -\theta_3$. Using Eq.(8.1) and allowing for additional undesired phase shifts ($a_n^\dagger \rightarrow e^{i\phi_n} a_n^\dagger$) between the BS pairs, we find that modulo local external phases, all these unwanted internal phases can be collected into a single net phase shift $\phi_N = \phi_c + \phi_a - \phi_b - \phi_t$. For the total circuit action we thus

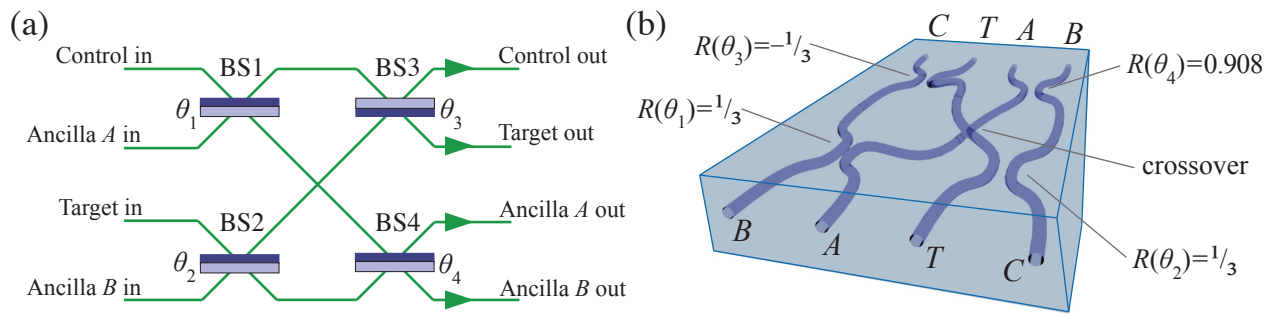


Figure 8.1: (a) The circuit for a $h\text{CZ}$ gate showing paths for computational and ancillary photons: the four modes undergo four beamsplitting operations with reflectivities $R(\theta_n) = \cos^2(\theta_n)$ as described in Eq. (8.1). The light-coloured side indicates the surface yielding a relative π phase change upon reflection. (b) The circuit modelled as a waveguide array, showing the crossover and the optimal reflectivities for the four BSs, which are implemented using controlled evanescent coupling between closely-separated waveguides. The waveguides are separated by $127 \mu\text{m}$ at the device end facets; fan-in and fan-out regions are not shown.

find:

$$U^{\text{circ}} = \begin{bmatrix} \cos \theta_1 \cos \theta_3 & \cos \theta_2 \sin \theta_3 & \cos \theta_1 \sin \theta_3 & \sin \theta_2 \sin \theta_3 \\ \cos \theta_1 \sin \theta_3 & -\cos \theta_2 \cos \theta_3 & \sin \theta_1 \sin \theta_3 & -\cos \theta_3 \sin \theta_2 \\ \cos \theta_4 \sin \theta_1 & e^{i\phi_N} \sin \theta_2 \sin \theta_4 & -\cos \theta_1 \cos \theta_4 & -e^{i\phi_N} \cos \theta_2 \sin \theta_4 \\ \sin \theta_1 \sin \theta_4 & -e^{i\phi_N} \cos \theta_4 \sin \theta_2 & -\cos \theta_1 \sin \theta_4 & e^{i\phi_N} \cos \theta_2 \cos \theta_4 \end{bmatrix}. \quad (8.2)$$

Up to external phases and in the absence of extra phase ϕ_N , the ideal matrix $U^{h\text{CZ}}$ given by Knill [13] is achieved by the target angles of $\theta_1 = \theta_2 = \theta_3 = \arccos \sqrt{1/3}$, and $\theta_4 = \arccos \sqrt{\frac{1}{2} + \frac{1}{\sqrt{6}}}$.

We employ two metrics to assess the design accuracy of a physical circuit for a $h\text{CZ}$ gate. The *mode fidelity* F_m , directly compares the 4×4 circuit mapping matrix U^{circ} to the ideal unitary matrix $U^{h\text{CZ}}$, and is given by $F_m = |\text{Tr}(U^{h\text{CZ}\dagger} U^{\text{circ}})|^2 / N^2$. This metric has the advantage of ease of calculation, but only partially captures how the device would function with qubits and heralding. For instance if the ancilla were swapped prior to detection, F_m would drop but there would be no effect on the heralded gate. The second metric crucially addresses device action in the space of the computational qubits, after successful heralding. A quantum process \mathcal{E} can be represented abstractly as a quantum state $\rho_{\mathcal{E}}$ via the *Jamiolkowski isomorphism* [24]. Given $\rho_{\mathcal{E}}$, the obvious figure of merit is the *process fidelity*: $F_p = \text{Tr}\{\rho_{\text{CZ}}^\dagger \rho_{\mathcal{E}}\}$ which simply compares the state representing the process and the state ρ_{CZ} representing an ideal CZ gate [25, 26].

The most direct way to calculate $\rho_{\mathcal{E}}$ is to consider a maximally-entangled state $|\phi_{\text{max}}\rangle$

between the Hilbert space on which the process acts, and another fictitious space of the same dimension. The process acts on one half, and the resulting total state is exactly $\rho_{\mathcal{E}}$. As our computational input is two qubits, the entangled state is $|\phi_{\max}\rangle = (|0000\rangle + |0101\rangle + |1010\rangle + |1111\rangle)/2$. After a CZ operation on the first two qubits the result is $|\phi_{\text{CZ}}\rangle = (|0000\rangle + |0101\rangle + |1010\rangle - |1111\rangle)/2$, and the corresponding process state is $\rho_{\text{CZ}} = |\phi_{\text{CZ}}\rangle\langle\phi_{\text{CZ}}|$.

Given that each qubit comprises a photon in two modes, $|\phi_{\max}\rangle$ involves four photons encoded across eight modes. With the addition of the two ancillary modes, the full entangled input state is thus represented using boson creation operators as $(1 + a_T^\dagger a_{T2}^\dagger + a_C^\dagger a_{C2}^\dagger + a_C^\dagger a_{C2}^\dagger a_T^\dagger a_{T2}^\dagger) a_A^\dagger a_B^\dagger |\mathbf{0}\rangle$ where $|\mathbf{0}\rangle$ is a multimode bosonic vacuum. The circuit transforms a_C^\dagger , a_T^\dagger , a_A^\dagger , and a_B^\dagger according to U^{circ} , and gate success is heralded by measuring single photons in each ancillary mode, so these modes are projected out in the resulting state, inducing a CZ on the remaining modes.

A subtle problem arises when the photonic gate is not perfectly balanced. There is then a non-zero amplitude for the states proportional to $(a_C^\dagger)^2$ and $(a_T^\dagger)^2$, which lie outside the qubit space and represent errors. In characterising circuit performance, we account for these errors by calculating the process fidelity against a version of ρ_{CZ} which is extended to include these two states but with zero support, and thus any weight on these terms will always reduce F_p .

Fig. 8.2 shows the variation of the process and mode fidelity with deviations in BS reflectivity and net internal phase. Both fidelity metrics are much less sensitive to small deviations in phase than in splitting ratios. Perhaps unsurprisingly the mode fidelity is far less sensitive to errors overall.

8.2.2 Device fabrication

The circuits were fabricated using the FLDW technique wherein a tightly focused femtosecond laser generates a localised refractive index contrast in a glass substrate. By translating the glass in (x, y, z) with respect to the incident laser, arbitrary 3D regions of net-positive refractive index change can be produced. Our fabrication employed a titanium sapphire oscillator (800 nm centre wavelength, < 50 fs pulse duration) with 5.1 MHz repetition rate [27, 28]. A telescope was used to overfill the input pupil of a $100\times$ oil immersion objective which focused the laser into the boro-aluminosilicate sample (Corning Eagle 2000) for writing with 66 nJ pulses at a translation speed of 1200 mm/min. The sample was subsequently annealed to obtain a more symmetric and Gaussian refractive index profile [29]. This significantly improves waveguide throughput efficiency, as shown in Ref. [30]. This process yields a mode

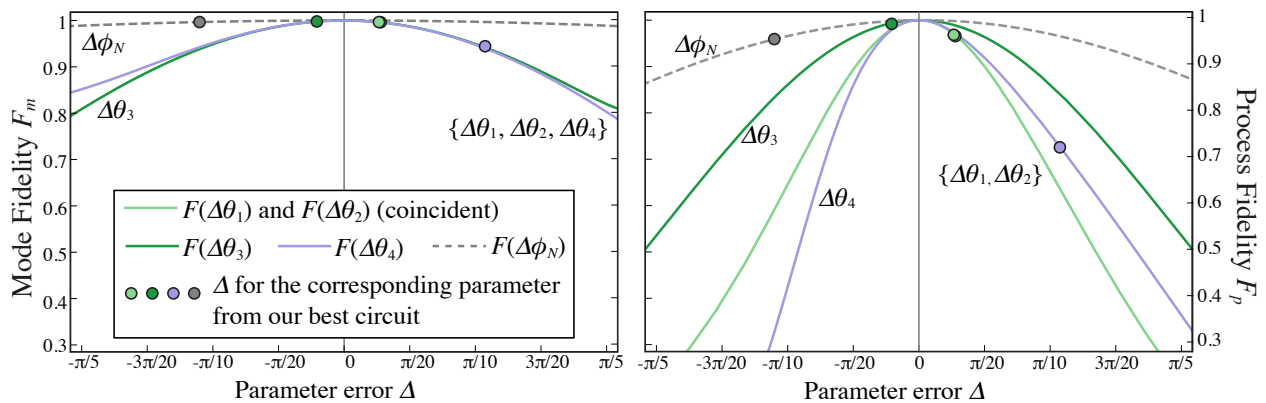


Figure 8.2: Variation of the model mode fidelity F_m and process fidelity F_p with deviations Δ from the ideal BS angles and internal phase shift. The ideal phase is zero and $\Delta\Phi_N$ represents any net extra phase introduced between beamsplitters. For the BSs Δ is the variation from the ideal angle; the total reflectivity will be $\cos^2(\theta_{\text{ideal}} + \Delta\theta)$. In both cases Δ is a length variation in the physical device. The points shown represent the deviations found in our best experimentally-characterised circuit; see Fig. 8.3 for further details. Note that on this scale both the curves and points for BS1 and BS2 are indistinguishable.

field diameter of $5 \mu\text{m}$ which has excellent overlap with an 800 nm single-mode optical fibre, and gives rise to fibre-to-fibre coupling loss of only 1.8 dB for straight waveguides of length 40 mm .

The splitting ratios of the waveguide BSs—or directional couplers—can be adjusted by changing their coupling lengths. Using a symmetric phase convention, the amplitudes in an ideal directional coupler of total length L with uniform coupling constant C vary sinusoidally with propagation length z as $a_j^\dagger \rightarrow a_j^\dagger \cos(Cz) + ia_k^\dagger \sin(Cz)$, where $j, k = \{1, 2\}$ and $0 \leq z \leq L$. The reflectivity is then $R = \cos^2 \gamma$, where $\gamma = \int_0^L C(z) dz$ even for real couplers where $C(z)$ is not constant.

While specific, arbitrary phase shifts are difficult to realise precisely using FLDW [22], adjustments in coupler length also allowed us to achieve the requisite internal phase shift of precisely π . Extending L such that γ goes from θ to $(2\pi - \theta)$ changes the action of the splitter to $a_j^\dagger \rightarrow a_j^\dagger \cos(-\theta) + ia_k^\dagger \sin(-\theta) = a_j^\dagger \cos(\theta) - ia_k^\dagger \sin(\theta)$. Exploiting this identity, we implemented the requisite phase shift by lengthening BS3 from $\gamma = \arccos \sqrt{1/3}$ to $\gamma = (2\pi - \arccos \sqrt{1/3})$. For ideal couplers the relative phase is limited to $\pm\pi/2$ and the application of this technique on BS3 yields no undesired internal phase ϕ_N , even for slight errors in L . In practice $\phi_N \neq 0$ can occur due to slight variations in local waveguide profile resulting from laser power fluctuations in fabrication, as well as from small internal path length variations.

An extensive parameter study of directional couplers was completed in order to determine the optimal laser characteristics, writing algorithm, and coupling lengths for achieving the desired reflectivities and internal phase. However, the performance of couplers written according to a particular algorithm will nevertheless vary from sample to sample, depending on the precise substrate and laser characteristics at the time of fabrication. In particular, slight refractive index differences between the two waveguides constitute a significant source of deviations from intended reflectivities. Such differences yield phase mismatch which prevents full power transfer between the waveguides, an effect which becomes more pronounced as coupling length increases. Twelve separate candidate circuits were thus fabricated, both to increase the likelihood of achieving near-optimal phase and reflectivity parameters in one or more circuits, and in order to experimentally investigate the sensitivity of device operation to parameter variations.

8.3 Results and Discussion

8.3.1 Coherent device characterisation.

We characterised the fabricated candidate circuits using a recently-demonstrated technique [31, 32] which yields $U^{\text{meas}} = r^{\text{meas}} \exp(i\phi^{\text{meas}})$ using only single- and two-mode bright coherent states and output intensity measurements. The moduli r_{jk}^{meas} result from intensity measurement at each output k for an input at mode j , while the phases ϕ_{jk}^{meas} are obtained as follows: a two-mode coherent state is injected into two inputs, and a relative phase between the modes is induced via continuous path-length variation in one mode using motorised translation. The output interference fringes are recorded with fast photodiodes and an oscilloscope, and the phases ϕ_{jk}^{meas} are simply the phase differences between the pairs of resulting periodic output intensity signals $\{I_j(t)\}$. However, due to experimental noise and slight variations in the phase-setting translation velocity, it was more accurate in practice to determine the unknown phases ϕ_{jk}^{meas} by subtracting the discrete Fourier transforms of the output signals.

The resulting 12 measured maps U^{meas} are nearly unitary within error: over all 12 circuits the maximum value of $D_{jk} = |U_{jk}^{\text{meas}} U_{jk}^{\text{meas}\dagger} - \mathbb{1}_{jk}|$ was 0.050, with a mean of 0.010, and on average D_{jk} differed from zero by just 1.6 standard deviations (determined through Monte Carlo analysis using our uncertainties in r_{jk}^{meas} and ϕ_{jk}^{meas}). Comparison of the measured matrices U^{meas} to U^{circ} in Eq. (8.2) allows nearly direct determination of the net phase ϕ_N ; notably the values of ϕ_{jk}^{meas} are consistent with U^{circ} to within error. The splitting parameters

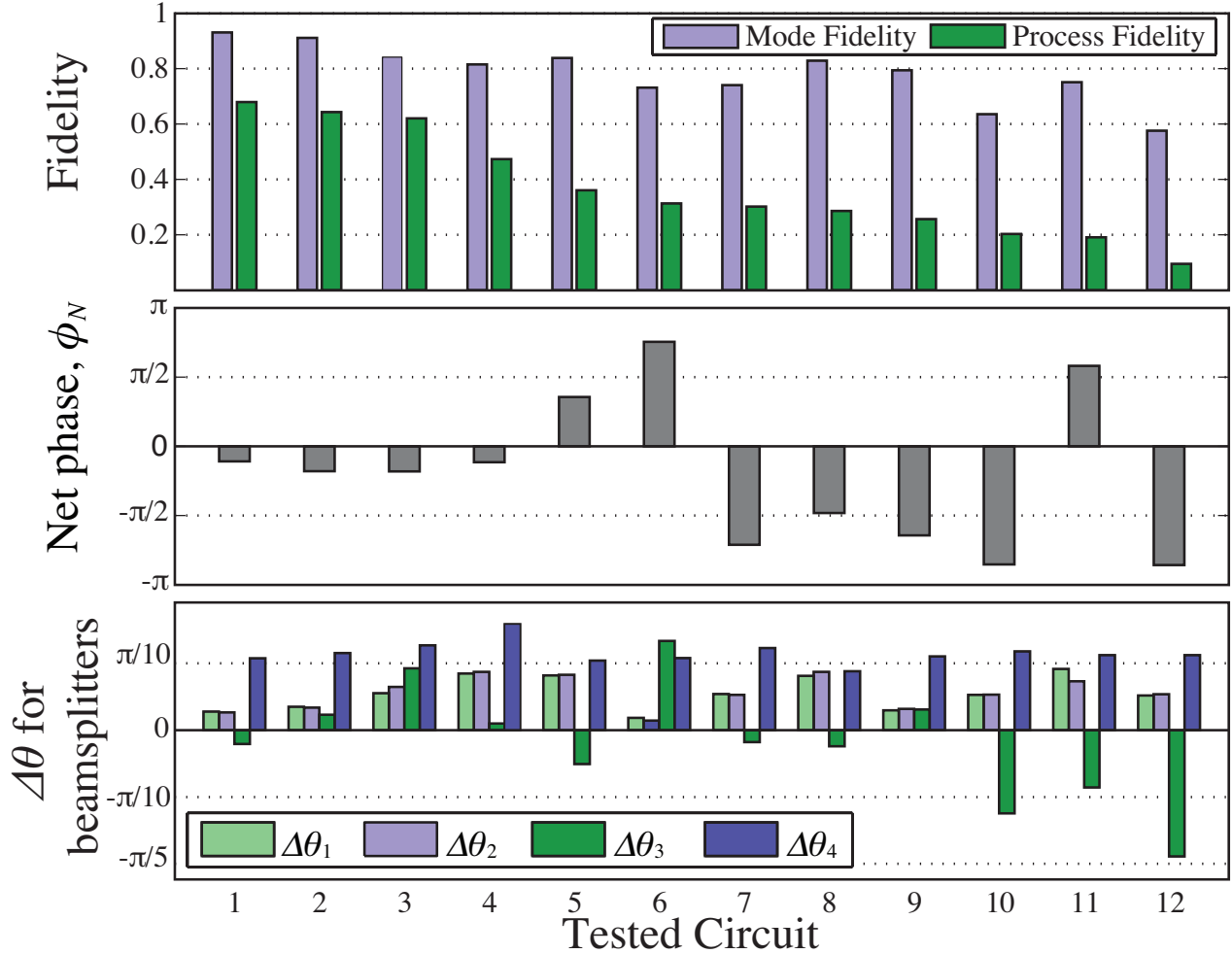


Figure 8.3: Results from coherent circuit characterisation. Error bars are too small to see and are thus absent. Top: Mode and process fidelity of the measured circuit mappings with the ideal hCZ circuit unitary, optimised over local external phases. The mean uncertainty in F_m and F_p are 0.002 and 0.006 respectively. Centre: Net undesired internal phase ϕ_N . The displayed value is the mean of the four values determined from the four occurrences of ϕ_N in comparing U^{meas} for each circuit to Eq. (8.2). For all 12 candidate circuits these differ by a maximum of 0.07. The mean uncertainty is 0.0015. Bottom: Deviations $\Delta\theta$ from the ideal reflectivity parameters for the four BSs. The mean uncertainty for all values of $\Delta\theta$ is 0.0026. In all 3 panels, the measured circuits are ordered by decreasing process fidelity.

θ_n , $n \in \{1, \dots, 4\}$ can be determined from r^{meas} using numerical optimisation. The results for F_p , F_m , ϕ_N , and θ_n for all 12 measured candidate circuits are shown in Fig. 8.3. Notably the fidelity values shown were calculated directly from the measured matrices U^{meas} , but agree to within error with the values calculated from the measured phase and reflectivity deviations in the manner depicted in Fig. 8.2. The relatively higher variance in θ_3 is due largely to the increased sensitivity of longer couplers to slight index mismatches, as explained in Sec. 8.2.2; BS3 has a coupling region almost six times the length of BS1 and BS2 in order to achieve the required internal phase shift.

For the best measured device, the mode and process fidelities determined were $F_m(U^{\text{meas}}, U^{\text{hcz}}) = 0.931 \pm 0.001$ and $F_p = 0.680 \pm 0.005$ respectively; the net internal phase found was $\phi_N = -0.346 \pm 0.013$, and the splitting parameter deviations determined were $\Delta\theta_1 = 0.087 \pm 0.002$, $\Delta\theta_2 = 0.083 \pm 0.003$, $\Delta\theta_3 = -0.065 \pm 0.003$, and $\Delta\theta_4 = 0.337 \pm 0.002$. As an illustration these parameter deviations are also depicted in Fig. 8.2 along with their individual effects on the fidelities. For all 12 devices BS4 was erroneously fabricated with a reflectivity near 60% rather than the ideal value of 90.8% due to a coding error which resulted in failure to vary the length of this coupler in fabrication as intended. However we note that if $\Delta\theta_4$ had been approximately the mean of the other splitting deviations achieved, with a value of 0.08, the process fidelity calculated according to those parameter errors would have been $F_p = 0.882$ and the mode fidelity $F_m = 0.984$.

8.3.2 Verification using two-photon interference.

Unfortunately current photon generation technology prevents full operation of these circuits as gates. Employing four photons from two concurrent photon-pair generation events via spontaneous parametric downconversion (SPDC)—the current state-of-the-art in generating multiple single photons—suffers severely from heralding false-positives. Two pairs are as likely to be generated in the same event as in two separate but contemporaneous events, which could lead to four output single-photon detections without having a photon input into each of the four modes. Triggering the ancillary photons could mitigate this, but would require a minimum of six SPDC photons. Given the $2/27$ gate success probability and the low rate of such simultaneous many-photon generation events, and despite our waveguides' relatively low losses of 1.8 dB, the expected miniscule 6-fold coincidence detection rates would necessitate prohibitively long integration times, and the corresponding low signal-to-noise ratio would allow only limited conclusions regarding actual gate fidelity. Meanwhile, no solid-state photon generation techniques to date have demonstrated the simultaneous production of

four or more spatially-separated single photons sufficiently mode-matched for high-visibility non-classical interference, although due to recent promising advances—such as the operation of a non-heralding entangling LOQC gate using indistinguishable photons from quantum dots in micropillar optical cavities [5]—that may change in the near future.

Despite requiring four input photons for full operation, the hCZ circuit relies only on fourth-order interference effects (in field), *i.e.* two-photon quantum interference; any higher-order interference effects between the four input photons can only result in error terms where the control and target qubits along with the two ancillary modes do not output exactly one photon each. In order both to confirm the ability of the circuits to support high-visibility quantum interference and to verify the results of their coherent characterisation, we therefore measured the visibility of two-photon quantum interference in the best-performing circuit for all possible input-output mode combinations. These measured visibilities are compared against both predictions from our classical characterisation and the ideal hCZ circuit visibilities in Fig. 8.4.

The apparatus for measuring the quantum interference effects is depicted schematically in Fig. 8.4(a). We measured two-photon quantum interference visibility for all $\binom{4}{2}^2=36$ combinations of two input and two output ports. The interference visibility V is calculated as $V=(C_{\max}-C_{\min})/C_{\max}$, where C is the rate of coincident photon detection events as a function of the temporal delay between the input photons, and C_{\max} and C_{\min} are calculated from a fit to the data as shown in Fig. 8.4(b).

The measured visibilities are shown in Fig. 8.4(c), along with those predicted from U^{meas} as determined via coherent characterisation, and the visibilities for an ideal hCZ circuit. The mean absolute difference between the measured and predicted visibilities is 0.05. Perhaps a better comparison is achieved by numerically calculating the unitary U^{vis} which would yield the minimum root-mean-square difference from the measured visibilities; this unitary has mode fidelities of $F_m(U^{\text{meas}}, U^{\text{vis}}) = 0.983$ and $F_m(U^{hCZ}, U^{\text{vis}}) = 0.931$ with the measured circuit and the ideal hCZ respectively. The small differences between predicted and measured visibilities can be attributed largely to three factors: polarisation non-degeneracy between the interfering photons in the FLDW circuit; the differing spectra of the SPDC photons and the laser diode used for the coherent characterisation; and the effects of higher-order SPDC terms.

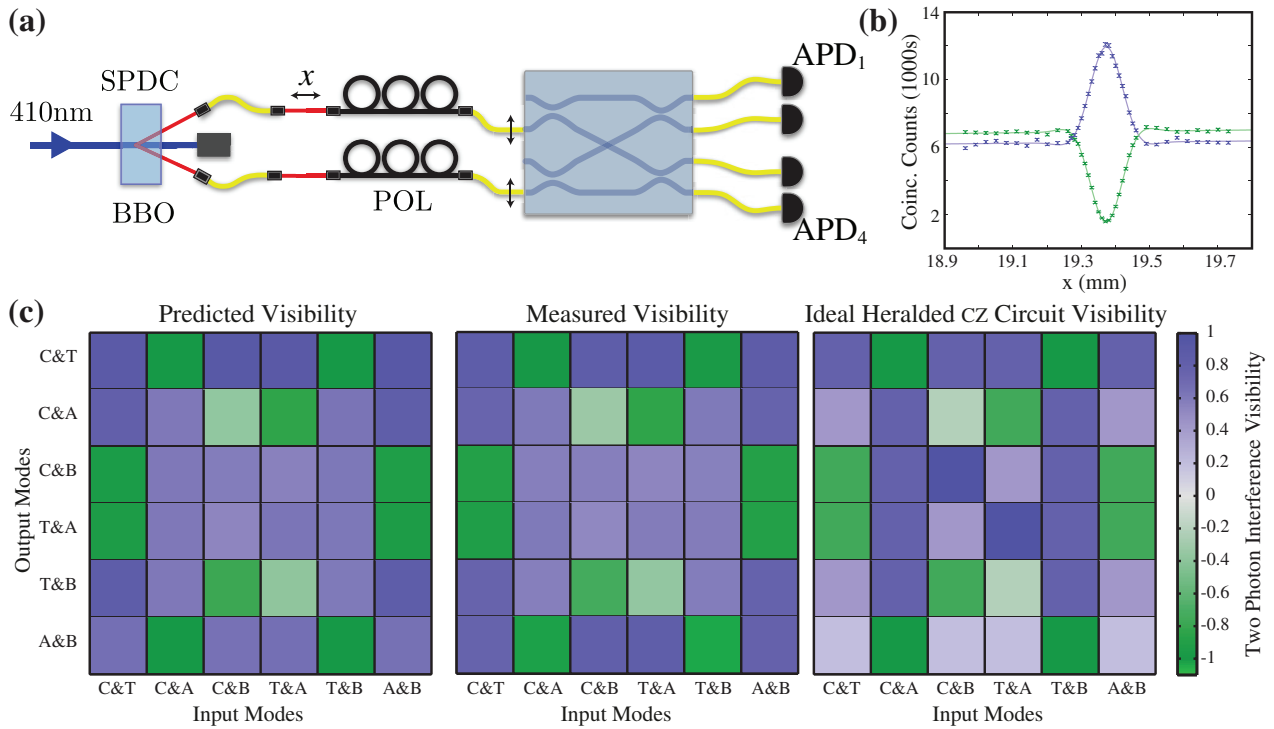


Figure 8.4: (a) Setup for measuring two-photon interference. Degenerate photon pairs at 820 nm are created via SPDC in a nonlinear β -barium-borate (BBO) crystal pumped by a 410 nm frequency-doubled Ti:sapphire laser. Manual polarisation controllers (POL) enable alignment of SPDC polarisation with the axes of polarisation-maintaining fibers coupled to the test device. We detect photons in coincidence using avalanche photo diodes (APD). (b) Representative observed non-classical interference patterns, showing anti-coalescent and coalescent interference for two different output mode combinations as well as fits to the data with Gaussian and sinc components. (c) Two photon interference results for our best h CZ circuit. We compare predictions (left) from the coherently-characterised circuit against measured two-photon interference visibilities (centre). The right panel shows visibilities for the ideal circuit U^{hCZ} ; most of the difference between this panel and the other two is due to the deviation in our best circuit from the ideal reflectivity for BS4 and unwanted net phase ϕ_N , as shown in Fig. 8.3.

8.4 Conclusions

Along with further improvements in photon sources and detection, heralding will be required to concatenate multiple entangling LOQC gates and thus enable more complex quantum computations and simulations. We have demonstrated that integrated waveguide arrays, and particularly the FLDW technique, are capable of generating the required multimode interference circuits with both high fidelity and excellent quantum interference, and allow simple implementation of mode crossover elements and π phase shifts. However further careful engineering will be required to precisely achieve the desired beamsplitter ratios and to avoid undesired phase accumulation.

The quantum process fidelity of candidate circuits can be calculated from known fabrication tolerances or classical characterisation results using the Jamiolkowski isomorphism, and this metric has proven to be more sensitive and useful than mode fidelity for assessing such circuits. However any circuit imbalance will lead to error terms outside the computational subspace wherein two photons exit in either the control or target mode. The precise effects of such coherent error terms when multiple gates are concatenated, as well as possibilities for their correction or mitigation, could be a fruitful avenue for future investigation.

Acknowledgments

This research was supported in part by the Australian Research Council Centre of Excellence for Ultrahigh bandwidth Devices for Optical Systems (CE110001018), the Centre of Excellence for Quantum Computation and Communication Technology (CE110001027), and the Centre of Excellence for Engineered Quantum Systems (CE110001013). AF is supported by an Australian Research Council Discovery Early Research Award (DE130100240), and AGW by a UQ Vice-Chancellor's Senior Research Fellowship.

References

- [1] Knill, E., Laflamme, R. & Milburn, G. A scheme for efficient quantum computation with linear optics. *Nature* **409**, 46–52 (2001). 134
- [2] Schell, A. W. *et al.* Three-dimensional quantum photonic elements based on single nitrogen vacancy-centres in laser-written microstructures. *Sci. Rep.* **3**, 1577 (2013). 134
- [3] Silverstone, J. W. *et al.* On-chip quantum interference between silicon photon-pair sources. *Nature Photon.* **8**, 104–108 (2013). 134
- [4] Meany, T. *et al.* Hybrid photonic circuit for multiplexed heralded single photons. *Laser Photon. Rev.* **8**, L42–L46 (2014). 134
- [5] Gazzano, O. *et al.* Entangling quantum-logic gate operated with an ultrabright semiconductor single-photon source. *Phys. Rev. Lett.* **110**, 250501 (2013). 134, 142
- [6] Calkins, B., Mennea, P. & Lita, A. High quantum-efficiency photon-number-resolving detector for photonic on-chip information processing. *Opt. Express* **21**, 22657–22670 (2013). 134
- [7] Reithmaier, G. *et al.* On-chip time resolved detection of quantum dot emission using integrated superconducting single photon detectors. *Sci. Rep.* **3**, 1901 (2013). 134
- [8] Sahin, D. *et al.* Waveguide photon-number-resolving detectors for quantum photonic integrated circuits. *Appl. Phys. Lett.* **103**, 111116 (2013). 134
- [9] Politi, A., Cryan, M. J., Rarity, J. G., Yu, S. & O’Brien, J. L. Silica-on-silicon waveguide quantum circuits. *Science* **320**, 646–9 (2008). 134
- [10] Crespi, A. *et al.* Integrated photonic quantum gates for polarization qubits. *Nat. Commun.* **2** (2011). 134
- [11] Pittman, T. B., Fitch, M. J., Jacobs, B. C. & Franson, J. D. Experimental controlled-not logic gate for single photons in the coincidence basis. *Phys. Rev. A* **68**, 032316 (2003). 134
- [12] Okamoto, R., O’Brien, J. L., Hofmann, H. F. & Takeuchi, S. Realization of a Knill-Laflamme-Milburn controlled-NOT photonic quantum circuit combining effective optical nonlinearities. *Proc. Natl. Acad. Sci. U.S.A.* **108**, 10067–71 (2011). 134

- [13] Knill, E. Quantum gates using linear optics and postselection. *Phys. Rev. A* **66**, 052306 (2012). [134](#), [136](#)
- [14] Marshall, G. D. *et al.* Laser written waveguide photonic quantum circuits. *Opt. Express* **17**, 12546–12554 (2009). [134](#)
- [15] Smith, B. J., Kundys, D., Thomas-Peter, N., Smith, P. G. R. & Walmsley, I. A. Phase-controlled integrated photonic quantum circuits. *Opt. Express* **17**, 13516–13525 (2009). [134](#)
- [16] Meany, T. *et al.* Non-classical interference in integrated 3D multiports. *Opt. Express* **20**, 26895–26905 (2012). [134](#)
- [17] Spagnolo, N. *et al.* Three-photon bosonic coalescence in an integrated tritter. *Nat. Commun.* **4**, 1606 (2013). [134](#)
- [18] Heilmann, R., Keil, R., Grfe, M., Nolte, S. & Szameit, A. Ultraprecise phase manipulation in integrated photonic quantum circuits with generalized directional couplers. *Appl. Phys. Lett.* **105**, 061111 (2014). [134](#)
- [19] Keil, R. *et al.* All-optical routing and switching for three-dimensional photonic circuitry. *Sci. Rep.* **1** (2011). [134](#)
- [20] Di Giuseppe, G. *et al.* Einstein-Podolsky-Rosen spatial entanglement in ordered and Anderson photonic lattices. *Phys. Rev. Lett.* **110**, 150503 (2013). [134](#)
- [21] Tillmann, M. *et al.* Experimental boson sampling. *Nature Photon.* **7**, 540–544 (2013). [134](#)
- [22] Crespi, A. *et al.* Anderson localization of entangled photons in an integrated quantum walk. *Nature Photon.* **7**, 322–328 (2013). [134](#), [138](#)
- [23] Owens, J. O. *et al.* Two-photon quantum walks in an elliptical direct-write waveguide array. *New J. Phys.* **13**, 075003 (2011). [134](#)
- [24] Jamiołkowski, A. Linear transformations which preserve trace and positive semidefiniteness of operators. *Rep. Math. Phys.* **3**, 275 – 278 (1972). [136](#)
- [25] Gilchrist, A., Langford, N. & Nielsen, M. Distance measures to compare real and ideal quantum processes. *Phys. Rev. A* **71**, 062310 (2005). [136](#)
- [26] White, A. G. *et al.* Measuring two-qubit gates. *J. Opt. Soc. Am. B* **24**, 172 (2007). [136](#)

- [27] Jovanovic, N. *et al.* Integrated photonic building blocks for next-generation astronomical instrumentation I: the multimode waveguide. *Opt. Express* **20**, 17029–17043 (2012). 137
- [28] Gross, S. *et al.* Femtosecond direct-write überstructure waveguide Bragg gratings in ZBLAN. *Opt. Lett.* **37**, 3999–4001 (2012). 137
- [29] Arriola, A. *et al.* Low bend loss waveguides enable compact, efficient 3D photonic chips. *Opt. Express* **21**, 2978–2986 (2013). 137
- [30] Meany, T. *et al.* Towards low-loss lightwave circuits for non-classical optics at 800 and 1,550 nm. *Appl. Phys. A* **114**, 113–118 (2013). 137
- [31] Rahimi-Keshari, S. *et al.* Direct characterization of linear-optical networks. *Opt. Express* **21**, 13450–13458 (2013). 139
- [32] Broome, M. A. *et al.* Photonic boson sampling in a tunable circuit. *Science* **339**, 794–798 (2013). 139

Chapter 9

Conclusion and outlook

We have reported on several experiments demonstrating the utility of laser-written waveguide arrays for optical quantum information science. These experiments provide further evidence that the rapidly-maturing field of integrated quantum photonics—particularly with the flexibility allowed by three-dimensional laser-written waveguide arrays [1]—constitutes a strong platform for quantum simulations.

The efficiency of quantum transport, especially in noisy open quantum systems, is currently of great interest [2]. We investigated two analog optical simulations of quantum effects related to transport of photo-induced molecular excitations in photosynthetic networks of coupled chromophore molecules:

1. The B850 subunit is part of a light harvesting complex in the purple bacteria *Rhodospira rubra*, which is known for its near-unit photosynthetic light harvesting efficiency [3]. We presented theory, modeling, and experimental results from an effort to simulate this Hamiltonian in an array of 16 coupled waveguides with a particular three-dimensional geometric arrangement. We showed how a combination of fabrication parameter studies and modeling techniques could be used to iteratively home in on the optimal geometric parameters, and detailed potentially deleterious fabrication and coupling effects which must be taken into account. We ultimately found this simulation to be somewhat beyond the capabilities of laser-written waveguide technology at the time, but certainly feasible in the near future given some careful attention to engineering the index contrasts and coupling constants of laser-written waveguides, especially in light of the subsequent rapid progress of that technology.

2. We simulated environmentally-assisted quantum transport (ENAQT) [2] in an experimental toy model consisting of an array of coupled waveguides with an ‘energy gap’—in practice a difference in propagation constants—where decohering noise was implemented by broadening the bandwidth of the input photons. ENAQT is a quantum transport phenomenon wherein moderate decoherence may, perhaps counterintuitively, increase transport efficiency by suppressing coherent localizing effects. It is hypothesized to play an important role in explaining the high efficiency of molecular excitation transport from the sites of solar photon absorbance to photosynthetic reaction centers in light-harvesting organisms. Our first-generation simulator showed a noise-induced transport enhancement of $7.2 \pm 2.4\%$, and we are optimistic that our second generation simulators will show a larger enhancement, as well as allowing multiple simulation lengths in order to illuminate transport dynamics.

In two other experiments, we also employed laser-written waveguide to study multi-walker quantum walks and circuits for heralded entangling quantum gates:

3. We studied the evolution of two-photon quantum states in continuous-time quantum walk with periodic boundary conditions, implemented in an elliptic array of laser-written waveguides. Our classical-light characterization allowed us to predict output correlations for two-photon inputs, and this experiment helped to set the stage for analog waveguide-array simulations of non-trivial Hamiltonians, in particular the simulations of quantum transport enumerated above.
4. Two-qubit photonic entangling gates will need to be heralded by the detection of ancillary photons to enable further advances in linear-optics quantum computing. We investigated the implementation of the optimal known heralded entangling gate design, which implements a controlled-z operation and was found by Knill [4]. We studied implementation of this gate design in a laser-written waveguide array, and particularly focused on the performance of the device in the presence of deviations from the optimal beam-splitting ratios and phase shifts. We showed how prototype circuits could be characterized using both classical and quantum interference techniques. The high mode indistinguishability—as evidenced by the agreement between the predictions for quantum interference, made using our classical-light measurement results, and the quantum interference visibility measurements—as well as the high circuit fidelity shown to be possible using the femtosecond laser-writing technique, demonstrate the promise of integrated quantum photonics for such gates and ultimately for optical quantum information processing.

We are convinced that integrated quantum photonics will play a crucial role in the future of optical quantum information science, especially given the rapid rate of progress in this field during the course of the research for this thesis. A particularly exciting prospect is that of analog quantum simulators of sufficient size to begin to rival the capabilities of simulations on conventional computers [5]. Consider the results presented here, in combination with recent progress on reconfigurable quantum circuits [6–8], fast optical integrated optical switching [9–12], high-quantum-efficiency integrated detection [13–15], and integrated arbitrary unitary operations on path- and polarization-encoded photonic qubits [16–20]: Given these capabilities, it is entirely plausible that integrated photonics is the platform best suited to the first analog quantum simulations capable of challenging the simulation capabilities of conventional computers—a very exciting prospect for the entire field of quantum information science.

References

- [1] Marshall, G. D. *et al.* Laser written waveguide photonic quantum circuits. *Opt. Express* **17**, 12546–12554 (2009). 148
- [2] Reberntrost, P., Mohseni, M., Kassal, I., Lloyd, S. & Aspuru-Guzik, A. Environment-assisted quantum transport. *New J. Phys* **11**, 033003 (2009). 148, 149
- [3] Kassal, I. *Quantum Computation for Chemical Problems*. Ph.D. thesis, Harvard University (2010). 148
- [4] Knill, E. Quantum gates using linear optics and postselection. *Phys. Rev. A* **66**, 052306 (2012). 149
- [5] Georgescu, I. M., Ashhab, S. & Nori, F. Quantum simulation. *Rev. Mod. Phys.* **86**, 153–185 (2014). 150
- [6] Li, H. W. *et al.* Reconfigurable controlled two-qubit operation on a quantum photonic chip. *New J. Phys.* **13**, 115009 (2011). 150
- [7] Shadbolt, P. J. *et al.* Generating, manipulating and measuring entanglement and mixture with a reconfigurable photonic circuit. *Nature Photon.* **6**, 45–49 (2012). 150
- [8] Smith, B. J., Kundys, D., Thomas-Peter, N., Smith, P. G. R. & Walmsley, I. A. Phase-controlled integrated photonic quantum circuits. *Opt. Express* **17**, 13516–13525 (2009). 150
- [9] Alibart, O., Ostrowsky, D. B., Baldi, P. & Tanzilli, S. High-performance guided-wave asynchronous heralded single-photon source. *Opt. Lett.* **30**, 1539 (2005). 150
- [10] Bonneau, D. *et al.* Fast path and polarization manipulation of telecom wavelength single photons in lithium niobate waveguide devices. *Phys. Rev. Lett.* **108**, 053601 (2012). 150
- [11] Jin, H. *et al.* Reconfigurable on-chip entangled sources based on lithium-niobate waveguide circuits. *arXiv:1404.0274* (2014). 150
- [12] Lobino, M. *et al.* Correlated photon-pair generation in a periodically poled MgO doped stoichiometric lithium tantalate reverse proton exchanged waveguide. *Appl. Phys. Lett.* **99**, 081110 (2011). 150
- [13] Sprengers, J. P. *et al.* Waveguide superconducting single-photon detectors for integrated quantum photonic circuits. *Appl. Phys. Lett.* **99**, 181110 (2011). 150

-
- [14] Sahin, D. *et al.* Waveguide photon-number-resolving detectors for quantum photonic integrated circuits. *Appl. Phys. Lett.* **103**, 111116 (2013). 150
- [15] Tanner, M. G. *et al.* A superconducting nanowire single photon detector on lithium niobate. *Nanotechnology* **23**, 505201 (2012). 150
- [16] Crespi, A. *et al.* Integrated photonic quantum gates for polarization qubits. *Nat. Commun.* **2** (2011). 150
- [17] Crespi, A. *et al.* Integrated multimode interferometers with arbitrary designs for photonic boson sampling. *Nature Photon.* **7**, 545–549 (2013). 150
- [18] Heilmann, R., Keil, R., Grfe, M., Nolte, S. & Szameit, A. Ultraprecise phase manipulation in integrated photonic quantum circuits with generalized directional couplers. *Applied Physics Letters* **105**, – (2014). 150
- [19] Heilmann, R., Grafe, M., Nolte, S. & Szameit, A. Arbitrary photonic wave plate operations on chip: Realizing hadamard, pauli-x, and rotation gates for polarization qubits. *Sci. Rep.* **4** (2014). 150
- [20] Corrielli, G. *et al.* Rotated waveplates in integrated waveguide optics. *Nature Commun.* **5** (2014). 150